Development of a Turbine Concept for Supercritical CO_2 Power Cycles

L.G.M. Meijboom

Delft University of Technology

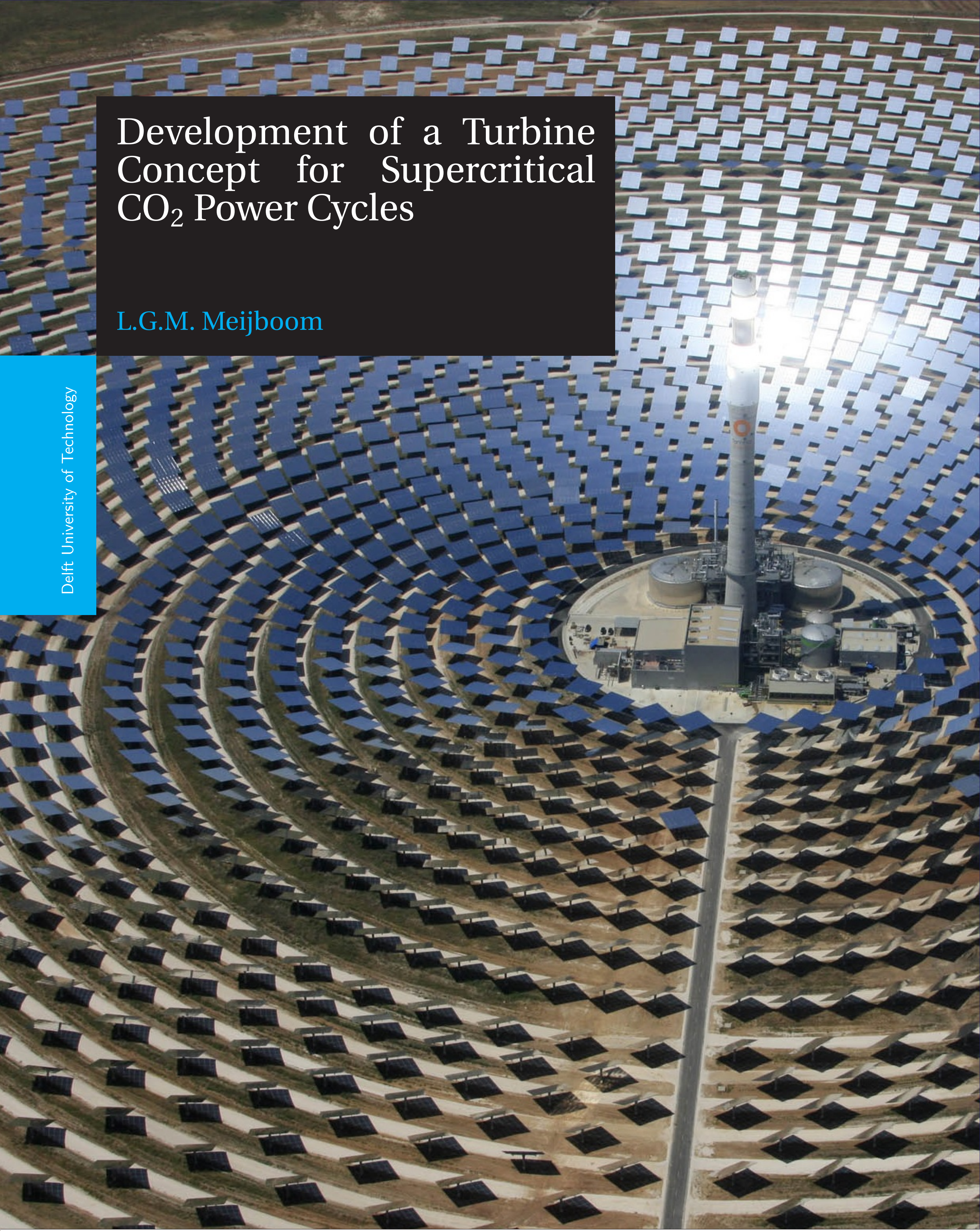

TU Delft Delft University of Technology

Challenge the future

DEVELOPMENT OF A TURBINE CONCEPT FOR SUPERCRITICAL CO_2 POWER CYCLES

by

L.G.M. Meijboom

in partial fulfilment of the requirements for the degree of

Master of Science
in Aerospace Engineering

at the Delft University of Technology,
to be defended publicly on Friday December 15, 2017 at 09:30 AM.

Thesis registration number:	`175#17#MT#FPP`	
Student number:	4202732	
Thesis committee:	Dr. ir. M. Pini,	Delft University of Technology
	Dr. I. Jahn,	University of Queensland
	Dr. A. Gangoli Rao,	Delft University of Technology
	Dr. ir. R. Pecnik,	Delft University of Technology

PREFACE

This research is part of the MSc degree in Aerospace Engineering at Delft University of Technology. The project is a result of collaborative activities between Delft University of Technology and the University of Queensland. The University of Queensland's Renewable Energy Conversion Centre of Excellence has been tasked by the Australian Solar Thermal Research Initiative to develop a regenerative cycle for experimentally testing a supercritical CO_2 power cycle for Concentrating Solar Power applications.

This report is submitted to Dr. ir. Matteo Pini (assistant professor at Delft University of Technology), Dr. Ingo Jahn (lecturer at the University of Queensland), Dr. Arvind Gangoli Rao (associate professor at Delft University of Technology) and Dr. ir. Rene Pecnik (assistant professor at Delft University of Technology). This thesis describes the methodology and results of a turbine concept which can be incorporated in the test cycle. In this report, the process of achieving the following objective is covered:

"Make recommendations on a 75-300kW supercritical CO_2 *turbine which can be tested in 2018, by designing and analysing the turbine concept."*

I would like to mention my appreciation of the assistance and guidance given by the team members of the Renewable Energy Conversion Centre of Excellence of the University of Queensland and by the Flight Performance & Propulsion group of Delft University of Technology. I would like to give special thanks to my principal supervisors Dr. ir. Matteo Pini and Dr. Ingo Jahn. Finally, I would like to thank the faculty of Aerospace Engineering of Delft University of Technology and the school of Mechanical & Mining Engineering of the University of Queensland, for providing me with the opportunity to participate in this innovative and challenging project.

Luuk Meijboom
Delft, December 2017

L Meyboom

ABSTRACT

Supercritical CO_2 (sCO_2) is considered as a working fluid in future Concentrating Solar Power (CSP) applications to increase the efficiency of the power cycle. Due to the limited experience, the turbine of an sCO_2 power cycle is in literature referred to as the component with the highest risk. In this thesis, a design methodology will be established and used to gain knowledge in sCO_2 turbine design by designing and analysing a turbine concept which can be used to generate sCO_2 turbine experimental data for validation purposes. The high density of the fluid in combination with the low power output of the turbine results in small turbine dimensions, a high rotational speed and a large axial load when using existing design wisdom. Therefore, the effect of limiting the rotational speed and axial load on the turbine design is evaluated.

The turbine design methodology includes a preliminary design module, an aerodynamic design module and a mechanical design module. The aerodynamic design module consists of a steady-state and transient solver to evaluate the importance of taking into account transient effects when estimating the aerodynamic performance. According to literature, pressure loads can have a significant effect on the stresses in sCO_2 turbines. Therefore, the mechanical design module is able to take into account the pressure loading from the steady-state and transient aerodynamic design.

The low power in combination with the limited rotational speed pushes the turbine design away from the desired specific speed range. During the preliminary design, the radial inflow turbine was found to give the best performance while meeting the turbine requirements. The degree of reaction of the turbine is close to 0, to limit the axial load due to the pressure difference across the rotor. As a result of the low specific speed, the turbine efficiency of 74% is lower than usually seen for radial inflow turbines. As no sudden peaks in entropy generation are seen across the rotor channel, it can be concluded that the high curvature of a low reaction radial inflow turbine does not seem to have a detrimental effect on the turbine performance. The main contribution to the losses can be found in the rotor channel as a result of the tip clearance losses and high flow velocities compared to reference turbines, while the stator losses are comparable. A good agreement is found between the steady-state and transient aerodynamic analysis. Based on this, it can be concluded that a steady-state analysis can give a good approximation of the turbine performance, but evaluating more designs would be required to generalise this statement to all small-scale low reaction sCO_2 turbomachinery. Due to the low degree of reaction of the turbine, the stresses originating from the pressure load are found to be less than 1% of the total stresses. Based on this, it can be concluded that only taking into account centrifugal loads for a low reaction sCO_2 turbine gives a good estimation of the stresses in the turbine during operation.

As this research focuses to a large extend on establishing the methodology, for future research it is recommended to perform a more thorough optimisation of the turbine shape, in particular to reduce the losses in the rotor channel by for example introducing a shrouded design. Moreover, it is recommended to analyse the turbine in combination with the other subsystems in the power block to also take into account the interaction between the subsystems.

Acknowledgements

This report concludes nine months of work and forms an important phase of my degree in Aerospace Engineering. This project is part of collaborative research between Delft University of Technology and the University of Queensland. My time in Delft has not only helped me to extend my knowledge into a broad field, but has also helped me to develop as a person as a result of countless group projects and international opportunities. The lessons learned in these years will benefit me for the rest of my life.

First of all, I would like to thank my principal supervisors Dr. ir. Matteo Pini from Delft University of Technology and Dr. Ingo Jahn from the University of Queensland for their enthusiasm and valuable help. Secondly, I would like to thank Dr. Rowan Gollan, Dr. Peter Jacobs, Joshua Keep, Jianhui Qi and Salvatore Vitale for giving advice and suggestions during the research. Also, I would like to acknowledge the committee for their time to read this report.

Finally, I want to express my gratitude to my family who has supported me throughout my time in Delft. Without their support I would not be where I am today.

Luuk Meijboom
Delft, December 2017

L Meyboom

NOMENCLATURE

Symbols:

a	Speed of sound $[m/s]$
A	Area $[m^2]$
A_{eff}	Effective flow area $[m^2]$
A_n	Normal flow area $[m^2]$
ang_r	Rotor outlet blade angle $[^\circ]$
ang_s	Stator outlet blade angle $[^\circ]$
b	Tangential stator blade spacing $[m]$
bax_r	Rotor axial chord $[m]$
C_p	Specific heat at constant pressure $[J/kgK]$
C_v	Specific heat at constant volume $[J/kgK]$
d	Diameter $[m]$
F	Force $[N]$
gr_{adm}	Degree of admission $[-]$
h	Blade height $[m]$
h	Enthalpy $[J/kg]$
I	Rothalpy $[J/kg]$
L	Length $[m]$
$\dot{m}$	Mass flow rate $[kg/s]$
M	Mach number $[-]$
n	Normal component $[-]$
$\vec{n}$	Surface normal vector $[-]$
N_s	Specific speed $[-]$
p	Pressure $[Pa]$
P_{out}	Output power $[kW]$
r	Degree of reaction $[-]$
R	Gas constant $[J/kgK]$
R	Radius $[m]$
rrr	Rotor inlet-to-outlet diameter ratio $[-]$
s	Entropy $[J/kgK]$
$\vec{S}$	Local streamline vector $[m]$
t	Thickness $[m]$
T	Temperature $[K]$
T	Torque $[Nm]$
tke	Turbulent kinetic energy $[J/kg]$
U	Blade velocity $[m/s]$
v	Jet-speed ratio [-]
V	Absolute velocity $[m/s]$
$\vec{V}$	Absolute velocity vector $[m/s]$
V_{grid}	Grid velocity $[m/s]$
$\overrightarrow{V_{grid}}$	Grid velocity vector $[m/s]$
W	Relative velocity $[m/s]$
$\vec{W}$	Relative velocity vector $[m/s]$
Y	Total pressure loss coefficient $[-]$
z	Axial length $[m]$
Z	Loss $[kW]$

Greek letters:

α	Absolute angle $[^\circ]$
β	Relative angle $[^\circ]$
γ	Ratio of specific heats $[-]$
η	Efficiency $[-]$
θ_{eff}	Effective flow angle $[^\circ]$
μ_{ref}	Reference laminar viscosity $[Ns/m^2]$
$\mu_{t,ref}$	Reference viscosity temperature $[K]$
ρ	Density $[kg/m^3]$
ϕ	Property of interest
ϕ	Twist angle $[^\circ]$
φ	Flow coefficient $[-]$
ψ	Head coefficient $[-]$
ω	Rotational speed $[rpm]$

Subscripts:

0	Total
atm	Atmospheric
ax	Axial
in	Inlet
is	Isentropic
KE	Kinetic energy
LE	Leading edge
out	Outlet
$root$	Blade root
$r\theta$	Projection on $r-\theta$ plane
tcl	Tip clearance
TE	Trailing edge
tip	Blade tip
ts	Total-to-static
tt	Total-to-total
x	X-component
y	Y-component
z	Z-component
θ	Tangential

Abbreviations:

ASTRI	Australian Solar Thermal Research Initiative
BLP	Boundary Layer Point
CFD	Computational Fluid Dynamics
CFL	Courant–Friedrichs–Lewy
CSP	Concentrating Solar Power
HCF	High Cycle Fatigue
KE	Kinetic Energy
ORC	Organic Rankine Cycle
RANS	Reynolds-Averaged Navier-Stokes
RIT	Radial Inflow Turbine
ROT	Radial Outflow Turbine
sCO_2	Supercritical CO_2
SP	Separation Point
TKE	Turbulent Kinetic Energy
UQ	University of Queensland

CONTENTS

LIST OF FIGURES

LIST OF TABLES

1

INTRODUCTION

Power cycles using fluids in the supercritical state were studied for the first time by the end of the 1960's by Angelino [1] and Feher [2] as there was a need for more energy efficient power cycles. This was also the time CO_2 was identified as a promising fluid due to its characteristics. Fluid properties of CO_2 show significant variations near its critical point, which is $7.38 MPa$ and $30.98°C$. This principle is used to reduce the required compressor work and thereby improve the efficiency of the cycle. The research on supercritical CO_2 (sCO_2) came to a stop after many years for several reasons, but gained renewed interest in the early 2000's for nuclear applications [3]. Whereas nuclear applications were the driving interest behind researching sCO_2 power cycles again, shortly afterwards also the potential of using sCO_2 for Concentrating Solar Power (CSP) applications was identified [4], which traditionally uses steam as a working fluid. As many of the renewable energy sources are strongly dependent on time-varying environmental conditions, there is a need for a system like CSP that can efficiently dispatch power over a large range of output powers, to compensate for output power variations of other renewable sources [5]. One of the main challenges of sCO_2 power cycles is the design of turbomachinery components. The high fluid density of sCO_2 and the resulting small turbomachinery components make the design challenging, also because of the potentially large pressure forces acting on the turbine. To bring down the axial load on the rotor to acceptable levels, a low reaction radial inflow turbine can be a design of interest.

First, in Section 1.1 the background of sCO_2 turbines in CSP applications will be discussed. This is followed by Section 1.2, where the motivation and scope of this thesis are elaborated upon, including an introduction to the research questions that will be answered in this research. Finally, in Section 1.3 the outline of this thesis will be given.

1.1. BACKGROUND

Using supercritical fluids like sCO_2 in thermodynamic cycles has the effect that volume flow rates become low due to the high fluid densities. These low flow rates lead to a substantial reduction in specific speed compared to alternate power cycles [6]. The specific speed is a turbine design parameter and is a function of the flow rate [7]. Because of the high power density and the relatively low expansion ratio of sCO_2 cycles, a smaller number of stages can be used in the turbine unit. Using these allows substantially simpler turbine system designs, as the number of seals and the complexity of supporting systems can be reduced.

Radial turbines have received much attention in the past for water, ideal gas and steam systems [8] [9]. However, the operation with sCO_2 creates new challenges, due to the a-typical fluid properties. For example at the target operating conditions, the viscosity is comparable to air, while the density can be more than 100 times higher. These highly different fluid properties make the design of turbines more challenging, but also raise questions about the validity of existing design wisdom. To improve sCO_2 turbine designs and to validate or disprove existing design wisdom, it is essential to experimentally investigate the performance of sCO_2 turbine prototypes and to create the sets of experimental data for validation purposes.

To date a number of sCO_2 turbine designs for CSP applications have been published and these are sum-

Table 1.1: sCO_2 turbine design for CSP applications in literature.

	Year	Power $[MW]$	Axial turbine	Radial inflow turbine
Muto et al. [10]	2014	100	✓	
Kalra et al. [11]	2014	10	✓	
Turchi [12]	2014	14	✓	
Qi et al. [13]	2016	0.1		✓
Qi et al. [13]	2016	0.2		✓
Spazzoli [14]	2016	50	✓	

marised in Table 1.1. At a glance it can be seen that the number of designs in literature is rather limited and have all been published in recent years.

From the turbine designs as shown in Table 1.1, a preliminary design is completed in all of the studies. The study of Muto et al. [10] is more of a comparative study between an sCO_2 turbine and a Brayton CO_2 turbine, without explaining the method of the turbine designs. Only in the study of Kalra et al. [11] the study is extended with a Computational Fluid Dynamics (CFD) simulation using an in-house CFD program, although hardly any detail is given about either the preliminary or CFD design. Turchi [12] describes the development of a multi-year testing program for an sCO_2 power cycle. The study of Qi et al. [13] shows the method of the preliminary design for a $100kW$ and $200kW$ turbine, which both use an in-house preliminary design tool TOPGEN [15]. Finally, the research of Spazzoli [14] shows the overall method of the preliminary turbine design.

The first conclusion that can be drawn is that none of the existing literature on sCO_2 turbine design for CSP applications have in detail been done and reported. Secondly, despite the limited number of turbine designs in Table 1.1, it appears that the axial turbine architecture is preferred for large applications and the radial inflow turbine architecture is preferred for the smaller power applications. Thirdly, only the research of Qi et al. describes the design of sCO_2 turbines for a similar power output as the turbine of this thesis, as will be seen in Section 1.2. Finally, none of the aforementioned turbines have been built and tested, thereby putting an uncertainty in the validity of the methods, assumptions and conclusions of the turbine designs.

The combination of high rotational speed and high pressure loads on the turbine as a result of the high fluid density of sCO_2 in the work of Qi et al. limits the feasibility of producing and experimentally testing the turbine concepts, as this would set high requirements on seal and bearing design. Turbine designs with a limited rotational speed and low degree of reaction, resulting in a low specific speed and axial load, are to date an unexplored area in the turbine design space. Because of the aforementioned reasons, exploring this region of the design space can give valuable insight in turbine characteristics, thereby potentially clearing the way to building and testing the sCO_2 turbine and providing the sets of experimental data for validation purposes to use in the future design of sCO_2 turbines in CSP applications.

1.2. MOTIVATION AND SCOPE

CSP has been identified as a technology to store and dispatch power during times of high demand in an environmentally friendly way. Using sCO_2 for CSP applications is currently of interest due to the potential increase in cycle efficiency compared to existing steam Rankine cycles or Organic Rankine Cycles (ORC) [16], making it therefore also interesting from an economical point of view. In the past, several turbine designs have been proposed for sCO_2 power cycles. These designs are mostly for large power applications and are therefore unsuitable for being built and tested at reasonable cost. To date none of these sCO_2 turbine designs for CSP have been built and experimentally tested, leading to a desire for validation data.

The University of Queensland (UQ) has been tasked by the Australian Solar Thermal Research Initiative (ASTRI) to develop a prototype 75-$300kW$ sCO_2 turbine that can be tested in 2018. Testing of this turbine will provide the sets of experimental data for validation purposes, required to progress the advancement of sCO_2 technologies. The scope of this project is to assist this endeavour by conducting the preliminary, aerodynamic and mechanical design of a turbine concept. Primarily this will consist of the selection of a stator and rotor and the conduction of aerodynamic analyses to assess the performance of the turbine in relation to target operating conditions. Besides that, a significant part of the work will be to assist in the development and implementation of tools to help designing the turbine for this thesis and for future research using Eilmer4 [17]. Eilmer4 is the University of Queensland's open-source transient CFD solver. In this thesis work, a design methodology will be established and will be used to gain knowledge in sCO_2 turbine design by designing and analysing a turbine concept which can be used to generate sCO_2 turbine validation data. By using conventional design methods of turbines, because of the different fluid properties of sCO_2 compared to oil or steam which are currently used in CSP plants [18], rotational speeds in excess of $150{,}000 rpm$ are required, resulting in high axial loads [13]. According to Wright [19], using conventional relationships for a $20kWe$ turbine with an expansion ratio of 3.1 would result in a turbine less than $1cm$ in diameter and operating at a rotational speed of about 1.5 million rpm. This combination of high speed and high loads is one of the design challenges that cannot be overcome with conventional bearing technologies at a reasonable cost. For this reason the turbine design is limited by ASTRI to $50{,}000 rpm$. Moreover, the combination of rotational speed and axial load on the rotor should be compatible with conventional bearing technologies.

Limiting the rotational speed and axial load pushes the turbine design towards a low specific speed and a low degree of reaction. The degree of reaction is a design parameter which, for a single-shaft configuration, allows to easily manage the thrust load. A low degree of reaction in combination with a radial inflow turbine architecture is an area of the design space which has hardly been visited. By exploring this region, potentially a new design space can be created for designers to solve thrust management issues.

The main research question is defined as follows:

What is the performance of a supercritical CO_2 turbine meeting the requirements set by the Australian Solar Thermal Research Initiative (ASTRI)?

In order to answer this main research question, several sub-questions have to be answered:

- What are the implications of the requirements set by ASTRI to the turbine design?
- What turbine architecture is more suitable for meeting the requirements set by ASTRI?
- What methods can be used to design the different turbine architectures of interest?
- What is the stator and rotor geometry to achieve the highest performance?

By answering these sub-questions, the answer to the main research question should be known. The sub-questions provide a steering function, which will help in guiding the research such that the main research question can be answered.

1.3. THESIS OUTLINE

In Chapter 2 a summary of the literature review will be given. This is followed by an overview and a short description in Chapter 3 on the methodology for supercritical CO_2 turbine design. The preliminary design of the turbine will be elaborated upon in Chapter 4. This covers the operating conditions and requirements, a verification of the 1D design tool and the design space exploration for the current research, including the turbine selection. Next, in Chapter 5 the procedure for the aerodynamic design and mechanical stress evaluation will be elaborated upon. This consists of an explanation on the procedure for the generation of the turbine geometry and grid for both the aerodynamic design and the mechanical stress evaluation, as well as the procedure to evaluate the aerodynamic and mechanical performance of the turbine. This is followed by the evaluation of the turbine concepts in Chapter 6, which concludes with a summary of the final turbine concept. Finally, the conclusions of this research and recommendations for future work can be found in Chapter 7.

2

LITERATURE REVIEW

In this Chapter, the most important aspects regarding sCO_2 turbines with respect to this thesis project as found in literature are summarised. Also, a link is tried to be made between the observations and statements made in literature and their applicability for this thesis project.

First, in Section 2.1 the experiences regarding radial inflow turbine design in general will be introduced and discussed. Secondly, in Section 2.2 an overview will be given of research on sCO_2, its use in CSP cycles and the operating region of the turbine of this thesis project. Finally, in Section 2.3 the challenges regarding sCO_2 turbine design that have been identified will be elaborated upon.

2.1. RADIAL INFLOW TURBINES

In a mixed-flow radial turbine, often simply referred to as a radial or radial inflow turbine, the flow enters the turbine radially and leaves the turbine axially. The radial inflow turbine has the advantage of being capable of achieving expansion ratios as high as 8:1 in a single stage, which would require a multi-stage axial turbine for the same expansion ratio [7]. This can be explained by looking at the Euler turbomachinery equation [7]. For a radial inflow turbine, the change in radius leads to a change in circumferential velocity between the rotor inlet and outlet, thereby contributing to the enthalpy change. The radial inflow turbine can be found in applications with various working fluids such as air [20], steam [21], organic fluids [22] and sCO_2 [13].

Among others, the potential of using a radial inflow turbine for ORC and sCO_2 applications has been identified by Qi et al. [13]. According to Persico and Pini [23], this turbine architecture is often preferred in case of an ORC turbine with a power output up to a few hundred kW, with some examples even up to power outputs in the order of $1MW$. Jahn and Keep [5] mention the possibility of using radial turbines for sCO_2 applications up to $25MW$. The non-dimensional specific speed N_s as defined by Equation 2.1 is a design parameter used to estimate the efficiency of a radial inflow turbine [7]. The specific speed is a function of the rotational speed ω, the mass flow rate $\dot{m}$, the temperature T at the inlet and outlet of the turbine, the pressure p at the outlet of the turbine, the specific heat at constant pressure C_p and the isentropic efficiency η_{is}. Limiting the maximum rotational speed of the turbine limits the specific speed, which can have a negative effect on the turbine efficiency. For turbines operating at lower specific speeds, which is of interest for the turbine design of the current thesis due to for example the rotational speed limitation as will be seen in Section 2.3, the radial inflow turbine is often preferred over the axial configuration [24].

$$N_s = \omega \cdot 0.1047 \cdot \frac{\sqrt{\dot{m} \cdot T_{rotor,out} \cdot \frac{10131.2}{p_{rotor,out}}}}{\left(C_p \cdot 10.718 \cdot \frac{T_{stator,in} - T_{rotor,out}}{\eta_{is}}\right)^{0.75}} \tag{2.1}$$

Also the unit cost of a radial inflow turbine is lower for a given expansion ratio compared to an axial turbine. This is in line with arguments made by Wheeler and Ong [25], who state that low cost and the capability to operate at high expansion ratios make radial turbines often the preferred choice for small-scale cycles. At small flow rates, a higher isentropic efficiency can be achieved when using the radial architecture compared to axial turbines. Sienicki et al. [26] argue that for sCO_2 power applications a single-stage radial turbine is often preferred for systems below $10MWe$. Usually, radial inflow turbines are preferred when unit cost and simplicity are required at smaller turbine sizes. According to Sauret and Rowlands [22], Russell et al. [6] and Walsh and Fletcher [7] the radial inflow turbine is of particular interest for ORC and other high density fluid applications for several reasons:

- They are able to accommodate a large expansion ratio of up to 8:1 in a single stage, thereby allowing for fewer stages.
- They generally achieve higher isentropic efficiencies for low capacities compared to axial turbines.
- Radial inflow turbines are able to maintain high efficiency levels at off-design conditions by making use of variable stator vanes, thereby allowing to achieve good performance during solar or environmental fluctuations.
- Blade inaccuracies have a smaller effect on the efficiency compared to axial machines, which makes it easier to maintain good efficiencies at a smaller sized turbine.
- The robustness of radial inflow turbines is higher with increasing blade load caused by the highly dense fluid.
- Since the blades are attached to the hub, the turbine is easier to manufacture compared to axial machines and is cheaper in unit cost for a given expansion ratio and capacity.

As the capacity of the turbine of this thesis project is as low as $0.0043\frac{kg\cdot\sqrt{K}}{s\cdot kPa}$, it would be beneficial to use a radial inflow turbine to achieve high efficiency [7]. Moreover, the last bullet point stressing the ease of manufacturing and the reduction in production cost is an important advantage of the radial inflow turbine for this thesis, as this will reduce the required investment for generating the experimental data. The advantage of maintaining high efficiency at off-design conditions by using variable inlet guide vanes as described above is not directly important for this thesis project as the turbine will not be used for actual electricity production and is therefore not directly influenced by solar and environmental fluctuations.

Although a radial turbine stage is capable of dealing with a larger expansion ratio than an axial turbine stage, if the expansion ratio is larger than the maximum achievable in a single stage, a multi-stage arrangement can be obtained easier in an axial machine compared to a radial machine [7]. Moreover, it is argued that by adding more swirl to the flow at the rotor outlet, the turbine work can be increased.

Because of the low mass flow rate requirement of the turbine, partial admission is one of the concepts which should be considered during the design. In a partial admission turbine, part of the flow passage is blocked. This principle can be used in small gas turbines to increase small blade heights, which reduces the losses due to secondary flows [27]. Apart from the added complexity of partial admission turbines due to the non-uniform flow, Balje and Binsley [28] showed that the four additional loss types introduced by partial admission are filling and emptying losses, losses due to scavenging, losses as a result of pumping by the blades in the blocked part of the arc and lastly the losses due to leakage between the rotor and stator. From these losses, the mixing, leakage and sudden expansion losses are considered to have the highest impact [29]. Research by Fridh et al. [30] showed a reduction in the total-to-static efficiency for lower degrees of admission. Also the velocity ratio giving the highest efficiency reduces with lower degrees of admission. Therefore, the use of partial admission turbines should be avoided if possible.

A distinction can be made between reaction and impulse turbines. In a reaction turbine, the expansion work is divided between the stator and rotor, whereas in a pure impulse turbine the expansion takes place in the stator only. Research by Ainley [31] showed that low reaction turbine stages often show low efficiencies compared to higher reaction stages. The advantage of an impulse or low reaction turbine is that, as most of the expansion happens in the stator, the pressure difference across the rotor is reduced, which makes the seal design less critical. Also this lowers the axial load of the system introduced by the pressure difference across the rotor as will extensively be discussed in Section 2.3. A lower axial load allows using less complex thrust bearing technologies.

The research of Rubechini et al. [24] describes the challenges in the CFD modelling of turbo-expanders operating in the transonic regime. It is argued that a reaction stage is often preferred in a radial turbine, thereby limiting the expansion ratio in the nozzle. However, as this would also increase the axial force due to the pressure difference across the rotor, for the research of this thesis it may be necessary to reduce the degree of reaction in order to limit the axial load.

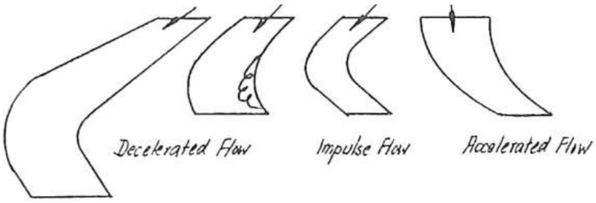

Figure 2.1: Qualitative representation showing large turning angles for radial inflow impulse turbines [32].

Although not backed-up by CFD simulations or experiments, in early research at the beginning of the 1960's by Knoernschild [32] it is argued that the deceleration of the flow in the rotor of an impulse radial inflow turbine in combination with the large turning angles as depicted in Figure 2.1 have a detrimental effect on the losses. Moreover, when reducing the degree of reaction, at some point part of the flow near the hub can get blocked or even flow backwards as a result of the reduced amount of head available. A reduction of the velocity ratio, defined as the ratio of the tip speed and the spouting velocity, will decrease the degree of reaction to a minimum and will then increase again as a result of the aforementioned effect.

No established methodology is defined in existing literature regarding the 1D design of sCO_2 radial inflow turbines. To explore the design space of the radial inflow turbine, zTurbo has been identified as an accessible design tool. zTurbo is a 1D design tool developed by Delft University of Technology as described in [33], which can evaluate turbines of the axial, radial inflow and radial outflow architecture. The tool can be coupled to the external thermodynamic libraries like Refprop [34] and Fluidprop [35], allowing for an accurate representation of the fluid behaviour in both the subsonic and supersonic domain. Several loss models are implemented in zTurbo and are summarised in Table 2.1, although they are based on conventional turbine data. Therefore, accurate CFD analyses are required to evaluate the turbine performance.

Table 2.1: Loss models summary.

Loss model	Type of model	Based on experimental data of
Soderberg [36]	Empirical	Axial machines with conventional working fluid
Craig - Cox [37]	Empirical	Axial machines with conventional working fluid
Traupel [38]	Empirical	Axial machines with conventional working fluid
Glassman [39]	Partly empirical and partly physics based	Radial machines
Baines [40]	Partly empirical and partly physics based	Radial machines

One of the effects that has been identified originating from changing the working fluid from an ideal gas to a refrigerant or supercritical fluid for the design of a radial inflow turbine, is the increased blade loading due to highly dense working fluids [6]. This also increases the passage to passage pressure differentials, thereby aggravating tip leakage effects. As a result, thicker blades are required to cope with the higher speeds and pressure loadings.

Wheeler and Ong [25] show that allowing the blade height to increase at the rotor inlet can reduce over-acceleration of the flow further downstream. This acceleration is due to the reduction in radius along the rotor channel and due to rotation, where the former dominates for subsonic blade speeds. The blade design method described by Jahn [41] uses the flow area to shape the rotor blades and therefore varies the blade height along the rotor channel accordingly.

Baines [42] describes the Coriolis effect which transfers the fluid in the rotor channel from the hub to the shroud. This effect is more pronounced at the suction side of the blade, as this is where the low momentum fluid is found. The secondary flows in the rotor channel, induced by the Coriolis effect, tip leakage flows and curvature of the blade, show to result in a region with high losses near the intersection of the suction surface and the shroud. Tip leakage flows are considered to be a main contributor to non-uniform flow at the rotor exit and corresponding losses [43]. Based on this, for maximising efficiency, an accelerating flow in a shrouded rotor channel would be desired. However, a low degree of reaction to keep the turbine axial load to a minimum requires a decelerating flow in the rotor channel.

Even nowadays the design space of the low reaction and low specific speed turbine is to a large extend an undiscovered region. Research of the last years showing the potential of using sCO_2 as a working fluid for CSP applications made this region of the design space an area of particular interest. The large fluid density of sCO_2 in combination with the limited rotational speed in this research pushes the design towards a low reaction turbine in order to have an acceptable axial load acting on the rotor.

2.2. SUPERCRITICAL CO_2 AND CONCENTRATING SOLAR POWER

The ability of making use of a thermodynamic cycle with the working fluid operating above its critical condition was identified by Angelino [1] and Feher [2] in the 1960's. Operating at these conditions allows for an efficient and compact cycle design. According to Feher, any fluid can be chosen in a supercritical cycle, but the operating pressures and temperatures of the cycle are defined by the working fluid. Although Angelino questioned the applicability of using carbon dioxide as a working fluid, Feher argued it to be a suitable working fluid because of its favourable characteristics:

- Lower operating pressures are allowed because of its low critical pressure of $7.38 MPa$.
- In the temperature range of interest for a power plant the material is stable and inert because of the strong covalent bonds.
- The material is abundant, non-toxic and relatively inexpensive.

Only one year later, Angelino [44] argues that the efficiency of an sCO_2 cycle is comparable to that of a reheat Rankine cycle when the turbine inlet temperature is above $650°C$ and has the benefit of its simplicity and compactness, especially at higher power levels. A comparison between the size of a turbine operating in an sCO_2, helium and steam cycle can be seen in Figure 2.2. The possible advantage in terms of cycle efficiency when using CO_2 as a working fluid opposed to steam, which is currently used in CSP systems, can be seen in Figure 2.3.

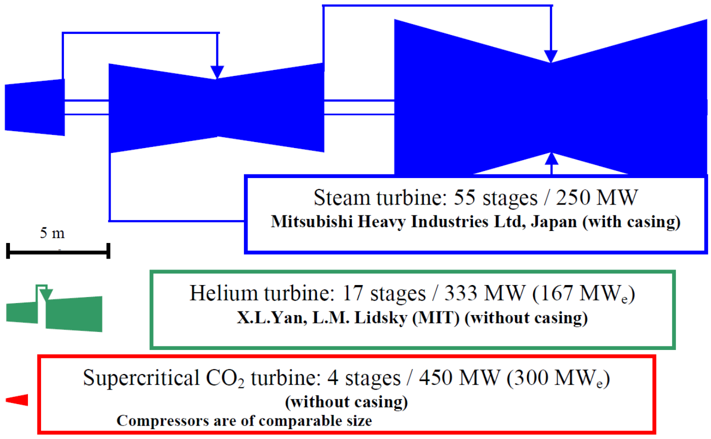

Figure 2.2: Turbine size comparison from sCO_2, helium and steam cycle [3].

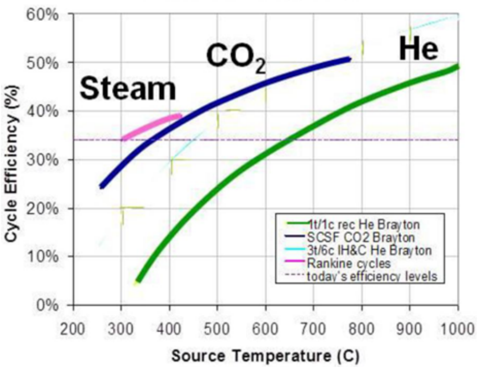

Figure 2.3: Cycle efficiency versus source temperature for different working fluids [45].

The research on sCO_2 cycles from the late 1960's and 1970's came to a stop and was not used in practice. According to Dostal [3], the main reasons for this were insufficient turbomachinery experience, heat exchangers which were not compact and heat sources having temperatures lower than the temperatures of interest for an sCO_2 cycle. Dostal argues that in the late 1990's studies on closed gas turbine cycles became a topic of interest, including investigations in the application of sCO_2 cycles, because the turbomachinery and compact heat exchangers experienced great advancements after Angelino's and Feher's research.

Fluid properties of CO_2 show significant variations near its critical point, which is $7.38 MPa$ and $30.98°C$. This principle is used to reduce the required compressor work, and thereby improve the efficiency of the cycle. Dostal showed that the turbine work is independent of the pressure at which the turbine operates. The

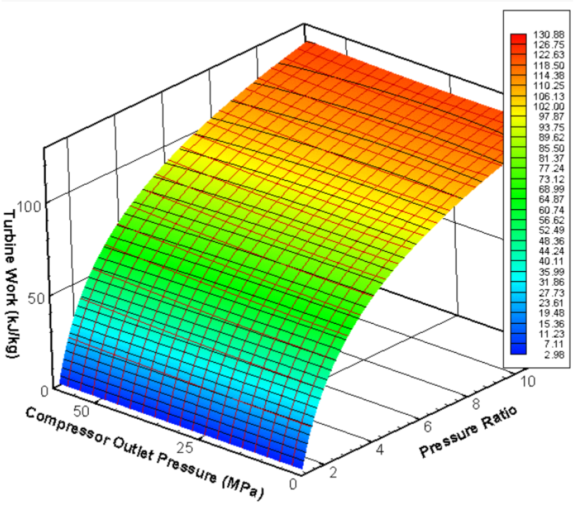

Figure 2.4: CO_2 specific turbine work as a function of compressor outlet pressure and pressure ratio [3].

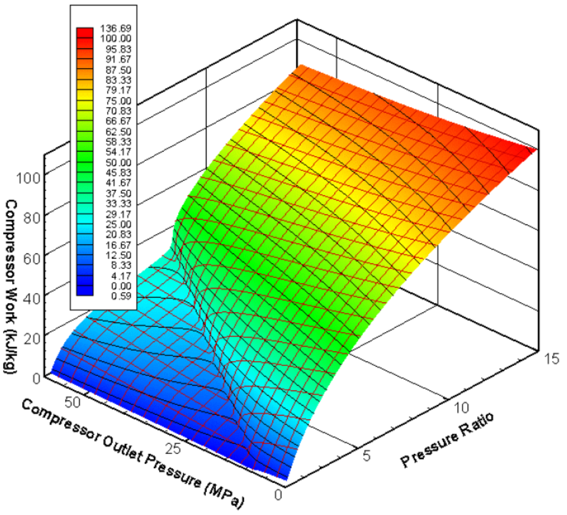

Figure 2.5: CO_2 specific compressor work as a function of compressor outlet pressure and pressure ratio [3].

expansion ratio does have an influence on the turbine work, but this influence becomes smaller at larger expansion ratios. This is illustrated in Figure 2.4. Dostal also showed that the compressor work is strongly dependent on the compressor inlet pressure, where a different trend can be observed just below and above the critical pressure of $7.38 MPa$. This is illustrated in Figure 2.5, where it can be seen that the compressor work at $32°C$ and 89% efficiency significantly reduces when approaching the critical pressure of $7.38 MPa$. The reason of the reduced compressor work is the low compressibility of the fluid near the critical point. This improves the compressor efficiency compared to compressing a fluid far from the critical point [3]. According to Dostal, compared to a helium Brayton cycle, an sCO_2 Brayton cycle can obtain similar efficiencies. However, the sCO_2 Brayton cycle can achieve this efficiency at a lower temperature of $550°C$ compared to $850°C$, but at a higher pressure of $20 MPa$ compared to $8 MPa$.

Over the years, several cycle configurations have been analysed. The configurations often considered are the simple Brayton cycle, partial condensation cycle, the precompression Brayton cycle, the recompression Brayton cycle and the partial cooling Brayton cycle. Angelino [44] shows the benefit in efficiency of a partial condensation cycle over a fully condensation cycle. He also recognises the benefit of using reheating in the cycle, thereby increasing the efficiency. Kulhanek and Dostal [46] show that the simple Brayton cycle is inferior to the precompression, recompression and partial cooling cycle across the range of turbine inlet temperatures. These findings show that adding complexity to the Brayton cycle by means of adding extra systems can have a beneficial effect on the efficiency of the cycle, where sometimes cycle efficiencies well above 50% can be found.

Using sCO_2 is considered for various applications like nuclear, waste heat, energy storage, clean coal combustion and also solar [47]. Making use of sCO_2 for CSP applications was identified by Yamaguchi et al. [4]. In a CSP plant, by using mirrors the solar radiation is concentrated, thereby heating up the working fluid. This drives the thermodynamic cycle, which can be used to generate electricity. One of the advantages of CSP systems over other methods of energy generation is the potential of using thermal energy storage, which has the benefit of being more efficient and less expensive than storage of electrical energy [18]. This increases the capacity factor and allows for a more efficient dispatch of power for electrical energy generation during night time or to increase the electrical power output at times of high demand. When using solar energy for generating both heat and electrical energy, efficiencies of 85% can be achieved [48]. Advantages of using sCO_2 as a working fluid for CSP opposed to current CSP applications include higher achievable efficiencies, good scalability and compactness [49]. Moreover, an sCO_2 cycle can be incorporated in a dry air cooling cycle instead of a cycle using water cooling, which is of particular importance for CSP as these systems are often located in hot and dry areas where water is not easily accessible [50]. Because of the smaller turbomachinery when using sCO_2, there could be a possibility to place the turbine on top of the CSP tower, which reduces the distance between the heat source and turbine, leading to a possible reduction in losses. For these reasons,

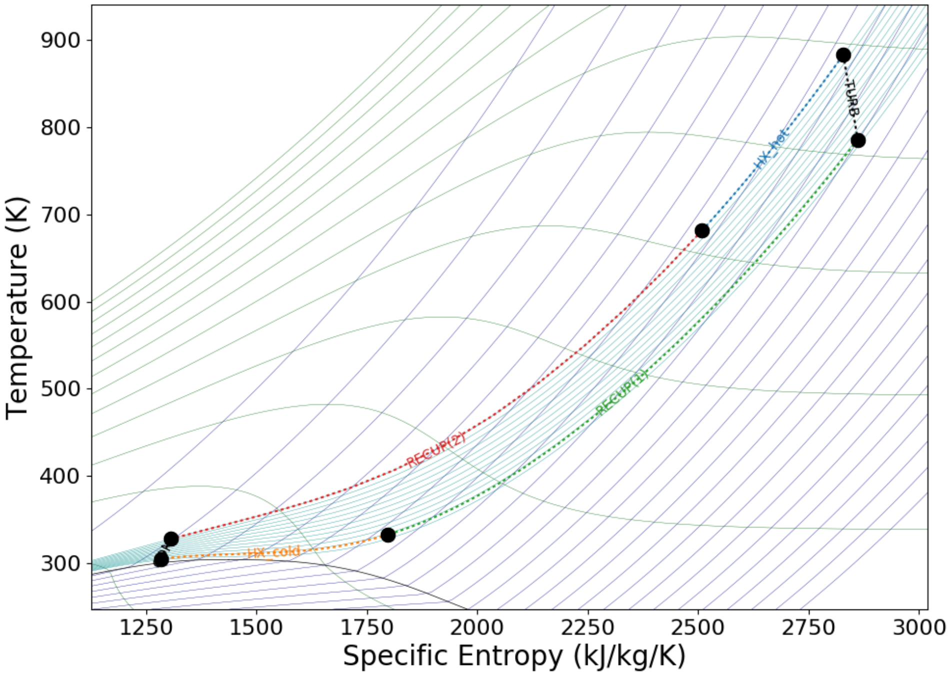

Figure 2.6: Overview of the reference regenerative sCO_2 thermodynamic cycle [5].

Table 2.2: sCO_2 turbine operating conditions comparison.

Parameter	Reference cycle [5]	Scaled cycle
Turbine output power $[kW]$	1128	300
Total inlet temperature $[K]$	883	823
Total inlet pressure $[MPa]$	20	20
Expansion ratio $[-]$	2.35	2.22

the application of an sCO_2 Brayton cycle in a CSP system is of interest for today's research.

The turbine of this research operates in a thermodynamic cycle which is based on a scaled form of the regenerative thermodynamic cycle as given by Jahn and Keep [5]. The temperature-entropy diagram of this cycle can be seen in Figure 2.6. The cycle as shown in Figure 2.6 corresponds to a turbine with an output power of approximately $1.1MW$, a total inlet pressure of $20MPa$, a total inlet temperature of $883K$, an expansion ratio of 2.35 and a mass flow rate of $10.22kg/s$. This cycle is scaled down to $300kW$ and there are small differences in turbine operating conditions, which are summarised in Table 2.2.

As can be seen in Figure 2.6 the compressor is operating close to the critical temperature of CO_2 of $304K$. According to Jahn and Keep, the non-linear properties in the region close to the critical point allow for efficient compression of the fluid, which can result in a higher cycle efficiency. These non-linear properties have to be modelled accurately for a good representation of the fluid behaviour. On the contrary, the turbine operates in a region far away from the critical point. It is argued that ideal gas properties can be used in this region for modelling the turbine [5] [51] [14].

2.3. CHALLENGES OF SUPERCRITICAL CO_2 TURBINE DESIGN

In this Section, the key challenges related to sCO_2 turbine design as identified in literature will be elaborated upon. The challenges that will be discussed are related to the turbine, but as the turbine cannot be seen as an isolated component, several challenges are introduced related to other components like the shaft or control systems. The main challenges that are identified are as follows, and will be discussed in more detail in this Section:

- Limited experience.

- Small turbine dimensions.
- High rotational speeds.
- High unit loading.
- Rotordynamics.
- Pressure containment.
- Integration with load control.
- Thermal management.
- Mechanical design.

LIMITED EXPERIENCE

One of the biggest difficulties at the moment regarding sCO_2 turbine design is the lack of experience. It is argued by Brun [49] in 2016 that, due to the lack of experience, the design of the turbine can be regarded as the highest risk component of an sCO_2 system. Mainly in the past decade several papers have been published describing the design of an sCO_2 turbine. These designs range from simple preliminary calculations to more detailed analyses and preliminary component testing in experimental cycles. As many of the preliminary calculations are done using in-house tools, often only little information is published on the details of the method of designing the turbine. An overview of sCO_2 turbine designs as found in literature including the output power, application and turbine architecture is summarised in Table 2.3.

From Table 2.3 it can be concluded that previous sCO_2 turbine designs mostly focus on multi-MW turbines, for which the axial turbine architecture is the preferred configuration. Only in recent years the interest arose in sCO_2 turbine designs for small power applications.

In Table 2.3 the turbine designs that have been subjected to some kind of real life testing have been highlighted in bold. Although useful insights have been gained during the experimental tests, due to problems encountered during testing of some of these turbines most of them have not been tested up to the design condition. This puts a limitation on the usability of the test results. Moreover, the amount of published turbine validation data from these experiments is very limited. This consequently leads to uncertainties in the methodologies and results as presented in existing literature on the design of sCO_2 turbines as they cannot be validated with experimental results. The level of detail in both the design of the turbine and the explanation in many of the publications as shown in Table 2.3 is rather limited and often the challenges in the turbine design as described in this Section are not or only to a limited extend taken into account. To generate validation data at reasonable cost, the turbine design of this thesis for low power applications and future experimental tests can be valuable information for future sCO_2 turbine design methodologies.

SMALL TURBINE DIMENSIONS

Compared to an open Brayton cycle operating with combustion gas turbines, the density of the fluid can be two orders of magnitude larger when using sCO_2 [49]. This has the benefit that cycle components like the turbine are greatly reduced in size, thereby bringing down for example capital investment and maintenance costs. However, this brings also challenges in proper turbomachinery design and increases secondary effects. According to Ahn et al. [50], the turbomachinery of an sCO_2 cycle can be 10 times smaller compared to a stream Rankine cycle. Due to the small distance between neighbouring components in small turbomachines, preventing excessive heat transfer between the turbine inlet housing and stator housing is a challenge [54]. Ahn et al. argue that, based on previous test results, the thermal efficiency of an sCO_2 cycle increases with increasing size, meaning that a cycle with a power output of over $10MW$ is required to have high efficiency turbomachinery while using conventional bearing and seal technologies. Many of the small power application turbines as presented in Table 2.3 have a good estimated efficiency. It will be interesting to see how keeping pressure differences across the turbine small in order to simplify seal and bearing design will influence the efficiency and operation of the turbine. Due to manufacturing tolerances, the leakage losses can be more severe for small sCO_2 turbomachinery compared to larger systems [60].

Table 2.3: sCO_2 turbine design in literature.

Author	Year	Power $[MW]$	Application	Axial turbine	Radial inflow turbine
Dostal [3]	2004	600	Nuclear	✓	
Gong et al. [52]	2006	300	Nuclear	✓	✓
Cha et al. [53]	2009	600	Nuclear	✓	✓
Wright et al. [54]	2010	0.125	Nuclear		✓
Persichilli et al. [55]	2011	0.25	Waste heat recovery		✓
Vilim [56]	2011	0.03	Nuclear		✓
Kimball et al. [57]	2012	0.1	Nuclear		✓
Utamura et al. [58]	2012	0.11	Nuclear		✓
Pasch et al. [59]	2012	0.178	Nuclear		✓
Pasch et al. [59]	2012	0.213	Nuclear		✓
Conboy et al. [60]	2012	0.092	Nuclear		✓
Muto et al. [10]	2014	100	CSP	✓	
Kalra et al. [11]	2014	10	CSP	✓	
Sienicki et al. [61]	2014	164	Nuclear	✓	
Held [62]	2014	2.7	Waste heat recovery		✓
Turchi [12]	2014	14	CSP	✓	
Zhang et al. [63]	2015	1.5	Nuclear		✓
Zhang et al. [63]	2015	15	Nuclear	✓	
Qi et al. [13]	2016	0.1	CSP		✓
Qi et al. [13]	2016	0.2	CSP		✓
Clementoni et al. [64]	2016	0.04	Nuclear		✓
Bidkar et al. [51]	2016	70	Coal	✓	
Bidkar et al. [51]	2016	610	Coal	✓	
Spazzoli [14]	2016	50	CSP	✓	
Cho et al. [65]	2016	0.082	Test		✓
Cho et al. [65]	2016	0.123	Test	✓	
Cho et al. [65]	2016	0.058	Test	✓	
Zhang et al. [66]	2017	15.9	Nuclear		✓

According to Brun [49], overspeed is of particular importance for sCO_2 turbines due to the small turbine size and low inertia in the rotor, possibly leading to sudden losses of load. The experience with control systems to prevent overspeed in sCO_2 systems is limited, although the research of Pasch et al. [59] reports about the installation of overspeed resistors in the sCO_2 test loop. To mitigate the risk and implications of overspeed, the turbine should be designed for a rotational speed that is 20% larger than the design operating speed.

In the research of Zhang et al. [63] it is recognised that along the fluid path in the turbine rotor the pressure difference across the blade decreases at the hub surface, whereas this difference increases at the shroud. As a result, the leakage losses at the tip clearance near the end of the rotor channel are more severe than near the inlet of the rotor channel. Therefore, the tip clearance at the trailing edge has a large influence on the aerodynamic performance of the radial inflow turbine compared to the tip clearance at the leading edge. This confirms the conclusion of Dambach et al. [67], who found that there is a smaller amount of tip leakage near the inlet of the rotor due to tip scraping. They argue that because of the higher tip gap loss in the exducer of the radial turbine, the effect of increasing the radial clearance on the stage efficiency of a radial inflow turbine is larger compared to an increase in the axial clearance. As the tip clearance of small turbomachines is relatively large, tip clearance losses are expected to have an important contribution to the total turbine losses.

According to Wright et al. [68] the power a system generates scales with the radius squared, whereas leakage flow scales linearly with the radius. This means keeping the fractional leakage losses low will be easier to achieve in large power systems, but it will be an extra challenge for small-scale turbomachinery.

HIGH ROTATIONAL SPEEDS

Kimball and Clementon [57] show how the turbine dimensions and rotational speed are related as a function of output power. As shown in Figure 2.7, when using existing design wisdom for small power levels, the turbine dimensions tend to get extremely small with high corresponding rotational speeds. This is a result of the desire to operate at an optimal specific speed and specific diameter. Similar as to the specific speed as introduced in Section 2.1, the specific diameter is a non-dimensional parameter which can be used to estimate the turbine performance based on empirical relations. The high rotational speed is closely related to the small turbine dimensions as described before. Based on this, it can be concluded that a compromise may have to be found regarding specific speed and specific diameter in relation to turbine operating conditions and efficiency.

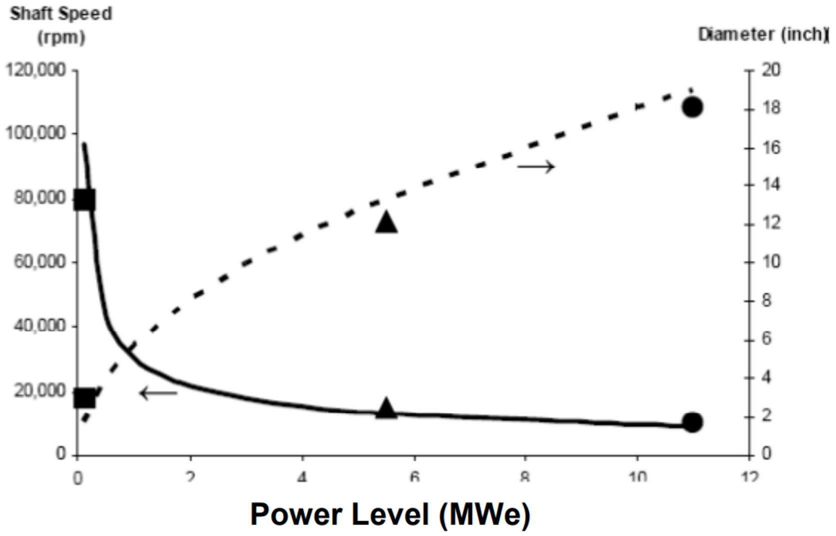

Figure 2.7: Relation between output power and rotational speed and turbine dimensions [57].

Bidkar et al. [51] mention that high rotational speeds are desirable from a turbomachinery point of view. However, as bearings are limited to a maximum surface speed of the shaft, a higher rotational speed would mean that the diameter of the shaft has to be reduced. As the torque capability of the shaft is related to the shaft diameter, a higher rotational speed results in a lower power capability. It is argued by Wright et al. [54]

that if the design rotational speed exceeds $60krpm$, the limiting factors to the shaft speed are bearing heating, windage friction and stator winding temperature. Increasing the rotational speed to higher values requires more advanced cooling, insulation, bearing heating and thrust load balance. As a result, the turbine in the research of Wright et al. operates at a specific speed of 0.38, which is lower than the ideal value. The design total-to-static efficiency however is still well above 80%, indicating that limiting the turbine rotational speeds can still result in acceptable efficiency levels. This is in line with observations of Gong et al. [52] who showed that an efficiency of 85% is expected to be achieved for a turbine operating with a specific speed of 0.32. As these are just preliminary results, for turbines with a rotational speed constraint, which are thereby limited to a maximum achievable specific speed, exploring the low specific speed design space in more detail would be an area of interest.

Results of Utamura et al. [58] showed that windage losses are a large contributor to the total turbine losses, as the windage loss scales with rotational speed to the power three. However, windage losses scale with the radius of the rotor to the power four. This means that trying to reduce the rotational speed by increasing the rotor size may not have the desired effect in terms of reduction in windage losses. It is concluded by Utamura et al. that windage losses have to be reduced in order to make use of sCO_2 power cycles in practice. As noted by Conboy et al. [60] windage losses are expected to be less of a problem for commercially large sCO_2 power systems due to the possibility of using a gearbox. Windage losses are also by Pasch et al. [59] considered to be an area that requires attention. This stresses the importance of trying to reduce the rotational speed of the turbine. Care must be taken when using existing relations for estimating the windage losses. According to Wright et al. [68], the relations currently used to estimate the windage losses are based on empirical relations of air and steam driven turbines. By comparing windage loss measurements of sCO_2 experimental data to the predicted values, it is confirmed by Wright et al. that existing relations give a good approximation of the actual windage losses at $35krpm$. When increasing the rotational speed still a good agreement is found, although the difference between the measured and predicted windage losses increases with rotational speed. Currently, research on windage losses in sCO_2 systems is ongoing at the University of Queensland's Geothermal research group in parallel to this thesis but is unpublished to date.

For extremely small power applications in the order of $1kW$ of electrical output power, Cho et al. [65] showed that an unrealistically high rotational speed of $800krpm$ would be required. As it is impossible to operate a turbine at these speeds, use has been made of a partial admission nozzle to block most of the flow. As a result, the turbine can operate at $200krpm$ when only a single passage of the nozzle is opened.

Research of Clementoni et al. [64] showed that a rotational speed of $75krpm$ would omit the possibility of using dry gas seals or other seals which can completely seal the shaft. As a result, all components which are located on the shaft are within the pressure region. Moreover, at a later stage the rotational speed is reduced to $60krpm$ due to difficulties in maintaining acceptable bearing and stator temperatures induced by windage and rotor losses. The windage losses of the turbine are twice as large as initially anticipated, thereby consuming more than 25% of the generated turbine power. This is due to the increased pressure gradient in the cavity as a result of cavity cooling to reduce bearing and stator temperatures. The effect of rotational speed on windage losses can be seen in Figure 2.8, where an increase in windage losses with increasing pressure and with increasing rotational speed can be observed. Moreover, the discrepancy between the estimated and measured windage losses by Clementoni et al. becomes evident from Figure 2.8. It is argued by Wright et al. [68] that dry-liftoff seals, which can reduce the leakage by about an order of magnitude compared to labyrinth seals, are more expensive and are usually not operated at shaft speeds used in sCO_2 turbine designs. When using fluid film bearings, the shaft surface speed in the design is often limited to $91m/s$ to keep the heat generation to acceptable levels [49]. Gas bearings can be used for higher surface speed applications, but this type of bearing may be unable to cope with the high turbine loading as will be discussed later.

HIGH UNIT LOADING

Brun [49] expects the high unit loading to originate from several sources for sCO_2 turbines:

- Pressure difference across the rotor.
- Asymmetric pressure difference across the rotor.
- Transient loads.

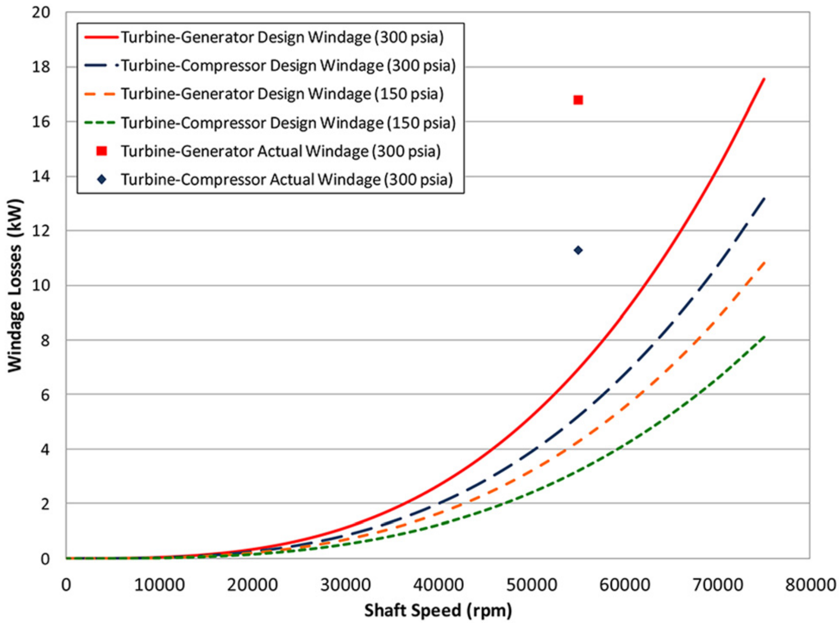

Figure 2.8: Relation between windage loss and rotational speed [64].

- Lateral forces in the gearbox.

The asymmetric pressure difference across the rotor often originates from off-design operation as a result of varying compressor operating conditions. As the turbine of this thesis will be operated in a controlled cycle instead of in a CSP system, one has got more control over off-design operating conditions and therefore this asymmetric pressure difference. As the turbine of this thesis operates without a gearbox, the last bullet point is also not a concern for this project, but should be taken into consideration when designing sCO_2 turbines for large-scale operations. Transient effects will be discussed later. One of the bigger concerns, also according to other literature, is the force induced by the pressure difference across the rotor [50] [51] [58].

Because of the high fluid density of sCO_2 in the operating region, a significant axial load can be generated across the turbine which is transferred through the shaft and has to be supported by thrust bearings [58]. In literature, several solutions are proposed to reduce the axial load induced by this pressure difference, which will shortly be elaborated upon below:

- Use twin impeller turbomachinery.
- Use of labyrinth seals.
- Adding cutouts to the turbine wheel.
- Use a low degree of reaction turbine.

In an attempt by Ahn et al. [50] to balance the thrust forces acting on the system, use has been made of a twin impeller compressor. This means two identical rotor wheels are used to cancel each other's generated axial load. A similar approach could be used for the turbine, as is done in the research of Bidkar et al. [51]. However, this will have the disadvantage for low power applications of reducing the mass flow rate, which is already low, to even lower values. This will aggravate the challenges as described before related to the small turbine dimensions. Therefore this is not considered to be a feasible solution for low power sCO_2 applications.

A shrouded turbine wheel with labyrinth seals at both sides of the wheel is designed to solve thrust balancing problems induced by the high pressure fluid as can be seen in Figure 2.9 [65]. By using a shrouded turbine with labyrinth seals, the high pressure fluid at the inlet of the turbine can access the gap between the turbine and the housing, which is present at both sides of the turbine near the inlet. By allowing the high pressure fluid to enter the gaps at both sides of the turbine, most of the force induced by the high pressure

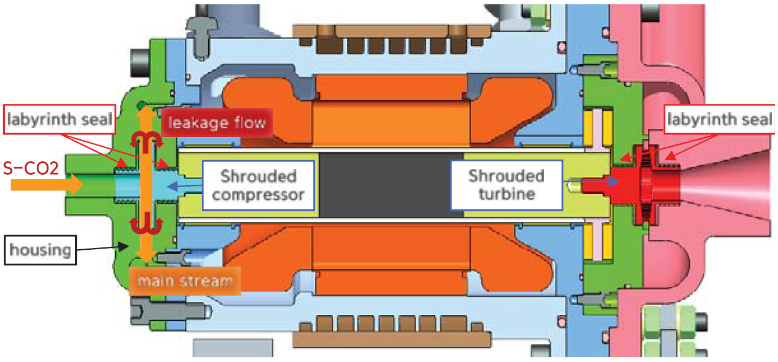

Figure 2.9: Usage of a shrouded turbine with labyrinth seals to balance axial loads [65].

fluid acting on the rotor wheel will be cancelled.

For balancing the axial forces, a possible solution that is used by Wright et al. [54] is adding cut outs to the turbine wheel. Based on experimental measurements, the thrust load on the turbine is determined. Based on this axial load, cut outs are made at the base of the turbine wheel, which are used to change the area the high pressure fluid is acting on. Implementing the right size of cut outs can be used to balance the thrust loading of the turbine. As these cut outs are made after testing and by trail and error, this solution is not considered to be interesting for the current research project.

The high rotational speed and high axial force of the $60kW$ turbine as designed and tested by Cho et al. [65] resulted in failure of the turbine. In an attempt to overcome this issue, a new turbine is designed which is an axial impulse turbine operating at $45krpm$. As described in Section 2.1, in an impulse turbine almost all of the expansion happens in the stator, thereby reducing the pressure difference across the rotor to low values or even towards 0. Because of the low mass flow rate, a partial admission nozzle is used. As already identified in Section 2.1, research by Fridh et al. [30] showed a reduction in the total-to-static efficiency for lower degrees of admission. Therefore, the use of partial admission turbines should be avoided if possible.

The high unit loading brings challenges to the design of shaft journal and thrust bearings in an sCO_2 system in order to be able to cope with both the radial and axial loads induced by the aforementioned sources [57]. Conboy et al. [60] identify the benefits of using gas foil bearings for small turbomachinery operating at high rotational speeds, although the lack of experience with this kind of bearing for sCO_2 applications is considered to be a risk for industrial applications that has to be overcome by conducting research and experiments on foil bearings in high density sCO_2 applications. The high unit loading in combination with high operating temperature will put limitations on gas foil bearings. Due to the high pressure of the fluid, small discrepancies between the design and actual operating conditions can have a large influence on the axial load [49]. As a larger axial force would require larger thrust bearings, the surface speed of the thrust bearings increases, leading to possible hot regions near the bearing. According to Wright et al. [68], the heating of the bearing scales linearly with the fluid density, which causes difficulties for sCO_2 systems because of its high density. Cho et al. [65] solved this by using labyrinth seals to separate the bearing chamber from the turbine chamber. This allows using ball bearings which operate at atmospheric pressure. This does however have a negative effect on leakage losses, as the high pressure CO_2 will flow through the labyrinth seals, therefore requiring a constant addition of CO_2 to the loop to compensate for the leakage. Wright et al. [68] used additional pumps to lower the pressure, and thereby density, in the rotor cavity region.

ROTORDYNAMICS

The combination of high fluid density, high power density and high temperatures poses a unique challenge for sCO_2 systems due to the swirl of the highly dense fluid around the turbine components [49]. Additional damper bearings, damper seals or swirl brakes may be required to mitigate the rotordynamic instability. This instability is caused by tangential forces, inducing vibrations with increasing amplitudes.

Indirectly related to the turbine are the rotordynamic instabilities of the shaft connecting the turbine to the compressor or generator [49]. Due to high turbine temperatures, an improved thermal system compared to conventional power systems has to be incorporated into the design in order to keep temperatures at acceptable levels. Moreover, the high axial loads as discussed before require a more advanced balance piston seal. Both the thermal and balance system require additional space and thereby lead to a larger shaft length, which decreases the rotordynamic stability of the system.

Bidkar et al. [51] show the importance of doing a rotordynamic analysis. It is noted that care has to be taken that the different modes of the undamped critical speed map have a sufficient margin with the actual rotational speed. Evaluating the rotordynamic stability of the complete power system of which the turbine of this thesis will be part of, is a required analysis before the components can be built and tested. As this stability is dependent on many more components than the turbine only and is especially important for the shaft design, evaluating the rotordynamic stability is outside of the scope of this thesis. However, as the shaft diameter has a large influence on both the rotordynamic stability and the thrust loads due to the atmospheric back pressure at the end of the shaft, care has to be taken in selecting the shaft dimensions and use this accordingly in turbine design calculations.

PRESSURE CONTAINMENT

Compared to supercritical steam turbines, the temperature and pressure at the inlet are similar as found in sCO_2 applications, but the outlet pressure and temperature are higher [49]. It is argued that the high outlet pressure and temperature in combination with the need of using dry gas shaft end seals in sCO_2 systems lead to a high temperature gradient. Consequently this puts extra requirements on seal design.

Bidkar et al. [51] mention that using labyrinth seals for systems with a large diameter and a large pressure differential is commonly used. For the sCO_2 system analysed, using labyrinth seals shows leakage flows of about an order of magnitude larger than the desired value. Therefore, it is recommended to develop dry gas seals which are able to operate with large diameter shafts in operating conditions as seen in an sCO_2 cycle to reduce leakage losses. This is in line with the conclusions made by Wright et al. [68] as discussed before.

INTEGRATION WITH LOAD CONTROL

During testing, as well as during operation when demand or thermal resource is limited, part-load and off-design operation are important effects to take into account during turbomachinery design [49]. These operating conditions can have an effect on the stability and efficiency of the system. Regarding the turbine, to extend the operating range variable nozzles can be incorporated into the turbine design to be able to adapt the turbine operation to the operating conditions. Although off-design and part-loading mitigation strategies have been used in many applications, the experience in using this in high pressure sCO_2 applications is limited. As the turbine of this thesis will be operated in a controlled cycle instead of in a CSP system, there is going to be more control over off-design operating conditions, thereby limiting the need of using a variable turbine geometry.

THERMAL MANAGEMENT

Due to the high heat transfer coefficient of CO_2 in the supercritical region and high turbine operating temperatures, a well-designed thermal management system is required to bring the temperatures down to acceptable levels for seals and bearings, as well as to reduce the thermal stresses in the turbine [49]. Because of rotordynamic stability issues as discussed before and reduced shaft diameters to get acceptable surface speeds for seals and bearings, the thermal management for sCO_2 systems introduces additional challenges.

Moreover, transient effects can aggravate the thermal complications in sCO_2 turbines which occur during start-up and shut-down of the system. This will have an effect on thermal stresses and therefore component life, including the life of for example seals. These effects have to be taken into account when operating the sCO_2 turbine system and one of the proposed solutions to mitigate this effect is to make use of preheating of critical components. As the start-up and shut-down transient effects are dependent on the power system and not just simply on the turbine, considering the current stage of the cycle and component designs, taking into account transient effects during start-up and shut-down is considered to be outside of the scope of this thesis project.

MECHANICAL DESIGN

Because of the high torque requirements of sCO_2 turbines, special attention has to be paid to the connection of the turbine to the shaft. Fitting the wheel on the shaft by shrinking the wheel, which is a method that is often used for power cycles, is likely to be insufficient for sCO_2 applications as the induced friction may not be large enough to transfer the torque [49].

Kalra et al. [11] describe the method of designing a $10MW$ turbine for an sCO_2 CSP system. Mechanical design analyses are performed to give insight in the levels of static stress due to rotation. As a result, the need of minimising blade heights and tip diameters is identified. Also, because of the highly dense CO_2, there is a need for mechanical robust blade designs as a result of the large bending stresses on the blade. According to Zhang et al. [63], the high fluid density of sCO_2, which is in the order of 50-100kg/m^3 during the turbine working process, will have an effect on the blade load. During the mechanical design it is therefore recommended to take into account both the centrifugal forces due to rotation and the blade pressure loading. These stresses should be compared to the ultimate tensile, yield, creep and rupture properties of the material [51]. The design challenges as identified by Kalra et al. due to the high power density of CO_2 in compact turbomachinery include high torque admission requirements, manufacturing issues for small turbine geometries and the high cycle fatigue life of the rotor.

When using an axial turbine, additional challenges arise as identified by Kalra et al. [11]. Traditionally, dove tail slots are used to connect the blade to the shaft, which will damp vibrational forces due to the friction in these slots. Because of the high power density of sCO_2, an integrated blade-shaft module has to be used which does not damp the vibrational forces. To damp these vibrational forces, use can be made of so called z-locks which are machined into the shroud of the blade. However, due to requirements on small tip gaps and manufacturing limitations, these are not considered to be feasible. As a result, the vibrational forces are only damped by material damping. In this case, evaluating the natural frequency of the components in the turbine and designing with sufficient margin has to be done carefully.

Moreover, Kalra et al. [11] show the importance of analysing the effect of transient temperatures on the stresses in the turbine, for example during the event of a sudden cloud, start-up or shut-down of the system as already has been described before. For this application, it should be confirmed that the peak stress located at the blade shroud is lower than the allowable stress.

3

METHODOLOGY FOR SUPERCRITICAL CO_2 TURBINE DESIGN

This Chapter serves to give an overview of the design methodology that will be used to design and evaluate the sCO_2 turbine of this thesis project. This includes a brief explanation of the main steps taken during the design and how these link together in the overall process. An overview of the design process can be seen in Figure 3.1. A more detailed explanation of each module can be found in the following Chapters. In Chapter 4 the preliminary design will be explained in detail. In Chapter 5 the procedure for the aerodynamic design and mechanical stress evaluation will be elaborated upon. A user manual is written to use this methodology in future turbine design [69].

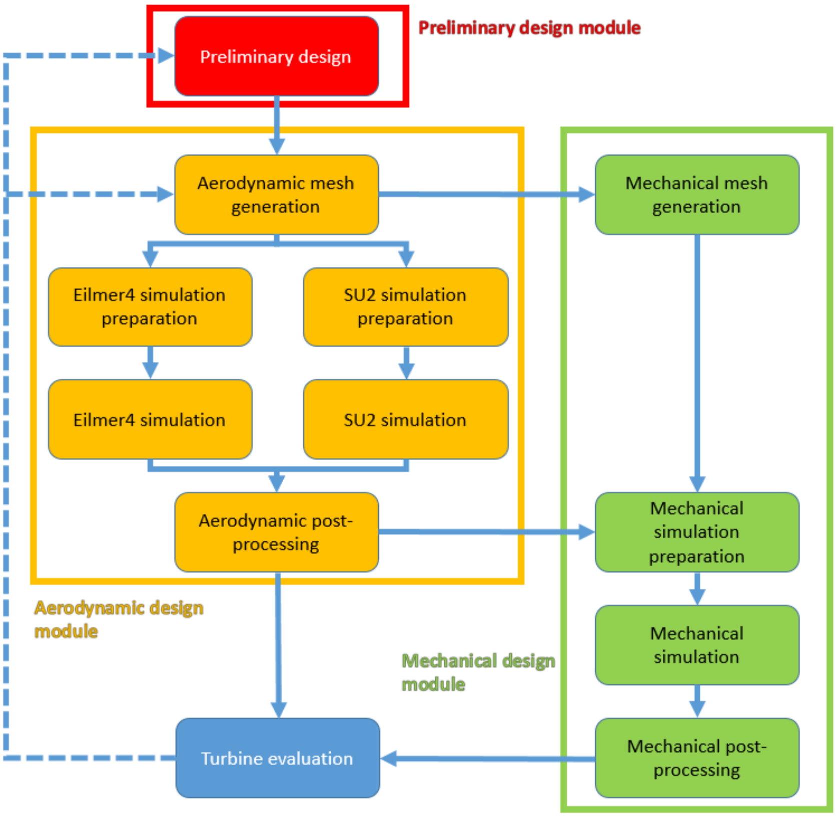

Figure 3.1: Turbine design methodology overview.

The first step in the turbine design process is to perform a meanline design, also referred to as a 1D design or preliminary design. The preliminary design module is represented by the red module as seen in Figure 3.1. This step allows for a quick evaluation of the estimated performance of a large range of turbine architectures and shapes. The software tool zTurbo will be used for this step. zTurbo is a 1D design tool for turbomachinery developed by Delft University of Technology. By using a Matlab script, a large number of turbine design variables can be varied in an automated way, thereby allowing for evaluating a large design space. As zTurbo is able to estimate the performance of different turbine architectures, the estimated performance for different turbine architectures for low power sCO_2 turbines can be assessed. Based on the results of the preliminary design, a decision will be made on the turbine architecture and the 1D design parameters, which will serve as a base for the 3D aerodynamic design.

The preliminary design is followed by a detailed aerodynamic design. The aerodynamic design module is represented by the yellow module as seen in Figure 3.1. This step allows for getting a detailed insight into the flow behaviour in the turbine and corresponding turbine performance. To get these results, a steady-state or a transient CFD simulation can be used. In a steady-state CFD simulation, the Reynolds-averaged Navier-Stokes (RANS) equations are solved to obtain a steady-state solution [70]. In a transient CFD simulation, the Navier-Stokes equations are solved for each time step, thereby taking into account transient effects [71]. The disadvantage of a transient simulation that it is more computationally expensive compared to a steady-state simulation. The aerodynamic solver SU2 will be used for the steady-state CFD simulation [70]. The aerodynamic solver Eilmer4 will be used for the transient CFD simulation [17]. Eilmer4 is the University of Queensland's open-source transient CFD solver with main applications in hypersonics, but has the capability of evaluating turbomachinery flows using a sliding interface. As this thesis project is the first time Eilmer4 will be used to analyse a turbomachinery component, developing and testing design tools is required to make Eilmer4 a suitable aerodynamic solver for turbomachinery applications as will be discussed in Chapter 5. By evaluating both the steady-state and the transient solution, the necessity of using a computationally expensive transient solver compared to using a relatively quick and simple steady-state simulation for the low power sCO_2 turbine design can be assessed.

As can be seen in Figure 3.1, the first step in the aerodynamic design process is to create the aerodynamic mesh. Whereas traditionally turbine meshes are based on the shape of the blade, the method for generating the mesh for this thesis will result in a structured grid of which the shape is based on aerodynamic parameters like flow area and flow direction [41]. This step of the design process includes extending the capabilities of the mesh generation tool to improve the modelling power of the tool and make it compatible with the CFD solvers as will be explained in detail in Chapter 5. The next step is to prepare and run both the steady-state and the transient CFD simulation. Post-processing tools will be created that can be used to analyse and compare the results of both CFD analyses.

Parallel to the aerodynamic design, a mechanical stress evaluation for the turbine rotor is done. The mechanical design module is represented by the green module as seen in Figure 3.1. This step allows for getting a detailed insight into the stresses in the rotor, originating from both centrifugal loads and fluid loads due to the high density sCO_2 in the turbine. The first step is to create a tool and establish a procedure to create a mechanical mesh based on the aerodynamic mesh which has been created in the aerodynamic design module. As the aerodynamic mesh represents the fluid domain, the edges of this mesh correspond to the blade, hub and shroud geometry. The mechanical mesh generation tool is an extension of the aerodynamic mesh generation tool and uses the software Solidworks to create the mechanical model. This can be loaded into ANSYS Workbench to do a steady-state structural analysis. Apart from the centrifugal loads induced by the rotation of the rotor, the loads on the blade and hub surfaces as estimated in the aerodynamic design module are used to take into account the pressure loading. The effect of the pressure loading from the steady-state CFD simulation and the pressure loading from the transient CFD simulation on the mechanical stresses can be evaluated. Based on this, the transient effects on the turbine loading can be evaluated and therefore again the necessity of doing a computationally expensive transient simulation compared to doing a steady-state simulation for the low power sCO_2 turbine design can be assessed. The result of the mechanical design module will be a detailed evaluation of the turbine loading.

The results of the aerodynamic and the mechanical design module can be used to evaluate the turbine concept. The turbine evaluation and the knowledge gained during the design can be used for a redesign of the turbine, starting either from the preliminary design or the aerodynamic mesh generation.

In this thesis, three turbine designs will be done. These designs will be referred to as the Generation 1, Generation 2 and Generation 3 turbine design respectively. An overview of the steps taken in each of these designs can be seen in Table 3.1, which relate back to the methodology overview as shown in Figure 3.1. These steps and corresponding results will be discussed in more detail in Chapters 4, 5 and 6.

The Generation 1 turbine starts with a preliminary design and this is followed by an aerodynamic design using SU2. As the efficiency of the turbine is lower than expected, the Generation 2 turbine is a redesign of the Generation 1 turbine, starting from the preliminary design. This design is used to compare the aerodynamic results from the SU2 and Eilmer4 simulation. The Generation 3 turbine uses the same rotor as the Generation 2 turbine, but the stator throat has been increased in order to increase the mass flow rate to the design value of $3kg/s$. This is done by going back to the aerodynamic mesh generation. Because of the agreement between the results of the SU2 and Eilmer4 simulation for the Generation 2 turbine, the aerodynamic design of the Generation 3 turbine is done using SU2. This design is extended with an evaluation of the mechanical stresses. Moreover, the performance of the Generation 3 turbine will be compared to a turbine design from literature and will also be evaluated at off-design operating conditions.

Table 3.1: Turbine design generations overview.

Turbine design	Preliminary design	Aerodynamic design	Mechanical stress evaluation
Generation 1	✓	✓ SU2	X
Generation 2	✓	✓ SU2 and Eilmer4	X
Generation 3	X	✓ SU2	✓

4

PRELIMINARY DESIGN

In this Chapter the preliminary design will be elaborated upon as part of the overall turbine design process as explained in Chapter 3 for the Generation 1 turbine. First, in Section 4.1 the operating conditions and requirements as set by ASTRI will be given. This is followed by a verification of the 1D design tool in Section 4.2, to assess the ability of the design tool to design small power sCO_2 turbomachinery. In Section 4.3 the design space exploration will be presented. This Chapter will conclude with a summary of the selected turbine concept in Section 4.4.

4.1. OPERATING CONDITIONS AND REQUIREMENTS

The conditions at which the turbine will be operating are summarised in Table 4.1. These conditions are fixed, as they are defined by the sCO_2 cycle as explained in Section 2.2.

Table 4.1: Turbine operating conditions.

Parameter	Value
Operating fluid	CO_2
Total inlet temperature	$550^{\circ}C$
Total inlet pressure	$20MPa$
Static outlet pressure	$9MPa$

The additional requirements which are set in order to operate the turbine in the existing test loop are summarised in Table 4.2. The turbine has to be able to be tested in 2018.

Table 4.2: Turbine requirements.

Parameter	Value
Rotational speed	$\leq 50{,}000rpm$
Power	In between $75kW$ and $300kW$
Flare angle	$\leq 30^{\circ}$
Rotor inlet blade height	$\geq 0.9mm$

The maximum rotational speed is set to $50{,}000rpm$ to ensure good operation in the test cycle in combination with the other components of the system. The power should be as high as possible, since this increases the size of the turbine and therefore makes the design more benign. Also, a higher power is expected to give more confidence in scaling to an even higher output power. The maximum power is $300kW$ in order for the turbine to be suitable for operating in the cycle. A power lower than $75kW$ is expected to be too low in order to use the results for scaling to a higher power. According to Dixon and Hall [72] the specific speed of a radial turbine should be between 0.5 and 0.9 for optimal performance and according to Japikse and Baines [73] the specific speed should lie between 0.2 and 0.6 for a radial inflow turbine. However, this is not a requirement of the turbine that will be fixed, but should be taken into account during the design. To prevent flow separation and corresponding large losses, the stator flare angle of all turbine architectures, as well as the rotor flare angle of the axial turbine, have a maximum value of 30° [33]. The rotor inlet blade height has a minimum value of $0.9 mm$ in order to prevent excessive losses and unmanufacturable blades [13].

For the design, a minimum value for the stator-rotor clearance of 10% of the stator chord will be used [33]. Because of the large pressures at the inlet and outlet of the turbine of $20 MPa$ and $9 MPa$ respectively, the axial load on the rotor wheel resulting from this pressure difference can easily exceed values in the order of $10 kN$ when using existing design wisdom. Therefore, the axial loads should be as low as possible in order to use conventional bearing technologies.

4.2. VERIFICATION OF THE 1D DESIGN TOOL

As no detailed experimental data on sCO_2 turbines has been published to date, it is decided to verify the results of zTurbo by doing a comparison with a preliminary design of an sCO_2 turbine from Qi et al. [13] to get more confidence in the ability of zTurbo to evaluate a small power sCO_2 turbine. The power output and mass flow rate in the work of Qi et al. are of the same order as the conditions of this thesis and is therefore considered to be more representative of this research compared to other multi-MW turbines.

The parameters as directly taken from the research of Qi et al. are summarised in Table 4.3. Moreover, the flow is assumed to enter the stator radially. Since no further details of the stator are given, the stator inlet blade height is assumed to be $1 mm$.

Table 4.3: zTurbo verification parameters [13].

Parameter	Value
Mass flow rate	$2.08 kg/s$
Number of stages	1
Rotational speed	$113000 rpm$
Total inlet temperature	$560°C$
Total inlet pressure	$20 MPa$
Static outlet pressure	$9 MPa$
Stator outlet angle	71.98°
Rotor relative outlet angle	-56.91°

Since the input and output parameters of the design tool used in the work of Qi et al. and zTurbo are not the same, some of the inputs of zTurbo have to be calculated based on the inputs and outputs of [13]. The inlet blade height-to-diameter ratio, stator inlet-to-outlet diameter ratio, stator-rotor diameter ratio and rotor inlet-to-outlet diameter ratio is chosen such that the rotor inlet radius is equal to the reference value of $28.7 mm$. The fluid properties are taken directly from the Refprop database [34]. The Traupel loss model is used because this is a widely used empirical model [38]. Although this loss model is based on axial turbine data, it has shown good results for radial outflow turbine designs in the past [74]. For this comparison, it is decided to not use the Glassman loss model [39] or the Baines loss model [40], which are both based on radial inflow turbine data as seen in Chapter 2, because when using these loss models, zTurbo fails to estimate the turbine performance.

A comparison between the results of Qi et al. and the zTurbo analysis can be seen in Table 4.4. From Table 4.4 it can be concluded that there is a difference in estimated efficiency of over 3%. This makes the validity of the Traupel loss model questionable for small scale radial inflow sCO_2 turbines. As the Glassman loss model and Baines loss model cannot be used for the design space exploration because of the aforementioned reason, it is important to re-evaluate the results of the design space exploration of the radial inflow turbine with the Glassman or Baines loss model.

4.3. DESIGN SPACE EXPLORATION

To explore the design space in a quick and systematic way, a Matlab program is written that varies the input parameters, writes the zTurbo input script, runs zTurbo and collects the results. This tool is explained in more detail in Section 4.3.1. The input parameters of the Matlab program will be specified in Section 4.3.2.

Table 4.4: zTurbo sCO_2 results comparison.

Parameter	Qi et al. [13]	zTurbo	Difference
Output power	$200kW$	$207kW$	3.5%
Total-to-static efficiency	80.4%	83.4%	3.7%
Degree of reaction	0.5	0.54	8.0%

The results of the preliminary design will be presented and discussed in Section 4.3.3.

4.3.1. METHOD

An overview of the created Matlab tool can be seen in Figure 4.1. The program runs from the main file, which in turn reads the input parameters as specified by the user. The Matlab tool is able to run a single geometry/condition or to execute zTurbo multiple times while varying the input parameters over a specified range. Executing zTurbo multiple times will in this Section be referred to as iterating. This tool allows for evaluating a large number of different geometries and loading conditions, thus allowing to gain insight into the effect of these changes on for example efficiency and axial load.

An input file is written in the zTurbo format based on the user inputs. After zTurbo is executed, a tool is called to evaluate the turbine performance, including an estimation of the axial load. The axial load is approximated by adding the force due to the pressure difference between the rotor inlet and outlet and the force due to the momentum increase of the flow. Finally, after evaluating the turbine performance, the meanline turbine geometry can be plotted to allow for a visual check. When exploring the design space, these steps are automatically repeated for every combination of the input variables. The results are summarised in an output file, which can be used to evaluate the effect of changing a parameter on the turbine performance.

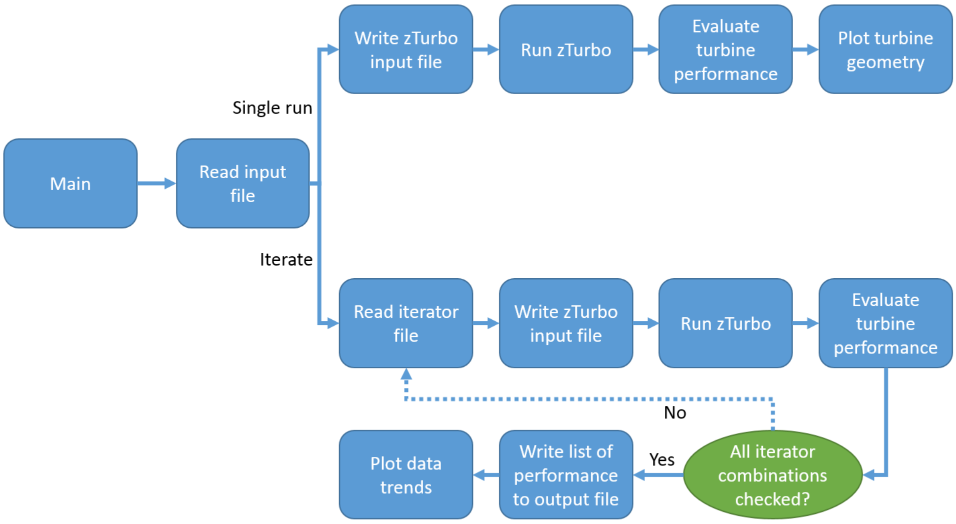

Figure 4.1: Matlab zTurbo runner architecture.

For an axial turbine, the force due to the pressure difference can be calculated using Equation 4.1. As can be seen in Equation 4.1, the change in area across the rotor blade is assumed to experience a pressure equal to the average pressure of the inlet and outlet. The area of the shaft is assumed to have an atmospheric back pressure. If the shaft is located at the low pressure side of the turbine, the disadvantage is that the pressure acting on the area of the shaft is equal to the high turbine inlet pressure, but this configuration allows for less complicated seals as the shaft is located in the low pressure area. If the shaft is located at the high pressure side of the turbine, the advantage is that the pressure acting on the area of the shaft is counteracting the force created by the pressure difference in the turbine and will therefore result in a lower axial load. The inlet and outlet area of the rotor are taken from the shaft to the tip of the blades in order to account for the pressure difference acting on the rotor disc.

$$F_{axial,pressure} = p_{rotor,in} \cdot A_{inlet} + \frac{p_{rotor,out} + p_{rotor,in}}{2} \cdot (A_{outlet} - A_{inlet}) - p_{rotor,out} \cdot A_{outlet} \pm (p_{shaft} - p_{atm}) \cdot A_{shaft} \tag{4.1}$$

For a radial inflow turbine, the force due to the pressure difference can be calculated using Equation 4.2, which holds for a design with the shaft at the low pressure side of the turbine. Figure 4.3 presents a sketch of the geometry of a radial inflow turbine to clarify this relation. The shaft is located at the side with the lower pressure, which provides more benign conditions for the bearings and seals of the shaft. A guide to thrust bearing load-carrying capability presented by Neale [75] is used as can be seen in Figure 4.2. As a first approximation, according to Figure 4.2 a rotational speed of 50,000rpm and a shaft diameter of 20mm would result in a maximum load of approximately 4100N when using a hydrodynamic oil film. As noted in the literature review in Chapter 2, keeping the shaft diameter small is also beneficial for the bearing design as this keeps the surface speeds low. As an initial estimation during the preliminary design, the shaft of the radial inflow turbine is assumed to be as large as the rotor exit hub diameter, with a maximum of 20mm. Based on the axial force estimations of the preliminary design, it will be reviewed whether the axial force does not exceed the maximum load capability. The curved part of the rotor as seen in Figure 4.3 is assumed to experience a pressure which is the average of the inlet and outlet pressure.

$$F_{axial,pressure} = p_{rotor,in} \cdot \frac{\pi \cdot D_{inlet}^2}{4} - \frac{p_{rotor,out} + p_{rotor,in}}{2} \cdot \left(\frac{\pi \cdot D_{inlet}^2}{4} - A_{outlet} - A_{shaft} \right) - p_{rotor,out} \cdot A_{outlet} - p_{atm} \cdot A_{shaft} \tag{4.2}$$

A similar approach is used for the evaluation of the radial outflow turbine and can be seen in Equation 4.3. At the back side of the rotor, a pressure force is assumed to be acting equal to the outlet pressure of the turbine. Similar as to the radial inflow turbine, the shaft at the back side of the rotor is assumed to be 20mm in diameter and to have an atmospheric back pressure. Note that the factor 2 is present since only half of the turbine is considered as can be derived from Figure 4.4.

$$\begin{aligned} F_{axial,pressure} = 2 \cdot (&p_{rotor,in} \cdot A_1 + \left(\frac{p_{stator,in} + p_{stator,out}}{2} \right) \cdot A_2 + p_{stator,out} \cdot A_3 \\ &+ \left(\frac{p_{stator,out} + p_{rotor,out}}{2} \right) \cdot A_4 - p_{rotor,out} \cdot A_5 - p_{atm} \cdot A_{shaft}) \end{aligned} \tag{4.3}$$

The axial force due to the momentum difference is calculated according to Equation 4.4. For the radial inflow turbine it is assumed that the flow will enter the turbine without an axial component, so $V_{in,axial}$ is assumed to be equal to 0. Finally, the total axial force of the rotor is found by adding the loads due to pressure and momentum for each stage as seen in Equation 4.5.

$$F_{axial,momentum} = \dot{m} \cdot (V_{in,axial} - V_{out,axial}) \tag{4.4}$$

$$F_{axial} = \sum_{i=1}^{N_{stages}} (F_{axial,pressure} + F_{axial,momentum}) \tag{4.5}$$

4.3.2. INPUT PARAMETERS

To explore the design space of the turbine, several input parameters of zTurbo are varied, while taking into account the turbine operating conditions and requirements as defined in Tables 4.1 and 4.2.

AXIAL TURBINE

For evaluating the axial turbine, the Traupel loss model [38] is used because this is a widely used empirical model and has shown good results for other axial turbines in the past [76]. However, as identified in [77], because of the small flow passages and increasing compressibility, the uncertainties in the results tend to get larger. Therefore, after the design area of interest is identified by looking at the results of the iterator, the turbine geometries will be analysed using the Craig and Cox loss model [37] as well as the Soderberg loss model [36]. According to Walsh and Fletcher [7], the expansion ratio per stage in an axial turbine is usually in

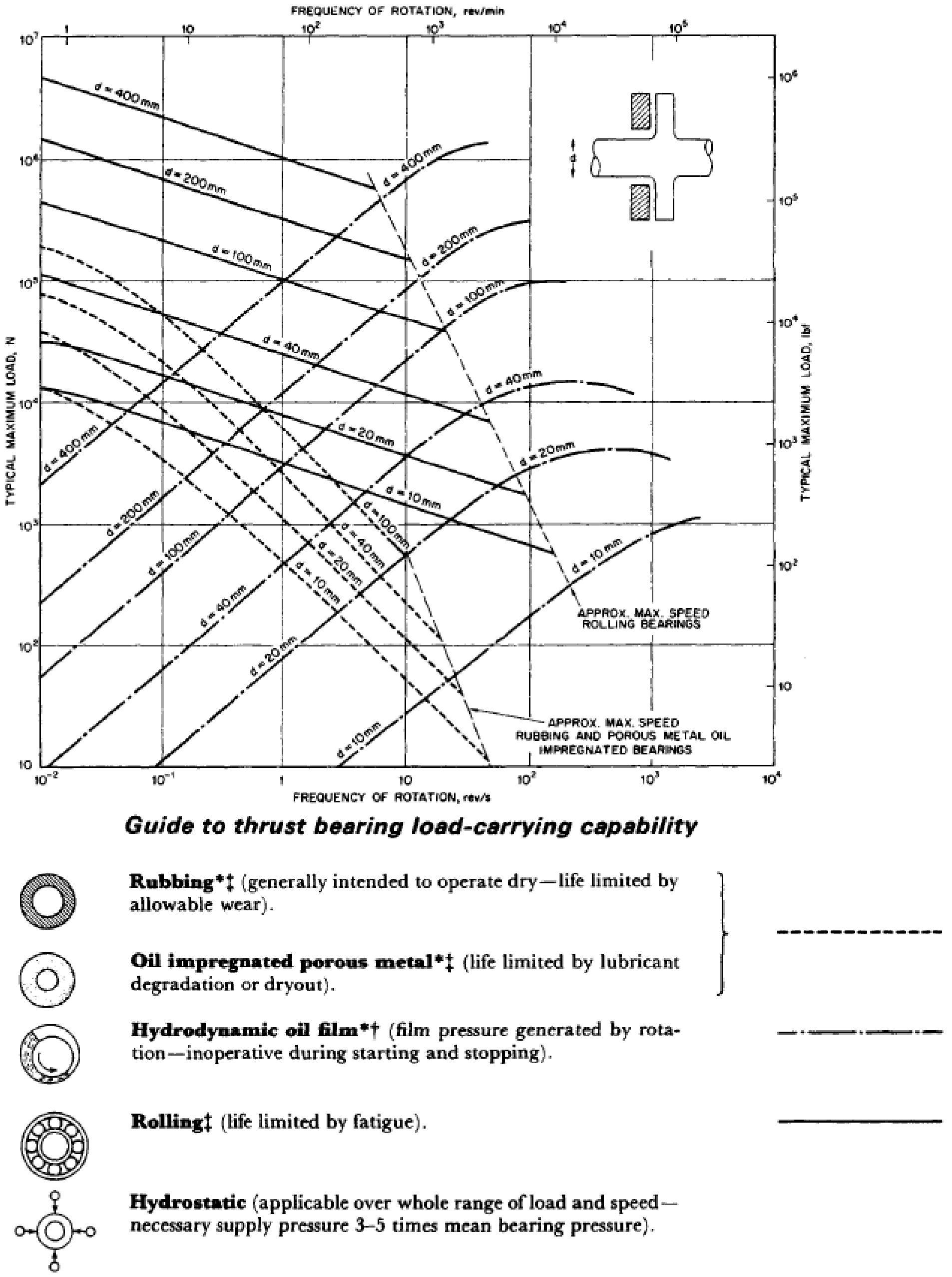

Guide to thrust bearing load-carrying capability

Rubbing*‡ (generally intended to operate dry—life limited by allowable wear).

Oil impregnated porous metal*‡ (life limited by lubricant degradation or dryout).

Hydrodynamic oil film*† (film pressure generated by rotation—inoperative during starting and stopping).

Rolling‡ (life limited by fatigue).

Hydrostatic (applicable over whole range of load and speed—necessary supply pressure 3–5 times mean bearing pressure).

Figure 4.2: Guide to thrust bearing load-carrying capability [75].

between 2 and 3. The expansion ratio is equal to 2.22, as can be calculated from the turbine characteristics summarised in Table 4.1. Therefore, only a single-stage axial turbine is considered. As a first estimation, the stator axial chord is equal to $5mm$ which is in the same order as the rotor chord. The range over which the design parameters are varied during the iteration are summarised in Table 4.5. The rotational speed is varied from the maximum allowable rotational speed to some lower rotational speeds. The stator blade height over diameter ratio is varied over a range which has the same order of magnitude as the result of [77]. Also the degree of reaction is varied from a pure impulse turbine with a degree of reaction of 0.01 to a 0.5 reaction turbine with several intermediate steps. The requirement of having a low axial force might limit the maximum degree of reaction, so therefore it is important to explore the design space of a low reaction turbine. The minimum absolute stator outflow angle is based on the minimum recommended angle as defined in [13]. A quick preliminary analysis showed that full admission turbines can meet the requirements. A full admission turbine is expected to lower the losses and to simplify the turbine design by making the turbine axisymmetric. It is therefore chosen to only consider full admission turbines for the remainder of this Section.

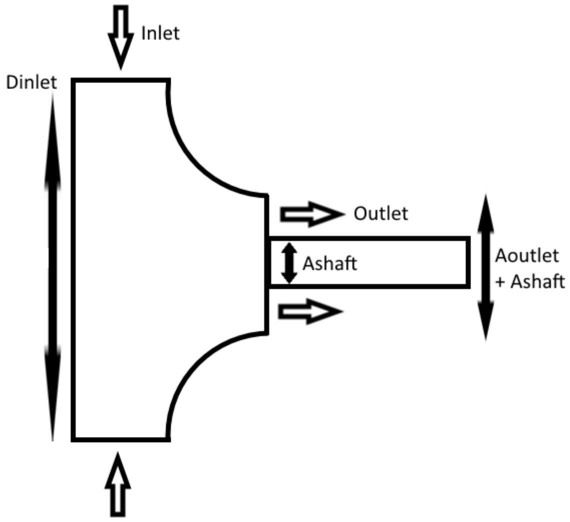

Figure 4.3: Sketch of a radial inflow turbine.

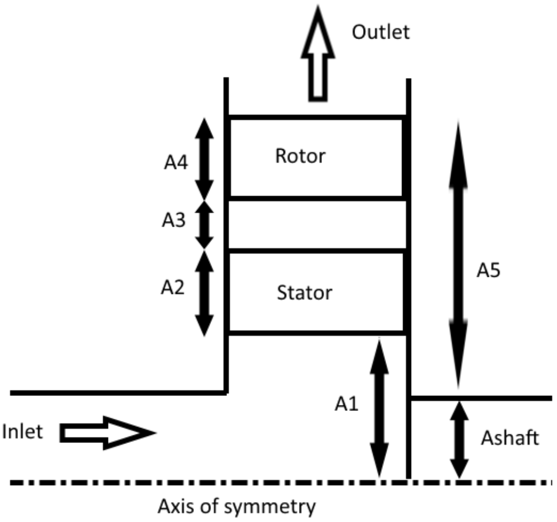

Figure 4.4: Sketch of a radial outflow turbine.

This process is repeated for a mass flow rate of $2.5kg/s$, $3kg/s$ and $3.5kg/s$. These values are chosen based on some test runs which showed that a mass flow rate of just over $3kg/s$ would be required to get a net power output of $300kW$, which was set as the maximum power output of the turbine in Section 4.1. Also evaluating a mass flow rate of $2.5kg/s$ is done to see the effect of changing the mass flow rate on the turbine performance, where a turbine with a higher mass flow rate is expected to have larger dimensions, thereby allowing for a more benign turbine design.

Table 4.5: Axial turbine iterator parameters.

Parameter	Minimum value	Maximum value	Step
Rotational speed [rpm]	40,000	50,000	2,500
Stator inlet blade height [m]	0.001	0.009	0.001
Stator blade height over diameter ratio [-]	0.01	0.11	0.01
Stage degree of reaction [-]	0.01	0.51	0.1
Stator absolute outflow angle [°]	71	86	3
Rotor axial chord [m]	0.005	0.010	0.0025
Rotor relative outflow angle [°]	69	85	4

Radial inflow turbine

Also for the Radial Inflow Turbine (RIT) the Traupel loss model [38] is used, the same as used in the mini-ORC turbine evaluation in [77]. It is decided to not use the Glassman loss model [39] or the Baines loss model [40] during the design space exploration, because when using these loss models, zTurbo often fails to estimate the turbine performance as already mentioned in Section 4.2. Without manually interrupting the zTurbo analysis, the Glassman loss model can therefore not be used in the design space exploration. The Glassman loss model will be used as a second loss model to re-evaluate the results. As a first estimation, the stator axial chord is equal to $0.01m$, which is in the same order as the dimensions in [77]. The range over which the design parameters are varied during the iteration are summarised in Table 4.6. Many of the values as seen in Table 4.6 are equal to the values in Table 4.5. The maximum stator blade height over diameter ratio is reduced compared to the axial turbine architecture, since for a radial inflow turbine the rotor diameter has to be smaller than the stator diameter.

This process is repeated for a mass flow rate of $1.0kg/s$, $2.0kg/s$ and $3.0kg/s$. These values are chosen based on some test runs which showed that a mass flow rate of just below $3kg/s$ would be required to get a net power output of $300kW$. The lower values are chosen to study how the mass flow rate affects the turbine performance. This is lower than the mass flow rate of the axial turbine, as a radial inflow turbine is assumed to perform better at low mass flow rates compared to axial turbines [13].

Table 4.6: Radial inflow turbine iterator parameters.

Parameter	Minimum value	Maximum value	Step
Rotational speed $[rpm]$	40,000	50,000	5,000
Stator inlet blade height $[m]$	0.001	0.005	0.001
Stator blade height over diameter ratio [-]	0.01	0.026	0.004
Stage degree of reaction [-]	0.01	0.51	0.25
Stator absolute outflow angle [°]	68	86	3
Rotor axial chord $[m]$	0.017	0.041	0.003
Rotor relative outflow angle [°]	65	85	2
Degree of admission [-]	0.1	1.0	0.45

RADIAL OUTFLOW TURBINE

Similar to the radial inflow turbine, the Traupel loss model [38] is used for evaluating the Radial Outflow Turbine (ROT). Although the Craig and Cox loss model [37] uses an empirical relation based on axial turbine data, similar as in [77] the 20 turbine geometries having the highest performance for the $3.5 kg/s$ case are analysed again using the Craig and Cox loss model. The flow is assumed to enter the stator without an incidence angle. As a first estimation, the stator axial chord is equal to $0.01 m$. The range over which the design parameters are varied during the iteration are summarised in Table 4.7. Most of the values in Table 4.7 are equal to the values in Table 4.5 or Table 4.6.

This process is repeated for a mass flow rate of $2.5 kg/s$ and $3.5 kg/s$. The value of $3.5 kg/s$ is chosen based on some test runs, which showed that a mass flow rate of around $3.5 kg/s$ would be required to get a net power output of $300 kW$. Contrary to the axial and radial inflow turbine analyses, this time only one lower mass flow rate of $2.5 kg/s$ is evaluated to speed up the calculation process.

Table 4.7: Radial outflow turbine iterator parameters.

Parameter	Minimum value	Maximum value	Step
Rotational speed $[rpm]$	40,000	50,000	5,000
Stator inlet blade height $[m]$	0.001	0.003	0.001
Stator blade height over diameter ratio [-]	0.01	0.20	0.02
Stage degree of reaction [-]	0.01	0.51	0.25
Stator absolute outflow angle [°]	68	86	3
Rotor axial chord $[m]$	0.017	0.041	0.006
Rotor relative outflow angle [°]	65	85	4
Degree of admission [-]	0.1	1.0	0.45

4.3.3. RESULTS AND DISCUSSION

The list of feasible geometries is limited to the ones identified to give reasonable performance (above 60% total-to-static efficiency) with an axial load below $\pm 5000 N$ and flaring angles below ±30°.

AXIAL TURBINE

As explained in Section 4.3.1, the shaft can be placed at the high pressure or low pressure side of the turbine, which will have an effect on the axial force. This effect is visualised in Figures 4.5 and 4.6, which show that a high degree of reaction turbine results in high axial forces for both shaft locations. It is observed that the axial load is lower than $5000 N$ for a degree of reaction close to 0 when the shaft is placed at the low pressure side. However, the loads are still well above $3000 N$ for this case. The axial load can be reduced by placing the shaft at the high pressure side, which allows for a slightly higher degree of reaction of 0.11 while still obtaining low axial loads. Based on the results as shown in Figures 4.5 and 4.6 it is decided to only consider the axial turbine in combination with the shaft placed at the high pressure side for the remainder of this Section.

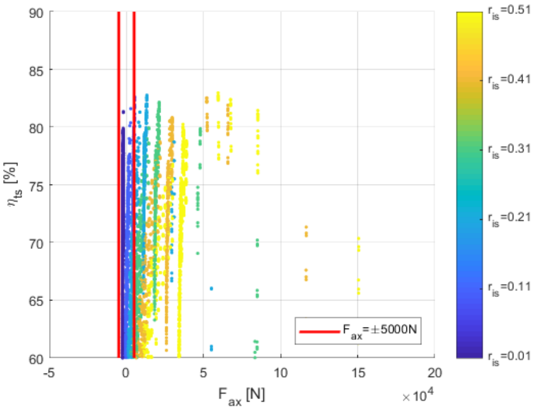

Figure 4.5: Efficiency and degree of reaction versus axial force for $\dot{m} = 3kg/s$ axial turbine with shaft at the high pressure side.

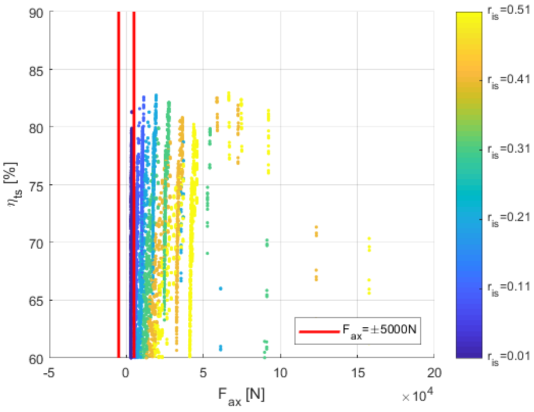

Figure 4.6: Efficiency and degree of reaction versus axial force for $\dot{m} = 3kg/s$ axial turbine with shaft at the low pressure side.

The overall results, together with the results of the other turbine architectures will be summarised in Figure 4.13. The effect of changing the parameters on the performance of an axial turbine is visualised in Appendix A.1, but can be summarised as follows. The results show that the rotational speed has no clear effect on the achievable efficiency. The stator blade height should be smaller than $5mm$ and optimal performance is achieved when the stator blade height over diameter is chosen such that the diameter is in between $8cm$ and $10cm$. Equally high efficiencies can be achieved for a degree of reaction of 0.01 and 0.11. An increasing stator outflow angle has a beneficial effect on the performance for the turbines with a mass flow rate of $2.5kg/s$ and $3kg/s$, but this effect is less pronounced for the $3.5kg/s$ mass flow rate turbine. The variation in possible performance for different rotor chords is small, although the rotor chord has an impact on the aspect ratio of the blade as will be discussed later. Similar as for the stator outflow angle, an increasing rotor outflow angle has a beneficial effect on the performance, where for the $3.5kg/s$ mass flow rate turbine an optimum in efficiency can be seen at stator outflow angles in between 81° and 85°.

Without putting any additional constraints on the feasible designs, the average output power is taken of the 30 cases having the highest total-to-static efficiency at each mass flow rate in order to investigate the effect of changing the mass flow rate on the output power. It can be observed that the output power scales approximately linearly with the mass flow rate, which is visualised in Figure 4.7, indicating that similar levels of efficiency can be obtained. This shows that if the efficiencies for the different mass flow rates as estimated by the analyses using the Traupel loss model can be achieved in reality, in order to get a power output of $300kW$, the mass flow rate should be approximately $3.2kg/s$. Based on this preliminary design, no clear trend of decreasing turbine performance for decreasing mass flow rate can be observed.

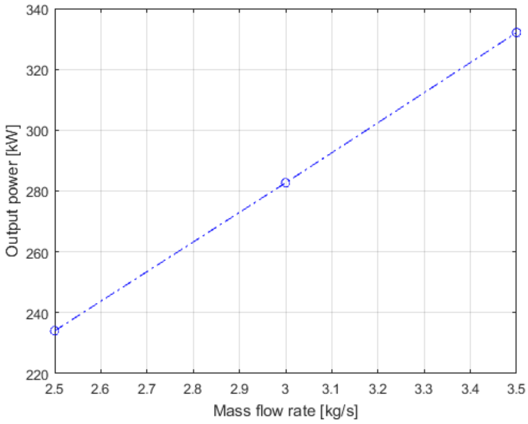

Figure 4.7: Axial turbine mass flow rate versus output power.

The 20 turbine geometries having the highest efficiency for the $3kg/s$ case are analysed again using the Craig and Cox loss model [37] as well as the Soderberg loss model [36]. The results show that the Craig and Cox loss model always overestimates the total-to-static efficiency compared to the Traupel loss model to unrealistically high values close to 100%. This makes the validity of the Craig and Cox model for small axial turbine geometries operating with sCO_2 is questionable. The results of the comparison with the Soderberg loss model are summarised in Table A.1 in Appendix A.1, but the main observation is that the Soderberg loss model estimates a higher efficiency of in between 8% and 14% compared to the Traupel loss model. As the Soderberg loss model represents just a simplistic relation between a limited number of parameters, the efficiencies as estimated by the Traupel loss model are expected to be more reliable. This shows the importance of carefully selecting the loss model for the 1D design, although a detailed CFD simulation is required to accurately predict the performance of an sCO_2 turbine.

An interesting observation from the results is that the aspect ratio of the rotor blade is low for the geometries showing high efficiency. This is illustrated in Figure 4.8. As identified by Walsh and Fletcher [7], the aspect ratio of the blade should ideally be in between 2.5 and 3.5. A possible reason for the high estimated efficiencies for low aspect ratio blades is the under-prediction of the tip leakage losses, although the low loading of the rotor blade for an impulse turbine reduces the effect of the aspect ratio on the efficiency. Reducing the degree of admission is expected to increase the blade height, which for a given rotor chord would increase the aspect ratio. As identified in the literature review in Chapter 2, the use of partial admission should be avoided if possible.

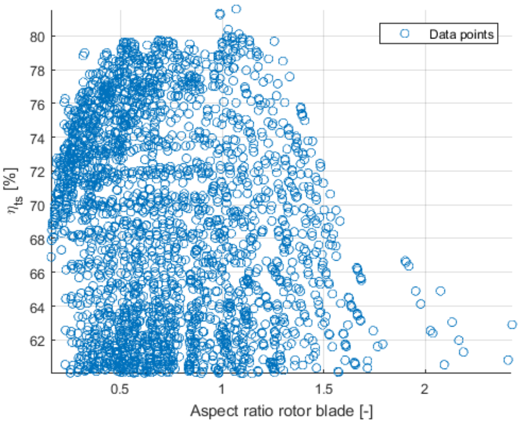

Figure 4.8: Aspect ratio of the rotor blade versus total-to-static efficiency for $\dot{m} = 3 kg/s$.

RADIAL INFLOW TURBINE

The overall results, together with the results of the other turbine architectures will be summarised in Figure 4.13. The effect of changing the parameters on the performance of a radial inflow turbine is visualised in Appendix A.2, but can be summarised as follows. The results show that the rotational speed has no clear effect on the achievable efficiency. The stator blade height should be equal to $2mm$ or $3mm$ and optimal performance is achieved when the stator blade height over diameter is in between 0.018 and 0.026. As can be seen in Figure 4.9, increasing the degree to values larger than 0.01 results in a quick increase in axial load. An increasing stator outflow angle has a beneficial effect on the performance for the turbines with a mass flow rate of $3kg/s$, but this effect is less pronounced for the lower mass flow rate turbines. For the radial turbine, the rotor chord is defined as the absolute distance between the mean line rotor inlet and rotor outlet. Increasing the rotor chord leads to additional profile losses, which explains the limited number of feasible solutions found at high rotor chords. Whereas the turbine performance seems to be independent from the relative rotor outflow angle for the $2kg/s$ and $3kg/s$ mass flow rate turbines up to 81°, a reduction in performance is seen when increasing this angle above 77° for the $1kg/s$ turbine.

It should be noted that also lower degree of admission designs are included the results. However, it is found that the effect of blade blockage as a result of reducing the degree of admission on the turbine efficiency is not accurately modelled in zTurbo. Full admission designs are found to show high efficiencies. Therefore, only full admission turbines are considered for the remainder of this Section.

Without putting any additional constraints on the feasible designs, the average output power is taken of the 30 cases having the highest total-to-static efficiency at each mass flow rate, in order to investigate the effect of changing the mass flow rate on the output power. It can be observed that the estimated achievable output power scales almost linearly with the mass flow rate, which is visualised in Figure 4.10, indicating that similar efficiencies can be obtained for the different mass flow rates. This shows that if the efficiencies as estimated by the analyses using the Traupel loss model can be achieved in reality, in order to get a power output of $300kW$, the mass flow rate should be approximately $3kg/s$.

Combinations of geometry and operating conditions giving the highest total-to-static efficiency for the $3kg/s$ mass flow case, while meeting the aforementioned conditions by using the Traupel loss model, are

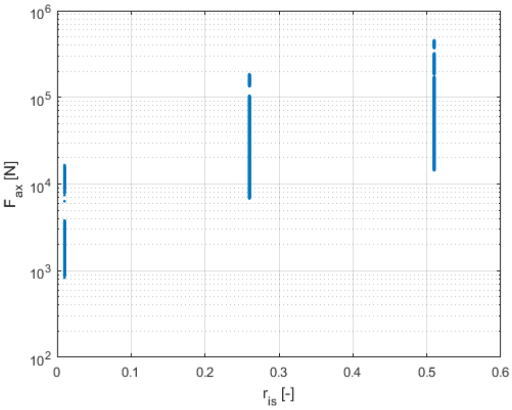

Figure 4.9: Radial inflow turbine degree of reaction versus axial load for $\dot{m}=3kg/s$.

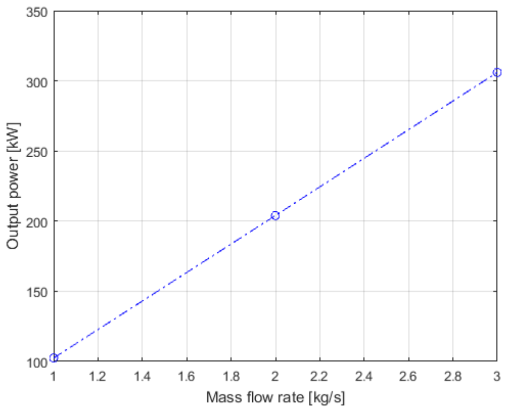

Figure 4.10: Radial inflow turbine mass flow rate versus output power.

analysed again using the Glassman loss model [39] until 50 combinations are evaluated successfully. The Glassman loss model is based on flow physics as well as experimental data on radial inflow turbines. As explained before, the reason the Traupel loss model was chosen for the first round of analyses is because in zTurbo the Glassman loss model does not converge for all input values and, without interrupting the calculation manually, the computational time would go to infinity. Therefore, the Glassman loss model cannot be used in an iterator or optimiser for exploring a large design space. The reason the Baines loss model [40], which is also based on radial inflow turbines, is not used is because in zTurbo the Baines loss model in most cases fails to give an output for a given turbine design, whereas the Glassman loss model can give a result. The results of this comparison are summarised in Table A.2 in Appendix A.2, but the main observation is that the Glassman loss model predicts a higher total-to-static efficiency compared to the analyses using the Traupel loss model. This difference is in between 8% and 14% for all cases analysed, with an average difference of 10.6% and a standard deviation of 1.3%. The difference in estimated efficiency is likely to be due to the tip clearance loss which turns out to be not taken into account for the Glassman loss model in zTurbo. This can result in an efficiency reduction of around 10% for small turbine designs [13].

RADIAL OUTFLOW TURBINE

Even with the large design space as explained before, only a limited number of turbine geometries (approximately 150) are identified to give reasonable performance (above 60% total-to-static efficiency) with an axial load below $\pm 5000N$ and flaring angles below $\pm 30°$. The reason for this is that for a radial outflow turbine, the area near the inlet is subjected to the high pressure flow. This can induce a large axial load, even for a low degree of reaction.

The overall results, together with the results of the other turbine architectures will be summarised in Figure 4.13. The degree of admission versus the estimated efficiencies of the $2.5kg/s$ and $3.5kg/s$ mass flow rate radial outflow turbines can be seen in Figures 4.11 and 4.12 respectively. The first observation is that the estimated efficiencies are inferior to the efficiencies as found for the axial and radial inflow turbine as seen before. Secondly, feasible solutions are only found at reduced degrees of admission as a result of the low mass flow rate. Whereas all feasible solutions have a degree of admission of 0.1 for the $2.5kg/s$ mass flow rate turbine, for the $3.5kg/s$ turbine solutions are found at a degree of admission of 0.1 and 0.55. This shows that increasing the mass flow might be a solution to be able to use a full admission radial outflow turbine. However, as already mentioned before, zTurbo is not capable of taking the losses due to blade blockage into account. Therefore these partial admission results are not expected to give a realistic view of the effect of the degree of admission and therefore make the validity of the estimated efficiencies questionable. Based on this, the radial outflow turbine is not considered a suitable turbine architecture for small-scale sCO_2 power cycles.

TURBINE ARCHITECTURE SELECTION

The total-to-static efficiency versus the output power of all turbine architectures and mass flow rates that are analysed is shown in Figure 4.13. For clarity, the different data sets have been numbered and these numbers are shown in Figure 4.13. As the total-to-static efficiency and the output power are linearly related, for a given

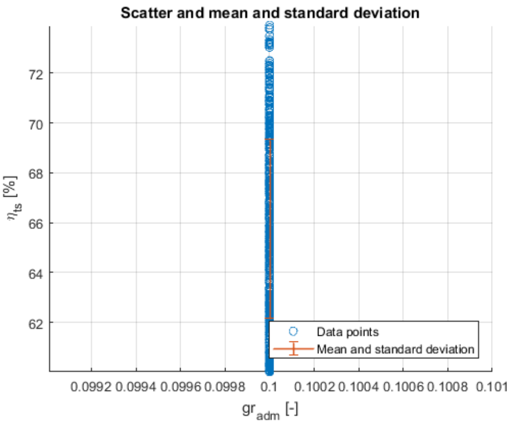

Figure 4.11: Radial outflow turbine degree of admission versus efficiency for $\dot{m}$=2.5kg/s.

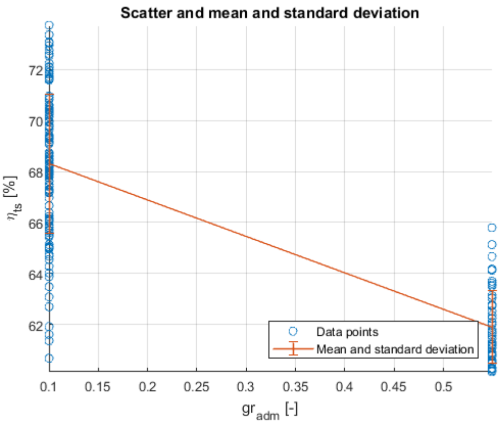

Figure 4.12: Radial outflow turbine degree of admission versus efficiency for $\dot{m}$=3.5kg/s.

mass flow rate the data points are located on a single line, regardless of the turbine architecture. From Figure 4.13 it becomes evident that the radial outflow turbine is inferior to both the axial turbine and the radial inflow turbine in terms of efficiency. It also becomes clear that the radial inflow turbine is able to achieve higher efficiencies compared to the axial turbine for the same mass flow rate. It should be noted that the results of the radial inflow turbine with a mass flow rate of 3kg/s are from the analysis using the Glassman loss model.

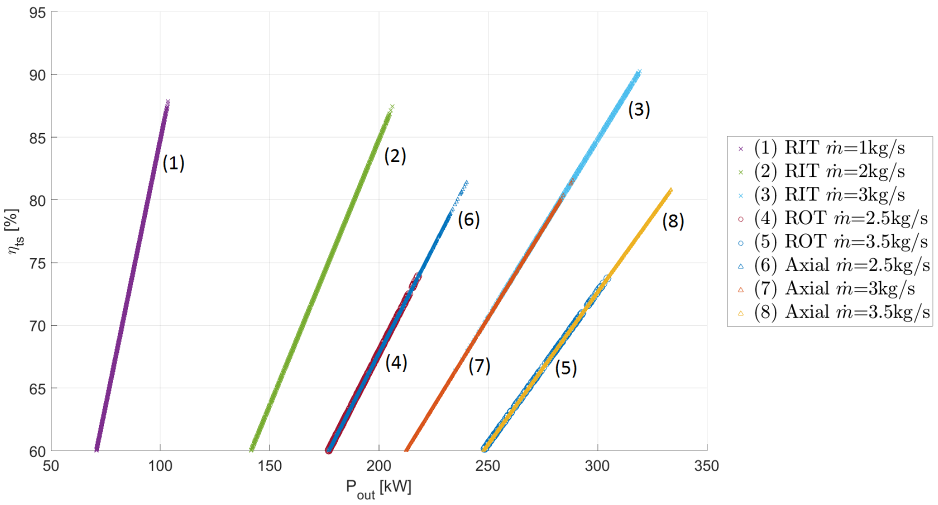

Figure 4.13: Efficiency versus output power for the analysed turbine architectures with different mass flow rates.

As explained before, the axial turbine requires the shaft to be placed at the high pressure side of the turbine to have an acceptable axial load. Full admission is possible and a low degree of reaction is desirable. However, the low aspect ratios of the full admission turbine designs are expected to result in larger losses than predicted by this preliminary design. Moreover, by removing the rotor outflow swirl, the rotor exit blade height reduces to values as low as 1mm to 2mm, resulting in a converging rotor. By using partial admission turbines, this aspect ratio can be increased. Because of the unsymmetrical design of a partial admission turbine, the design becomes more complicated and additional losses are expected. Moreover, for the high aspect ratio partial admission turbines, high stator and rotor angles are required to achieve good efficiencies.

The radial inflow turbine shows good efficiencies for full admission turbines. A degree of reaction of 0.01 is necessary for meeting axial load requirements. It should be noted that during the preliminary turbine design of the radial inflow turbine, the shaft is assumed to be placed at the low pressure side of the turbine to simplify seal and bearing design. Moving the shaft to the high pressure side of the turbine would allow the degree of reaction to increase in order to balance the axial load.

Based on these observations, it is decided to select a radial inflow turbine for the ASTRI test loop and this turbine will be analysed in more detail. An additional benefit of using a radial inflow turbine is that the supply chain of manufacturing this turbine architecture is ready to use at the University of Queensland.

DESIGN SPACE REFINEMENT

The design space of the radial inflow turbine with a mass flow rate of $3 kg/s$ is analysed in more detail in order to decide on the mean line turbine geometry. Based on the results as discussed before, the degree of reaction is 0.01 in order to have an acceptable axial load. Only full admission turbines will be considered for this design space refinement. The range over which the parameters are varied is summarised in Table 4.8. Similar to before, first the Traupel loss model [38] will be used, followed by a re-evaluation of the turbine concepts with the Glassman loss model [39].

Table 4.8: Radial inflow turbine refinement iterator parameters.

Parameter	Minimum value	Maximum value	Step
Rotational speed $[rpm]$	45,000	50,000	5,000
Stator inlet blade height $[m]$	0.001	0.004	0.001
Stator blade height over diameter ratio [-]	0.018	0.026	0.002
Stator absolute outflow angle [°]	65	86	3
Rotor inlet-to-outlet diameter ratio [-]	1.2	2.6	0.2
Rotor relative outflow angle [°]	65	85	3

The results of this analysis using both the Traupel and the Glassman loss model is visualised in Appendix A.3, but can be summarised as follows. The main observation is that estimated efficiency of the Glassman loss model is higher than the Traupel loss model. This is because the rotor tip clearance having no effect on the estimated efficiency for the Glassman loss model. As a result, the Glassman loss model predicts an optimal efficiency at a large rotor outlet diameter, as the tip clearance effects of the corresponding small blade heights are neglected. The Traupel loss model suggests the rotor inlet-to-outlet diameter ratio should be in between 1.6 and 2.2.

The effect of varying the tip clearance on the performance is investigated by running the geometries using the Traupel loss model with a rotor tip clearance of 1% and 4.5% of the blade height. A tip clearance of 4.5% is in the same order as the radial clearance in the design of Qi et al. [13]. The most noticeable effect is observed for the stator outflow angle, rotor outlet diameter and rotor inlet-to-outlet diameter ratio, where the latter two are related to each other. This effect is shown in Figures 4.14 and 4.15, where the colour bars represent the stator outflow angle in degrees. From Figures 4.14 and 4.15 it can be observed that for larger rotor outlet diameters, which lead to a lower rotor inlet-to-outlet diameter ratio, the effect of varying the rotor tip clearance has a stronger effect on the performance as the outlet blade height decreases. Also it can be seen that the effect on the performance when varying the tip clearance is stronger for higher stator outflow angles, as indicated by the colours in Figures 4.14 and 4.15. Even though the Glassman loss model suggests a low rotor inlet-to-outlet diameter ratio is beneficial for the performance, a higher rotor inlet-to-outlet diameter might be favourable to reduce the effect of the rotor tip clearance. Similarly, this shows that a lower stator outflow angle decreases the effect of the rotor tip clearance on the turbine efficiency.

The effect on the turbine efficiency by increasing the specific speed close to 0.6 as suggested by Walsh and Fletcher [7] is evaluated. For given cycle operating conditions and a given turbine power output, which defines the mass flow rate, the only way to change the specific speed is by changing the rotational speed [7]. An analysis is done to evaluate the effect of ignoring the maximum rotational speed of $50 krpm$ and to increase it to $100 krpm$. For this analysis, several zTurbo input parameters are varied over a selective range as seen in Table 4.9, which is based on the range over which the parameters are varied for the previous analysis. The results of the previous radial inflow turbine calculations with a mass flow rate of $3 kg/s$, as well as the results of the analysis with the increased rotational speed, can be seen in Figure 4.16. The Glassman loss model is used for all of these analyses. First of all, it can be observed that for all rotational speeds the estimated total-to-total efficiency is higher than the line of maximum achievable efficiency as estimated by Walsh and Fletcher [7]. A

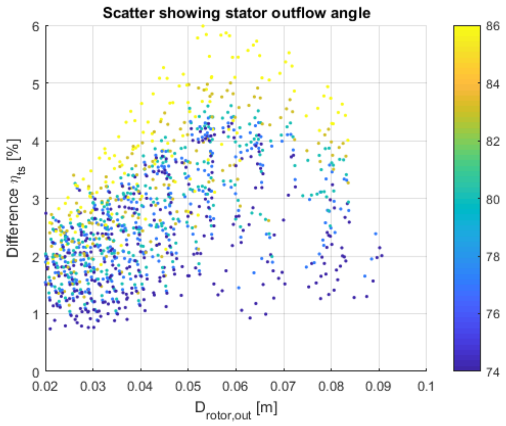

Figure 4.14: Reduction in estimated total-to-static efficiency by changing the rotor tip clearance from 1% to 4.5% for various rotor outlet diameters and stator outflow angles.

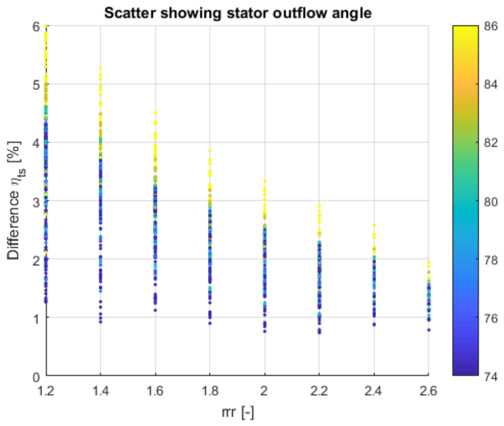

Figure 4.15: Reduction in estimated total-to-static efficiency by changing the rotor tip clearance from 1% to 4.5% for various rotor inlet-to-outlet diameter ratios and stator outflow angles.

possible reason for this is the tip clearance effect, which is neglected in the Glassman loss model. Secondly, it can be observed that the estimated efficiency is increased by changing the rotational speed to $100krpm$. Based on these observations on the preliminary design results, in can be concluded that the turbine efficiency can be improved by increasing the turbine output power, which effectively results in a larger mass flow rate, or by increasing the rotational speed. For the relatively low output power turbine with a limited rotational speed, the specific speed is limited to the lower side of the suggested range as explained above. As there is no validation data for sCO_2 turbines available yet, it is not possible to validate these results. By doing CFD simulations it can be checked whether these estimations are realistic.

Table 4.9: Radial inflow turbine $100krpm$ iterator parameters.

Parameter	Minimum value	Maximum value	Step
Stator inlet blade height [m]	0.001	0.004	0.001
Stator blade height over diameter ratio [-]	0.018	0.026	0.002
Stator absolute outflow angle [°]	65	71	3
Rotor inlet-to-outlet diameter ratio [-]	1.2	2.6	0.2
Rotor relative outflow angle [°]	65	68	3

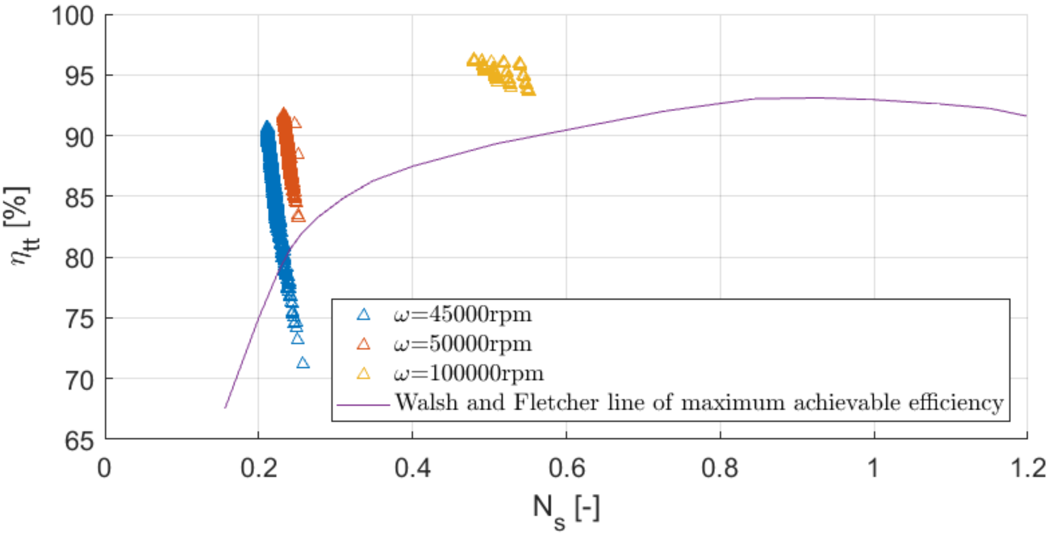

Figure 4.16: Calculated efficiency versus specific speed and Walsh & Fletcher line of maximum efficiency [7].

4.4. PRELIMINARY TURBINE CONCEPT

Based on the results of the refinement and considerations as explained above, it is decided to choose the turbine concept giving the highest efficiency as predicted by the Glassman loss model with a rotor inlet-to-outlet diameter ratio of in between 1.6 and 2.2. This turbine has a rotor inlet-to-outlet diameter ratio of 1.8 in combination with a stator outflow angle of 70°, which is expected to have a good efficiency and axial load. Investigation of the results shows that the relative outflow angle has to be reduced to a value as low as 60° in order to have a nearly axial outflow. The characteristics of the chosen turbine concept are summarised in Table 4.10.

The values as seen in Table 4.10 are taken from the zTurbo output file where some of the values, like the degree of reaction or the stator absolute outflow angle, differ slightly from the input value. Note that these results have been obtained by analysing the concept using the Glassman loss model. The specific speed is calculated using the expression given by Walsh and Fletcher [7] as presented in Section 2.1. The specific speed is on the lower side of the range of 0.2 to 0.6 as suggested by Japikse and Baines [73] for a radial inflow turbine. The velocity ratio, calculated using the blade speed at the rotor inlet and the spouting velocity by using the enthalpy drop across the turbine, is equal to 0.52. This is below the suggested value of 0.7 as given by Dixon [78]. Based on this, it would be beneficial to increase the rotational speed above the specified limit. One of the noticeable features is the decelerating flow in the rotor, as can be seen by the rotor inlet-to-outlet relative velocity ratio in Table 4.10. This is a result of the low degree of reaction. It should be noted that the number of stator and rotor blades as shown in Table 4.10 will be re-evaluated in the 3D design. The resulting meridional section and the velocity triangles at the rotor inlet and outlet can be seen in Figures 4.17 and 4.18. These results of the preliminary design can be used as a starting point for the 3D aerodynamic design as explained in the overall methodology in Chapter 3.

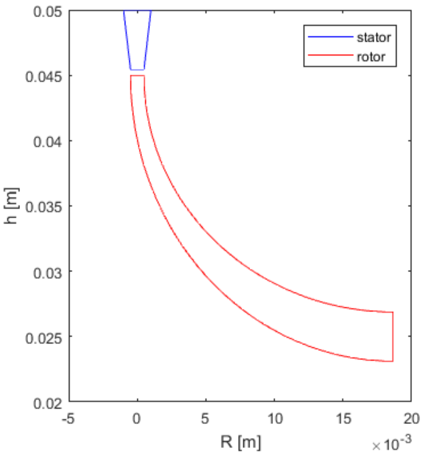

Figure 4.17: Meridional section of the selected turbine.

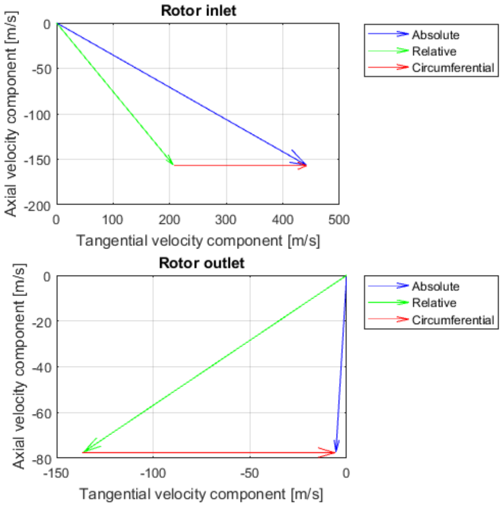

Figure 4.18: Velocity triangles at the rotor inlet and outlet of the selected turbine.

Table 4.10: Selected turbine characteristics.

Parameter	Value
Turbine architecture	Radial inflow - Axial outflow
Mass flow rate $[kg/s]$	3
Degree of admission [-]	1
Degree of reaction [-]	-0.02
Rotational speed $[rpm]$	50,000
Specific speed [-]	0.233
Stator absolute outflow angle [°]	70
Stator inlet blade height $[m]$	0.002
Stator outlet blade height $[m]$	0.001
Stator blade height over diameter ratio [-]	0.02
Stator inlet diameter $[m]$	0.100
Stator outlet diameter $[m]$	0.091
Stator expansion ratio [-]	2.19
Number of stator blades [-]	51
Rotor relative inflow angle [°]	51
Rotor relative outflow angle [°]	58
Rotor absolute outflow angle [°]	-3
Rotor inlet blade height $[m]$	0.0009
Rotor outlet blade height $[m]$	0.0034
Rotor inlet diameter $[m]$	0.090
Rotor mean outlet diameter $[m]$	0.050
Rotor inlet-to-outlet relative velocity ratio [-]	1.64
Rotor expansion ratio [-]	1.01
Number of rotor blades [-]	11
Stator outlet absolute Mach number [-]	1.14
Turbine outlet absolute Mach number [-]	0.21
Axial load $[N]$	2878
Total-to-static efficiency Traupel [%]	81.0
Total-to-static efficiency Glassman [%]	88.6
Output power Traupel $[kW]$	287
Output power Glassman $[kW]$	313

5

AERODYNAMIC AND MECHANICAL DESIGN PROCEDURE

In this Chapter, the procedure for the aerodynamic design and mechanical stress evaluation will be elaborated upon as part of the overall turbine design process as presented in Chapter 3. First, in Section 5.1 the procedure for the generation of the turbine geometry and grid for both the aerodynamic design and the mechanical stress evaluation will be explained. This is followed by the procedure to evaluate the aerodynamic and mechanical performance of the turbine in Section 5.2.

5.1. BLADE DESIGN AND MESH GENERATION PROCEDURE

Before an aerodynamic or mechanical design can be done, the geometry and corresponding mesh have to be created, which model for an aerodynamic design the fluid domain and for a mechanical design the blade and hub profile. Creating this geometry and corresponding mesh in a parametric way based on an input script allows for a quick 3D model setup, where any future changes can be made relatively easily.

The aerodynamic mesh is created based on the method as described by Jahn [41]. The turbine meshing tool of Jahn can create a structured mesh for both the stator and rotor based on several parametric input values and accounts for the tip clearance at the rotor. In alternative methods, the 3D shape is often based on parameters describing the blade and hub contour rather than parameters describing the fluid path. The main difference between the approach used in this thesis and alternative methods is that parametric input values directly define the aerodynamic properties of the passage, in particular for the rotor. In this way, the aerodynamic shape is an input instead of an output of the geometry creation tool.

When using converging nozzles with choked conditions, the flow continues to expand after the stator trailing edge because of the additional space, causing the flow to over-accelerate as argued by Jahn [41]. In a converging stator the expansion and compression waves interact, causing a non-uniform flow field downstream of the stator. Persico and Pini [23] argue that a purely converging stator shape would result in only weak shock waves while simplifying blade design. Using a convergent-divergent stator design where the flow is choked at the throat, which is located slightly upstream of the stator exit, allows for controlling the mass flow rate and expansion process in the turbine directly. By shaping the stator walls in the supersonic region, a uniform outflow can be achieved at the rotor inlet. As achieving the highest turbine efficiency is not the main aim of this thesis, the benefit of controlling the sonic expansion makes a convergent-divergent stator the preferred type.

In the mesh generation method of Jahn, the stator geometry is described by several parameters, which for a transonic turbine design ensure the Mach number at the trailing edge is as desired. These parameters are the blade height, stator outlet angle, the radial position of the leading edge, trailing edge and throat, as well as the radius describing the curvature of the leading edge and the throat. Given the desired mass flow rate, turbine inlet conditions and gas properties, the required throat area to ensure sonic conditions are reached in the throat is calculated by solving Equation 5.1 for Mach 1. The required throat width can be calculated

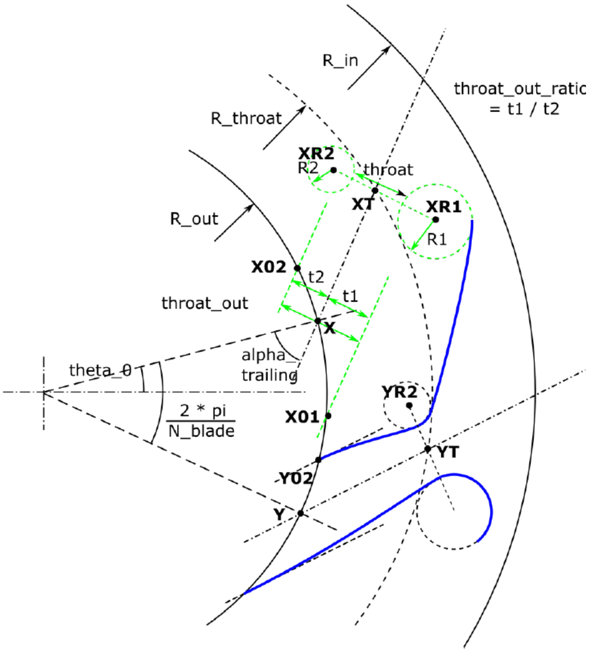

Figure 5.1: Generating a convergent-divergent stator based on parametric input values [41].

by dividing the throat area by the stator blade height and the number of blades. For solving Equation 5.1, the design mass flow rate is taken from the selected turbine design of the preliminary design as presented in Table 4.10. The total pressure and temperature of the incoming flow are used as imposed by the turbine requirements in Table 4.1. The values of 1.238 and 189 are used for γ and R respectively, which are average quantities between the turbine inlet and turbine outlet estimated by the preliminary design as described in Chapter 4, which is linked to the Refprop database [34]. A schematic of the parameters defining the stator passage shape can be seen in Figure 5.1. In the same way, the required throat width at the stator outlet to ensure the Mach number is as desired is calculated by solving Equation 5.1, using the stator outlet Mach number of 1.14 of the selected turbine design of the preliminary design as can be seen in Table 4.10.

$$A_{passage} = \frac{\dot{m}}{\frac{p_0}{\sqrt{T_0}} \cdot M \cdot \sqrt{\frac{\gamma}{R}} \cdot \left(1 + \frac{\gamma - 1}{2} \cdot M^2\right)^{\frac{-(\gamma+1)}{2\cdot(\gamma-1)}}} \tag{5.1}$$

In the current tool, the stator mesh is created with the blade in the centre of the mesh and the fluid domain is split in half. The tool is modified such that the user has the possibility to create the stator mesh with the channel in the centre instead of the stator blade in the centre. This is done in order be able to make slices along the channel to evaluate the one-dimensionalised properties as will be explained later.

After the stator geometry is defined, a structured mesh is created based on a number of user input values. By changing these values, the user is able to tune the mesh in a relatively simple way. The tool described in [41] allows for changing the number of cells in each mesh block, the shape of the blocks and the cluster functions. As also these options can be tuned by simply changing the corresponding parameters in the user input file, the user is able to quickly generate and change a mesh.

As mentioned before, whereas traditionally the rotor of a radial turbine is based on parameters from a mechanical point, the approach of shaping the rotor in this work is based on an aerodynamic point of view [41]. This means that rather than defining the shape based on parameters describing the hub, shroud and blade angle, the shape is based on aerodynamic parameters such as the flow area, wetted area and flow direction. The twist angle is found in an iterative way to ensure a smooth profile in which the streamline experiences a continuous change in properties along the channel. The steps that are taken to create the rotor geometry based on the user defined parametric input values can be summarised as follows:

- The shape of the meridional streamline consists of three sections. Based on the rotor inlet blade angle, the rotor meridional streamline starts as a straight line of a user defined length. Based on the rotor outlet blade angle, the final part of the rotor channel is a spiral with a user defined length, growth rate in the radial direction and growth rate in the axial direction. In between the straight section at the start of the rotor channel and the spiral at the end of the rotor channel, a Bezier curve is used to define the meridional streamline path. To ensure a smooth gradient between the Bezier curve and the other curves, control points close to both ends based on the gradients of the other curves are added before constructing the Bezier curve.

- The flow normal area is defined by a Bezier curve as well, which is based on a specified inflow and outflow area. The inflow and outflow area are derived from the rotor inlet and outlet diameter, blade heights and blade angles as suggested by the preliminary design.

- The effective flow area A_{eff} is calculated using the streamline as constructed in the first step and its relative projection on the normal flow area. This projection can be calculated using the local streamline directional vector $\overrightarrow{S}$ and its projection on the local $r-\theta$ plane $\overrightarrow{S}_{r\theta}$. The vector normal to the $r-\theta$ plane $n_{r\theta}$ is used, which is the cross product of the radial vector and the unit vector in the z-direction. This is summarised in Equation 5.2. Also an area correction is used for the blade thickness. This blade thickness is defined by a 1D polynomial for both the root and tip of the blade.

$$A_{eff} = \frac{A_n}{cos(\theta_{eff})} = \frac{A_n}{\overrightarrow{S} \cdot \overrightarrow{S}_{r\theta}} = \frac{A_n}{\overrightarrow{S} \cdot (\overrightarrow{S} - |\overrightarrow{S} \cdot n_{r\theta}| n_{r\theta})} \tag{5.2}$$

- The rotor hub and blade shapes are defined using the parametric passage shape. This parametric passage shape starts from a rectangular segment at the rotor inlet to an annular segment at the rotor outlet.

- The shroud shape is defined by a clearance from the rotor blade, which can be defined as a function in order to vary the absolute tip clearance along the rotor channel. Similar as in the work of Qi et al. [13], the tip clearance is limited to $0.1mm$ because of manufacturing tolerances and uncertainties in thermal expansion during operation. This is approximately 11% of the rotor inlet blade height of $0.9mm$, which adds up with the tip clearance to the stator outlet blade height of $1mm$ as presented in Table 4.10.

To be able to model rotor blades with a non-zero inlet blade angle, the method of meshing the region near the rotor leading edge is modified. The boundary layer mesh near the leading edge of the blade is extended and curved based on the gradient of the boundary layer at this location, indicated by Boundary Layer Points $BLP1$ and $BLP2$. As the line separating Block1 and Block2 as seen in Figure 5.2 is represented by an arc, the coordinates of Separation Point $SP1$ and $SP2$ are found iteratively to ensure they are located at the same radius in the polar coordinate system. This modification extends the capability of the tool to be able to model rotor blades with a non-zero blade angle at the inlet.

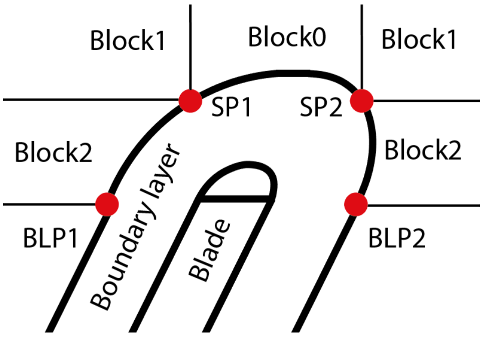

Figure 5.2: Blocks at the rotor leading edge.

As the trailing edge of a radial inflow rotor has a non-zero blade angle, a similar approach is used for the mesh near the trailing edge to add a rounded section to the blade and to create the mesh. Finally, outlet blocks are added to the meshing tool, which are defined by a helix based on the rotor mesh. This helix extends the mesh with rotor outlet blocks of a user defined length.

For the Generation 2 turbine as introduced in Chapter 3, the stator geometrical dimensions are calculated using the meanline rotor characteristics based on the TOPGEN results as will be explained in Chapter 6. To deliver to flow at the right conditions at the rotor inlet, the stator dimensions of the Generation 2 turbine are calculated based on the desired mass flow rate and the rotor inlet dimensions. First, the radial velocity at the rotor inlet $V_{radial,rotor}$ is calculated based on the continuity Equation, taking into account the tip clearance and the blade thickness as can be seen in Equation 5.3.

$$\frac{\dot{m}}{N_{rotor}} = \rho_{rotor,in} \cdot \left(\left(\frac{2\pi \cdot R_{rotor,in}}{N_{rotor}} - t_{rotor}\right) \cdot (h_{rotor} + h_{tcl,rotor,in}) + t_{rotor} \cdot h_{tcl,rotor,in}\right) \cdot V_{radial,rotor} \tag{5.3}$$

The following assumptions and constraints are made to calculate the required stator dimensions:

- The flow is isentropic in the stator.
- The density at the stator outlet is equal to the density at the rotor inlet.
- The radial velocity component at the stator outlet is equal to the radial velocity component at the rotor inlet, which is a direct conclusion from the continuity Equation.
- The number of stator blades is equal to the number of rotor blades. This is currently a constraint due to limitations in the Eilmer4 sliding interface calculation method as the corner points of the stator and rotor mesh at the sliding interface should match.
- The height of the stator is equal to the height of the rotor blade plus the tip clearance at the rotor inlet. Also this is because the corner points of the stator and rotor mesh at the sliding interface should match for the Eilmer4 simulation.
- The radius of the stator outlet is equal to the radius at the rotor inlet multiplied by a radius ratio.
- The total temperature at the stator outlet is equal to the total temperature at the rotor inlet. This means losses in the spacing between the stator outlet and rotor inlet are neglected.

Given the stator outlet blade height, the stator trailing edge blade thickness t_{stator} can be calculated to satisfy the continuity Equation using the radial velocity as seen in Equation 5.4. In the same way the tangential spacing between the stator blades b can be calculated as seen in Equation 5.5.

$$\begin{aligned} \rho_{rotor,in} \cdot \left(\left(\frac{2\pi \cdot R_{rotor,in}}{N_{rotor}} - t_{rotor}\right) \cdot (h_{rotor} + h_{tcl,rotor,in}) + t_{rotor} \cdot h_{tcl,rotor,in}\right) \cdot V_{radial,rotor} \\ = \rho_{stator,out} \cdot \left(\left(\frac{2\pi \cdot R_{stator,out}}{N_{stator}} - t_{stator}\right) \cdot h_{stator}\right) \cdot V_{radial,stator} \end{aligned} \tag{5.4}$$

$$\frac{\dot{m}}{N_{stator}} = V_{radial,stator} \cdot b \cdot h_{stator} \cdot \rho_{stator,out} \tag{5.5}$$

Using the rotor tip blade speed $U_{rotor,in}$ and the relative tangential velocity at the rotor inlet $W_{\theta,in}$, the absolute tangential velocity at the rotor inlet $V_{\theta,in}$ can be calculated. Given the radial velocity component as calculated earlier, the stator outflow angle $\alpha_{stator,out}$ and stator outlet absolute velocity $V_{stator,out}$ can be calculated. These steps are shown in Equations 5.6 to 5.10.

$$U_{rotor,in} = 2\pi \cdot R_{rotor,in} \cdot \frac{\omega}{60} \tag{5.6}$$

$$W_{\theta,in} = V_{radial,rotor} \cdot tan(\beta_{rotor,in}) \tag{5.7}$$

$$V_{\theta,inlet} = U_{rotor,in} + W_{\theta,in} \tag{5.8}$$

$$\alpha_{stator,out} = arctan\left(\frac{V_{\theta,in}}{V_{radial,rotor}}\right) \tag{5.9}$$

$$V_{stator,out} = \sqrt{V_{\theta,in}^2 + V_{radial,rotor}^2} \tag{5.10}$$

Finally, the stator outlet Mach number $M_{stator,out}$, stator outlet flow area $A_{stator,out}$ and stator throat area $A_{stator,throat}$ can be calculated using the isentropic relations as can be seen in Equations 5.11 to 5.13.

$$\left(\frac{V_{stator,out}}{M_{stator,out}}\right)^2 \cdot \frac{1}{\gamma \cdot R} = \frac{T_t}{1 + \frac{\gamma-1}{2} \cdot M_{stator,out}^2} \tag{5.11}$$

$$A_{stator,out} = b \cdot h_{stator} \cdot cos(\alpha_{stator,out}) \tag{5.12}$$

$$\frac{A_{stator,out}}{A_{stator,throat}} = \left(\frac{\gamma+1}{2}\right)^{\frac{-(\gamma+1)}{2(\gamma-1)}} \cdot \left(1 + \frac{\gamma-1}{2} \cdot M^2_{stator,out}\right)^{\frac{\gamma+1}{2(\gamma-1)}} \cdot \frac{1}{M_{stator,out}} \tag{5.13}$$

Currently, the corner points of the stator face and rotor face at the sliding interface in Eilmer4 should match exactly. This means that in order to model just a single stator and a single rotor passage and apply periodic boundary conditions to reduce the computational cost, an equal number of stator and rotor blades have to be selected. Moreover, as the throat of the stator is choked, the only way to make sure the height of the mesh at the outlet of the static mesh matches the height of the mesh at the inlet of the rotating mesh, is to reduce the blade height at the rotor inlet such that this blade height together with the tip clearance adds up to the stator blade height.

The created aerodynamic mesh as just described will be referred to as the Eilmer4 mesh. Relating this back to the overall methodology of the project as described in Chapter 3, this procedure completes the infrastructure to create the Eilmer4 mesh and use it as an input of the Eilmer4 simulation preparation.

The next step is to transfer the aerodynamic mesh to the right format for the SU2 simulation. This mesh will be referred to as the SU2 mesh. A semi-automated method is established using the software tool Pointwise.[1] This method consists of the following steps for both the stator and the rotor mesh individually:

- Transform the coordinates of the Eilmer4 mesh from metres to millimetres as, due to the limited accuracy of Pointwise, importing the mesh with the coordinates in metres would result in open corners in the mesh.
- Run the Pointwise macro, which automatically groups and labels all boundaries of the mesh. The mesh is exported in the SU2 format.
- Scale the SU2 mesh from millimetres to metres.
- Apply periodic boundary conditions to the mesh.

Finally, a small tool is developed to combine the mesh of the stator and the rotor. This procedure completes the infrastructure to create the SU2 mesh and use it as an input for the SU2 simulation preparation.

With the completion of the procedure for creating the aerodynamic meshes for both the Eilmer4 and SU2 simulation, a semi-automated approach is used to generate the mechanical mesh based on the aerodynamic mesh to avoid any discrepancies between the meshes. The aerodynamic mesh generation tool has been extended with the capability of determining the coordinates of the blade contours at several span wise positions, as well as of the hub and blade tip profile and writing these to an output file. Creating the mechanical geometry and mesh is done using the software tools Solidworks[2] and ANSYS Workbench[3] by using the following procedure as documented in [69]:

- Read the blade and hub coordinates and transform these in the right format to be imported into Solidworks.
- Import the blade and hub coordinates into Solidworks and follow a step-by-step procedure to transform these coordinates into a full 3D model.
- Import this 3D model into ANSYS Workbench and follow a step-by-step procedure to create a mechanical mesh from this 3D model.

The shape of the hub and shaft of the turbine are based on several user defined geometrical dimensions. These dimensions include the thickness of the back face of the turbine $t_{backface}$, the axial length of the shaft L_{shaft}, the outer radius of the shaft $R_{outer,shaft}$ and the inner radius of the shaft $R_{inner,shaft}$. This can be

---

[1] http://www.pointwise.com/

[2] http://www.solidworks.com/

[3] http://www.ansys.com/

seen in Figure 5.3. The inner radius of the shaft can be set to be able to fit a second shaft through the centre, which has been used in previous turbine designs to apply a clamping force in order to push the turbine into the direction of the shaft. The outer radius of the shaft should be chosen carefully and in compliance with the seal and bearing design. As the back face of the shaft is subjected to an atmospheric pressure, a larger outer radius of the shaft will have a direct effect on the axial load in the system. Moreover, the connection between the shaft and the turbine is likely to experience high stresses due to the centrifugal loads in the turbine. Increasing the radius of this connection helps in reducing the peak stress as experienced during operation.

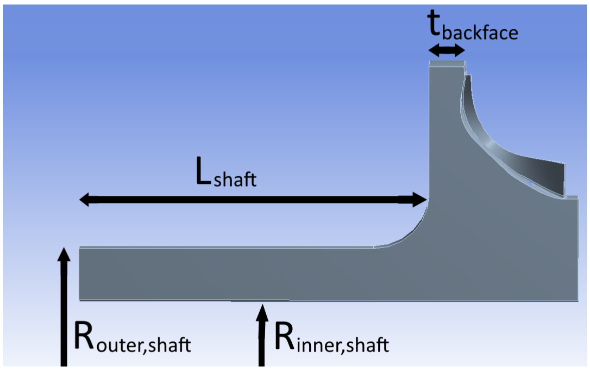

Figure 5.3: Side view of the mechanical model.

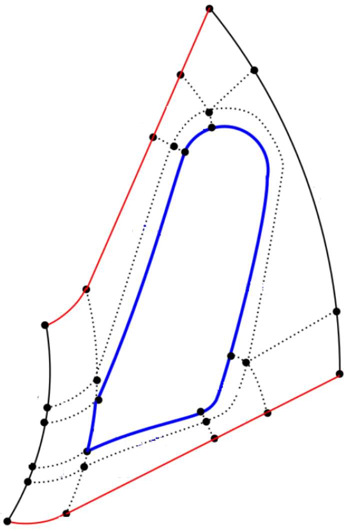

Figure 5.4: Schematic representation of the stator streamline in red [41].

These procedures are well-documented in the form of a user guide and the method can therefore be used in future research work to create the mechanical ANSYS model based on the aerodynamic Eilmer4 model in a relatively simple way [69]. The resulting mechanical mesh can be used as an input for the mechanical mesh preparation stage.

5.2. TURBINE EVALUATION PROCEDURE

In this Section, the procedure to evaluate the aerodynamic and mechanical performance of the turbine will be explained. First, the aerodynamic performance evaluation procedure will be elaborated upon in Section 5.2.1. This is followed by the mechanical stress evaluation procedure in Section 5.2.2.

5.2.1. AERODYNAMIC PERFORMANCE EVALUATION PROCEDURE

To evaluate the aerodynamic performance of the turbine, a procedure is developed which is compatible with both Eilmer4 and SU2 solution files. The user can specify the desired number of slices in the stator channel, rotor channel and rotor outlet section. When constructing the aerodynamic mesh, the meshing tool automatically writes the coordinates representing the streamline of the stator channel, rotor channel and rotor outlet section. The streamline of the stator is approximated by the centre line through the stator channel as can schematically be seen in Figure 5.4. In Figure 5.4, the blue line represent the stator blade contour, the dotted black lines represent the mesh blocks of the stator and the red line represents the centre line of the stator channel. For the rotor channel, the streamline data can be extracted directly from the mesh generation tool, as the streamline is used as a starting point for creating the passage shape. Finally, the rotor outlet streamline is represented by one of the edges of the helix which defines the shape of the rotor outlet mesh. For making the slices using the Eilmer4 solution file, the user has two options:

- Create slices using the i, j, k-coordinates, i.e. the internal coordinate system of the mesh. This method has the advantage that slices are made using the mesh coordinates directly. This allows for example for creating slices in the stator outlet blocks in an accurate way to capture the effect of the stator wake. Moreover, as the rotor channel mesh is based on the streamline data, extracting the rotor slices based on the i, j, k-coordinates allows for creating slices perpendicular to the fluid normal, which is not always possible when using the streamline data as will be seen in the next bullet point. The disadvantage of this method is that it cannot be used with an SU2 solution as the mesh in the SU2 solution file is not labelled in i, j, k-coordinates. Another disadvantage is that the relative position along the streamline has to be calculated indirectly, which can result in slices being projected onto the same relative position along the streamline.

- Create slices using the streamline data. In this method, slices are made perpendicular to the normal of the streamline. This method has the advantage that it can be used with both Eilmer4 and SU2 solution files and can therefore be used to compare the results. Another advantage is that in case of a highly skewed mesh, this method will still create slices perpendicular to the streamline normal. The disadvantage of this method is that, in case of a highly curved rotor blade, the slices made perpendicular to the streamline can intersect the rotor channel at two locations, resulting in invalid slice data. To avoid this, an extra option is added to the slicing tool which gives the user the possibility to neglect the tangential component of the streamline normal, thereby only taking into account the radial and axial components of the streamline normal for both the stator and the rotor slices.

As already mentioned, for the Eilmer4 solution files the user has the freedom to choose between both options, but only the second option can be used for post-processing the SU2 solution files as the mesh coordinates are only given in the global x, y, z reference frame in the SU2 output file. Additional equations are added to the solution files of both the Eilmer4 simulation and the SU2 simulation to:

- Calculate the relative properties in the rotor domain.
- Calculate the quantities which are not automatically given in the solution files.

To be consistent, these missing values are calculated for both the Eilmer4 solution file and the SU2 solution file, even though it might be directly given as an output in one of them. This is also used to verify the calculation of the missing quantities. First, the relative velocity components $\overrightarrow{W}$ are calculated using the absolute velocity components $\overrightarrow{V}$ and the grid velocity $\overrightarrow{V_{grid}}$. The latter is zero for the stator and is for the rotor dependent on the rotational speed and the location of the cell. This allows for calculating the relative Mach number $M_{relative}$. The calculation of the total temperature T_0 and $T_{0,relative}$ and total pressure p_0 and $p_{0,relative}$ both in the absolute and relative frame is done using the isentropic relations.[4] The entropy s and static enthalpy h are calculated using the ideal gas law.[5] Finally, the total enthalpy h_0 and $h_{0,relative}$ in both the absolute and relative reference frame can be calculated using the relation as given by Wilcox [79]. These Equations can be seen in Equation 5.14 to 5.23.

$$\overrightarrow{W} = \overrightarrow{V} - \overrightarrow{V_{grid}} \tag{5.14}$$

$$M_{relative} = \frac{|\overrightarrow{W}|}{a} \tag{5.15}$$

$$T_0 = T \cdot \left(1 + \frac{\gamma - 1}{2} \cdot M^2\right) \tag{5.16}$$

$$T_{0,relative} = T \cdot \left(1 + \frac{\gamma - 1}{2} \cdot M^2_{relative}\right) \tag{5.17}$$

$$p_0 = p \cdot \left(1 + \frac{\gamma - 1}{2} \cdot M^2\right)^{\gamma/(\gamma-1)} \tag{5.18}$$

$$p_{0,relative} = p \cdot \left(1 + \frac{\gamma - 1}{2} \cdot M^2_{relative}\right)^{\gamma/(\gamma-1)} \tag{5.19}$$

$$s = \frac{R}{1 - \frac{1}{\gamma}} \cdot ln\left(\frac{T_0}{T_{0,in}}\right) - R \cdot ln\left(\frac{p_0}{p_{0,in}}\right) \tag{5.20}$$

---

[4] https://www.grc.nasa.gov/www/k-12/airplane/isentrop.html

[5] https://www.grc.nasa.gov/www/k-12/airplane/entropy.html

$$h = \frac{R}{1 - \frac{1}{\gamma}} \cdot T \tag{5.21}$$

$$h_0 = h + \frac{|\vec{V}|^2}{2} + tke \tag{5.22}$$

$$h_{0,relative} = h + \frac{|\vec{W}|^2}{2} + tke \tag{5.23}$$

When the first option is chosen for creating the slices of an Eilmer4 simulation, the volume-averaged quantities are calculated using all cells of each slice. When the second option is chosen for either an Eilmer4 simulation or an SU2 simulation, the one-dimensionalised properties are extracted from the CFD results using the Onedval software tool developed by the University of Queensland [80]. Based on the information of a data slice of the CFD results, the Onedval program calculates the one-dimensionalised properties. The three methods available for one-dimensionalising the properties are:

- Area-weighted average.
- Flux-conserved average.
- Mass-flux-weighted average.

The area-weighted average method is the simplest method of the three. Currently, the flux-conserved average method in Onedval is based on the thermally perfect gas assumption. The method of taking the mass-flux-weighted average of the stator outlet conditions has also been used by Yamamoto [81]. According to the Onedval user guide [80], the method of mass-flux-weighted average is often used to compare the results of the CFD simulation with experimental results. For these reasons, it is decided to use the mass-flux-weighted average method for getting the one-dimensionalised properties. In this method, the average of some property ϕ is calculated according to Equation 5.24. In Equation 5.24, ρ is the density, $\vec{V}$ is the absolute velocity vector, $\vec{n}$ is the surface normal vector and A is the surface area of the block.

$$\phi = \frac{\int \phi \cdot \rho \cdot (\vec{V} \cdot \vec{n}) dA}{\int \rho \cdot (\vec{V} \cdot \vec{n}) dA} \tag{5.24}$$

The post-processing tool automatically plots the one-dimensionalised properties along the normalised streamline position, going from 0 to 1 for the stator, from 1 to 2 for the rotor and from 2 to 3 for the rotor outlet blocks. This gives a clear and thorough overview of the fluid behaviour in the turbine. Although the user has the freedom to choose the parameters to be plotted, the one-dimensionalised parameters that are automatically plotted are the total and static pressure, total temperature, entropy, total enthalpy, Mach number, blade loading and the turbulent kinetic energy. The total quantities are plotted both in the absolute and in the relative frame. Apart from the blade loading, all of these parameters are calculated by the Onedval tool. Similar as in the work of Zangeneh et al. [82], the blade passage loading per unit passage length dT/dL is calculated according to Equation 5.25 and is equal to the change in total enthalpy as calculated by the Onedval tool per length. As the calculation of the blade loading is found to be showing a scatter following a trend due to the sensitivity to the change in total enthalpy and the length between two data points, a polynomial is fitted through the data points to make the data more consistent.

$$\frac{dT}{dL} = \frac{d}{dL}(R \cdot V_\theta) = \frac{d}{dL}\left(\frac{h_0}{\omega}\right) \tag{5.25}$$

Moreover, a tool has been developed to be able to easily monitor the mass flow rate at the inlet, outlet and intermediate positions of the turbine for the transient Eilmer4 simulation. This can be used to evaluate the convergence of the transient simulation and the transient effects. On top of that, a tool has been developed to quantify the transient effect on the one-dimensionalised parameters as explained before. The minimum, maximum and mean value of the parameter at each location along the streamline is calculated. The user is also able to plot the mean of the transient simulation and the results of the steady-state simulation, thereby allowing for a good comparison between the solutions.

5.2.2. MECHANICAL STRESS EVALUATION PROCEDURE

The importance of taking into account the pressure loading due to the highly dense fluid during the mechanical design of an sCO$_2$ turbine was identified in the literature review in Chapter 2. Therefore, a semi-automated tool is created which extracts the pressure data of the surfaces of interest from the aerodynamic simulation solution files, i.e. the blade pressure side, the blade suction side and the hub surface. This tool is capable of using the aerodynamic design results of both the Eilmer4 and SU2 simulation.

Eilmer4 allows for extracting the pressure data of the surfaces of interest directly. For using the SU2 simulation results, a more sophisticated procedure is followed. Based on the coordinates of the surfaces of interest, as can be extracted from the aerodynamic mesh generation tool, the nearest cell in the SU2 results file is determined and the pressure data of this cell is saved. By repeating this step for all cells located at the surfaces of interest, a pressure map is created similar to the pressure map as extracted from the Eilmer4 simulation results. The creation of these pressure maps is done automatically.

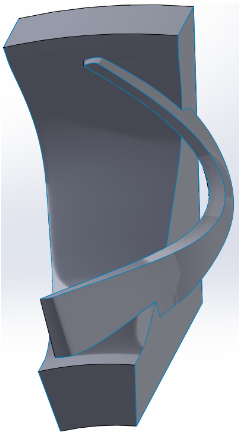

Figure 5.5: Example mechanical model without extension of the hub surface.

In case of highly curved rotor blades, the hub surface might have to be extended to a larger circumferential angle in order to fit the blade on the hub mesh. An example of this can be seen in Figure 5.5 where the hub contour represents $\frac{1}{N_{rotor}}$ of the full circle, with N_{rotor} the number of rotor blades. It can be seen that the hub contour has to be extended in order to fit the blade on the hub profile. To be able to use the pressure data as extracted earlier on the extended hub surface, the pressure data extraction tool calculates the radius-averaged pressure along the hub profile and creates a 360° pressure map of the hub profile data.

The pressure data of the blade pressure side, blade suction side and hub profile are written to text files which can be imported into ANSYS Workbench. This pressure data is automatically mapped to the nearest node of the mechanical mesh. The donor and receiver points can be plotted in ANSYS Workbench as a visual check of the established method.

Similar as seen in Figure 5.3, Figure 5.6 shows the side view of the mechanical model, including numbered edges. Edge 1 is in reality connected to the thrust bearing, and will therefore in the simulation be subjected to an atmospheric pressure. Edges 2, 3 and 4 will be subjected to the rotor inlet pressure and edges 5 and 6 to the rotor outlet pressure. Moreover, a constraint is placed on edge 1 during the mechanical simulation, allowing movement of this edge only in the radial direction.

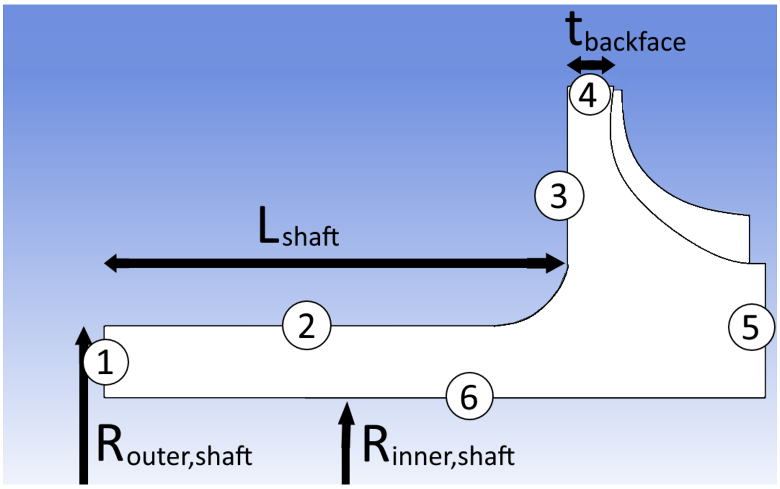

Figure 5.6: Side view of the mechanical model including edge labels.

6

AERODYNAMIC AND MECHANICAL DESIGN EVALUATION

In this Chapter, the three turbine generations as introduced in Chapter 3 will be presented. First, in Section 6.1 the Generation 1 turbine will be evaluated, which is based on the preliminary design results from zTurbo as presented in Chapter 4. This is followed by the Generation 2 turbine design in Section 6.2, which uses the preliminary design results from TOPGEN as will be explained. This Chapter concludes with the Generation 3 turbine design in Section 6.3.

6.1. GENERATION 1 TURBINE EVALUATION

First, the stator evaluation of the Generation 1 turbine will be elaborated upon in Section 6.1.1. Using the chosen stator geometry, the full turbine will be evaluated in Section 6.1.2. The main conclusions of Section 6.1 can be summarised as follows:

- The loss in the stator is minimal when 20 stator blades are used.
- No noticeable difference in loss is observed between using the ideal gas model and a look-up table with the real gas properties.
- The total-to-static efficiency is only 65%, which is mainly a result of extra losses due to over-acceleration of the flow at the stator exit and additional losses in the rotor channel, including tip clearance losses. Negative blade loading is found to be a contributor to losses in the rotor channel. To evaluate the mismatch in efficiency, a redesign of the turbine will be done using the results from the preliminary design tool TOPGEN.

6.1.1. AERODYNAMIC STATOR EVALUATION

To determine the number of stator blades, a single stator blade is analysed. Also the effect of using a look-up table with the real gas properties compared to the ideal gas model will be evaluated. To help stabilising the simulation, the flow angle at the inlet of the stator mesh is calculated to ensure it is aligned with the blade. Due to the difference in radius between the trailing edge of the blade and the inflow boundary, the inflow angle is different to the blade outflow angle $\alpha_{stator,out}$ as can be seen in Figure 6.1. Based on the blade outflow angle as found in the preliminary design, the radius at the stator outlet $R_{stator,out}$ and the radius of the inflow boundary $R_{mesh,in}$, the required inflow angle can be found. This method will also be used for the full turbine analysis.

When the stator is analysed without the presence of a rotor blade, a constant back pressure is specified at the outlet plane, resulting in a fluid moving from the high pressure to the low pressure region. If the outflow boundary is placed too close to the trailing edge of the blade, the specified constant pressure at the outflow boundary results in non-physical turning of the flow in the tangential direction as this low pressure wake cannot pass the fixed-pressure outlet boundary. However, for a choked radial inflow turbine with only slight supersonic speeds as analysed in this thesis, placing the outflow boundary at a too large distance from the trailing edge can result in a flow area smaller than the throat area somewhere downstream of the blade. This is due to the natural decrease in flow area in a radial inflow turbine. As this would make the actual throat of the stator ineffective, it is decided to place the outflow boundary at the trailing edge of the stator blades, thereby disregarding the wake of the blade. For doing a quick quasi-2D simulation of the stator, the hub and shroud walls in the 3D space can be assumed to be free-slip walls. The boundary conditions are summarised in Table 6.1, with an estimated $y+$ value of 3 at the blade suction surface. Similar as in the research of Persico [83], for the stator design the $k-\omega$ turbulence model is used.

Table 6.1: Generation 1 stator boundary conditions.

Boundary condition	Value
$T_{0,in}$ $[K]$	823
$p_{0,in}$ $[MPa]$	20
p_{out} $[MPa]$	9.1
Inflow angle $[deg]$	-46
Turbulence intensity [%]	5
Turbulent-to-laminar viscosity ratio $[-]$	100
Blade wall	Adiabatic
Hub and shroud wall	Free-slip

For quantifying the stator performance, the total pressure loss coefficient Y is evaluated as also done by Binder and Romey [84]. This loss coefficient is calculated using Equation 6.1. In Equation 6.1, $p_{0,in}$ is the total inlet pressure which is specified as an input condition to the CFD simulation at the inflow boundary condition. The total outlet pressure $p_{0,out}$ and static outlet pressure p_{out} are calculated by taking the average of the total and static pressure respectively of each cell of the plane located at the stator trailing edge. For extracting the one-dimensionalised properties from the CFD results, use has been made of the Onedval software tool as introduced in Section 5.2.1.

$$Y = \frac{p_{0,in} - p_{0,out}}{p_{0,in} - p_{out}} \tag{6.1}$$

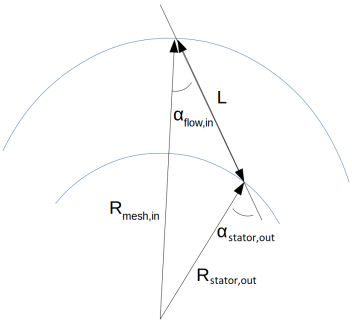

Figure 6.1: Sketch of the relation between blade outlet angle and inflow angle.

The effect of the number of blades on the loss coefficient is investigated by varying the number of stator blades from 15 to 25, which is in the order of similar turbines as seen during the literature review. This is considerably lower than the number of stator blades as suggested in the preliminary design, as the correlations for determining the number of stator blades in zTurbo are based on axial turbine correlations. Also the location of the throat, i.e. close to the trailing edge or further upstream, is investigated. Reichert and Simon [85] argue that the supersonic part of the stator is preferably as small as possible. However, making the supersonic part of the stator too short reduces the control over the expansion process in this section of the turbine. Based on these results, the stator geometry resulting in a low loss coefficient can be chosen.

When using 15 stator blades it is found that locating the throat too far downstream leads to a large wake of separated flow after the throat, thereby making the divergent part of the channel ineffective as can be seen in Figure 6.2. This is because of the shock wave boundary layer interaction due to over-expansion of the flow as a result of the rapid uncontrolled expansion in the supersonic part of the stator. That the flow separation is much reduced when locating the throat further upstream while using the same number of blades becomes evident when looking at Figure 6.3. For this reason, the results of the simulation with 15 stator blades and the throat located close to the trailing edge are omitted from any further analysis.

The total pressure loss coefficient Y as explained before is evaluated for all cases and can be seen in Figure 6.4. The stator blades with the throat located more upstream are denoted by the label *Throat up* and the stator blades with the throat located more downstream with *Throat down*. In Figure 6.4 it can be seen that the loss coefficient is minimal when using 20 stator blades. As the supersonic section of the stator is smaller when lo-

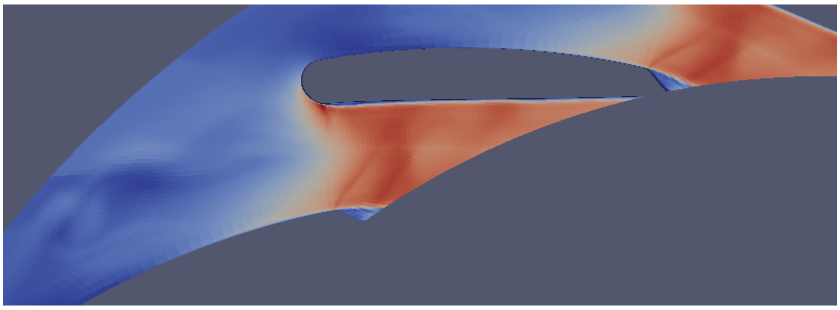

Figure 6.2: Qualitative Mach number distribution for 15 stator blades and the throat located more downstream.

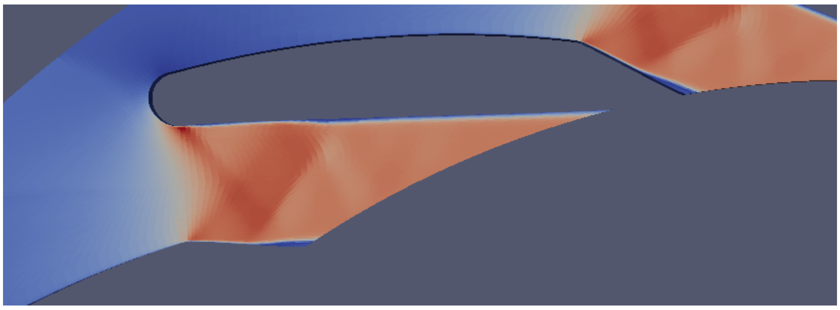

Figure 6.3: Qualitative Mach number distribution for 15 stator blades and the throat located more upstream.

cating the throat further downstream, it is decided to use this stator shape for the Generation 1 turbine design.

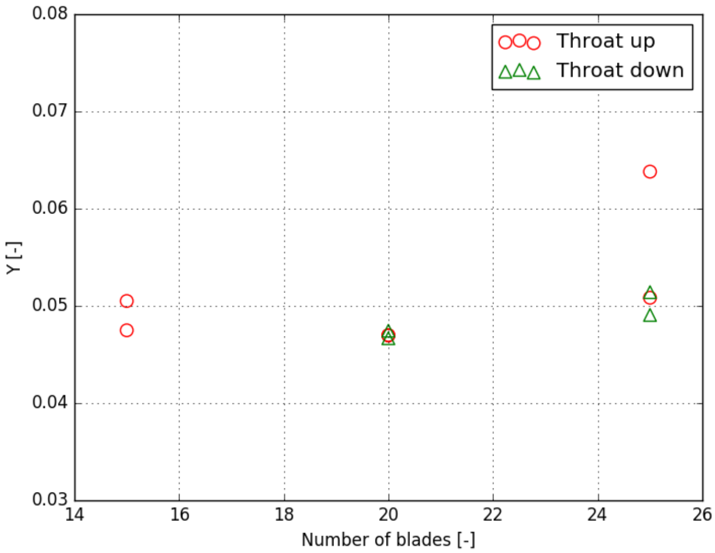

Figure 6.4: Loss coefficient versus the number of stator blades and throat location.

In order to do a comparative study between the ideal gas and real gas effects, similar as in the research of Rubechini et al. [24], a look-up table is generated containing the CO_2 properties from the Refprop database [34]. This study also helps to identify where real gas effects are more pronounced. The CO_2 properties from the Refprop database are based on the experimentally-derived Span and Wagner gas model [86], which is according to Sengers et al. [87] the most accurate equation of state for CO_2. The method of creating the uniform look-up table is derived from the work of Qi [88]. Whereas the work of Qi creates a look-up table based on a range of temperatures and pressures, the Eilmer4 code requires a table based on a range of internal energies and densities as suggested by Jacobs [89]. The modified tool allows for creating the look-up table in the correct format.

By specifying the temperature range and density range of the look-up table, the internal energies and density range can be obtained via the Refprop database. The temperature is varied from $500K$ to $1000K$ and the density is varied from $10kg/m^3$ to $200kg/m^3$. Based on the results of the preliminary design, the temperature and density in the stator and rotor of the turbine will be well within these ranges.

A grid convergence study based on the method developed by Qi [88] is done to make sure the table is sufficiently dense to guarantee a certain accuracy, while keeping the number of nodes in the table to a minimum to reduce the computational time. Based on a user defined temperature range and density range, the tool first creates a high resolution grid and evaluates the fluid properties at each node. Next, a coarse grid is created and the fluid properties at the nodes of the high resolution grid are calculated based on interpolation in the coarse grid. By comparing fluid properties of the high resolution grid and the interpolated coarse grid, the error at each node can be calculated. The error is calculated for the pressure, dynamic viscosity, ratio of specific heats, heat capacity at constant pressure, heat capacity at constant volume and enthalpy.

The maximum allowable error for the aforementioned parameters is set to 0.5%. This value is lower than the maximum error as found using the interpolation method as described by Ding et al. [90] and is therefore assumed to be sufficiently accurate. An example of the error across the domain of interest can be seen in Figure 6.5, where the error of the dynamic viscosity is shown versus the internal energy and the logarithmic density. The error is 0 at the nodes of the look-up table and the interpolation error is the largest in between two neighbouring nodes. This explains the wave pattern of the error as seen in Figure 6.5. By varying the number of nodes of the internal energy and the number of nodes of the density, the minimum number of nodes to get a maximum error of 0.5% across the domain can be found. The maximum error across the domain corresponds to the highest peak of Figure 6.5. The effect of the number of internal energy nodes and density nodes on the maximum error of interpolated variables can be seen in Figures B.1 to B.6 in Appendix B. When combining the results from Figures B.1 to B.6, it can be concluded that a minimum of 6 nodes for the internal energy and 20 nodes for the density are required to stay below the error limit of 0.5% for all variables. The relatively low number of required nodes show that the fluid properties vary approximately linearly in the domain of interest. Moreover, it is observed that the maximum error is found near the lowest internal energy, corresponding to a temperature of only $500K$, in the domain as seen in Figure 6.5. This shows the linearity of properties at the higher temperatures as likely found in the turbine, as the turbine outlet temperature according to the preliminary design is approximately $720K$.

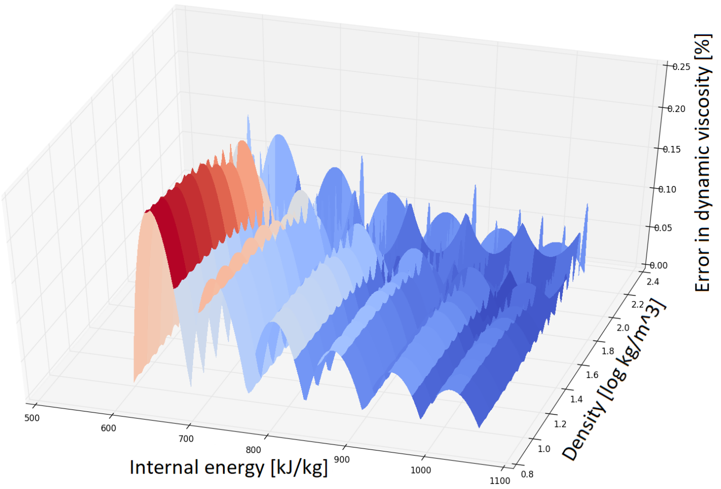

Figure 6.5: Example of the maximum error in interpolated dynamic viscosity across the domain.

For the comparison between the ideal gas model and the look-up table, the ratio of specific heats γ in the ideal gas model has been set equal to 1.238, which is the average γ of the inlet and outlet of the turbine according to the preliminary design results. Using the ideal gas model as implemented for CO_2 in Eilmer4, a 2.8% higher mass flow rate is measured compared to the look-up table results. Whereas the total pressure in the throat is similar between the two analyses, it is found that for the simulation using the ideal gas model the total temperature in the throat is approximately 3% lower compared to the look-up table simulation, which explains the difference in mass flow rate by looking back at Equation 5.1. No noticeable difference is observed in the loss coefficient Y of the ideal gas and look-up table analyses. Research by Kalra et al. [11] shows that when using the perfect gas assumption during the CFD simulation, the estimated efficiency is slightly higher compared to a simulation using a look-up table. Based on this observation together with observations made during the literature study review, it is decided to use this ideal gas law for the full turbine simulation as this simplifies and speeds up the calculation.

6.1.2. AERODYNAMIC FULL TURBINE EVALUATION

Based on the preliminary design results, a 3D geometry is created using the aerodynamic meshing method as explained in Chapter 5. One of the current limitations of the Eilmer4 simulation is that the mesh at the stator outlet and rotor inlet should match, meaning that only an equal number of stator and rotor blades can be modelled. Based on the observations made in Section 6.1.1, the number of stator and rotor blades are both set equal to 20. The most important design parameters as used in the user input files are summarised in Table 6.2.

Table 6.2: Generation 1 turbine geometric parameters summary.

Stator		Rotor	
Parameter	Value	Parameter	Value
N_{stator} $[-]$	20	N_{rotor} $[-]$	20
$R_{stator,LE}$ $[mm]$	60.8	$R_{rotor,LE}$ $[mm]$	42.7
$R_{stator,TE}$ $[mm]$	45	$R_{rotor,TE,mean}$ $[mm]$	25
$R_{stator,throat}$ $[mm]$	48	$h_{rotor,in}$ $[mm]$	0.9
h_{stator} $[mm]$	1	$h_{rotor,out}$ $[mm]$	3.6
α_{stator} $[deg]$	70	$h_{rotor,tcl,in}$ $[mm]$	0.1
$M_{stator,out}$ $[-]$	1.14	$R_{rotor,tcl,out}$ $[mm]$	0.144
		z_{rotor} $[mm]$	13
		$\beta_{rotor,LE}$ $[deg]$	53
		$\beta_{rotor,TE}$ $[deg]$	60
		$t_{rotor,root}$ $[mm]$	2
		$t_{rotor,tip}$ $[mm]$	1.5
		ϕ_{rotor} $[deg]$	11

In Table 6.2, N is the number of blades, R is the radius, h is the blade height, t is the blade thickness, z is the axial length, α is the flow angle, β is the blade angle and ϕ is the twist angle. The subscripts LE and TE refer to the leading edge and trailing edge respectively, tcl stands for tip clearance, $root$ refers to the blade root and tip refers to the blade tip.

As can be seen in Table 6.2, the radius of the stator at the tip of the leading edge has been increased compared to the preliminary design as a smaller radius seemed to be impractical considering the required stator outlet flow angle. Moreover, the inlet radius of the rotor has been slightly decreased as the stator-rotor clearance of only 5% of the radial stator chord as used during the preliminary design is lower than seen in practice. Increasing this clearance to 15% is more in line with designs as found in literature [91]. This change results in an estimated efficiency drop of approximately 2% according to zTurbo. According to Qi et al. [13], typical values for the tip clearance for radial inflow turbines is 9% in the axial direction and 4% in the radial direction, with a minimum value of $0.1\,mm$ due to manufacturing limitations. A similar blade thickness is used as in the research of Russell et al. [6].

The turbine is analysed in the steady-state solver SU2. An overview of the gas properties used in the simulation is given in Table B.1. These properties come from the ideal gas library of Eilmer4 and the ratio of specific heats γ is taken as the average value between the turbine inlet and outlet according to the preliminary design. As a starting point, all walls are assumed to be free-slip walls. An overview of other simulation parameters can be found in Table B.2. The SST turbulence model as implemented in SU2 is used during the simulation. The rotor design tool ensures a smooth variation of geometric flow parameters along the streamline and this variation can be seen in Figure B.7.

The quality of the mesh is assessed using the software tool Pointwise. The aspect ratio of the cells in the boundary layer can be in the order of 1000 in case cells are sufficiently orthogonal [92]. Moreover, a smooth variation of cell area is assured as much as possible. It is acknowledged that due to the meshing method of the meshing tool the smooth variation in cell area is more difficult to obtain in certain areas of the flow domain, like for example close to the stator throat and in the tip clearance cells of the rotor. Also the skewness of the cells can be large in certain regions as a result of the short supersonic section of the stator compared to the stator length and due to the meshing method in the rotor domain. One of the areas that is identified during the simulation as an area in which extra mesh refinement is required is the supersonic part of the stator. In this region the expansion fans and shock waves require a more refined mesh. By doubling the number of cells in the supersonic part compared to the first simulation the local peak values in momentum residuals are greatly reduced as can be seen in Figures B.8 and B.9.

For the convergence history and residuals, the reader is referred to Appendix B. The convergence history of the simulation can be seen in Figure B.10, which is started in first order and switched to second order after 1000 iterations. By taking a closer look at the residuals by visualising them in the flow field a better understanding can be obtained of the location of the residuals. The regions of interest for the residuals of the density, momentum, Turbulent Kinetic Energy (TKE) and omega can be seen in Figures B.11 to B.14 respectively. It can be noted that the highest density residuals are found at the periodic boundary of the rotor outlet blocks, even after refining the mesh in that region. The highest momentum residuals are found in what seem to be random locations in the rotor channel, where local peak values can be found in the middle of the fluid domain. Even when using a coarse mesh these residuals are present at the same location, thereby giving a similar convergence history. Because of computational limitations, refining the mesh in these regions even more is not feasible. Therefore it is decided to use these results to evaluate the turbine performance. A possible explanation of the slow convergence can be that the flow is inherently unsteady. It can be noted that the peak TKE residuals and omega residuals are at the inlet plane of the stator. This is expected to be a result of forcing a turbulent flow to enter the stator domain which is actually a laminar or transition region.

The main results are summarised in Table 6.3. The variation of the properties across the turbine is visualised in Figure 6.6, where the relative position goes from 0 to 1 for the stator, from 1 to 2 for the rotor channel and from 2 to 3 for the rotor outlet blocks. Figure B.15 can give the reader an idea of the location and orientation of the slices, which go from the stator inlet in the top-left corner to the end of the rotor outlet blocks at the bottom.

Table 6.3: Generation 1 turbine main results.

Parameter	Value CFD	Value zTurbo
η_{ts} [%]	65.1	88.6
η_{ts} reduction stator [%]	6.6	5.4
η_{ts} reduction stator-rotor interspace [%]	5.5	0
η_{ts} reduction rotor [%]	20.8	3.3
Degree of reaction [$-$]	0.10	-0.02

By looking at the total pressure, total temperature, total enthalpy and entropy, it can be seen that the losses in the stator up to the location of the throat are small. The shock wave in the supersonic part of the stator as a result of over-expansion can be seen by looking at the pressure distribution in this area in Figure 6.7. Losses in total pressure are a result of this shock wave. As the slices in the stator are not parallel to this shock, this reduction is not abrupt in Figure 6.6 but is spread out over multiple slices. It can be seen that a peak value of TKE is present at the stator inlet, which explains the peak in TKE residuals at that location as mentioned before. A gradual increase in Mach number can be seen across the stator. Due to the orientation of the slices, which are not exactly aligned with the local streamline, the fluid properties in the supersonic region of the stator are not perfectly represented, as can be seen by the Mach number which seems to exceed 1.0 by a small amount in the stator. When looking at the flow field, Mach 1 is reached in the stator throat and the flow is further expanded to approximately Mach 1.5, after which the flow is decelerated again by means of a normal shock. This leads to an increase in static pressure at the stator outlet. To get more control over this part of the expansion process, a more sophisticated blade design method has to be used for the supersonic part of the stator. The study on the exact blade curvature and the implementation of this in the meshing tool would

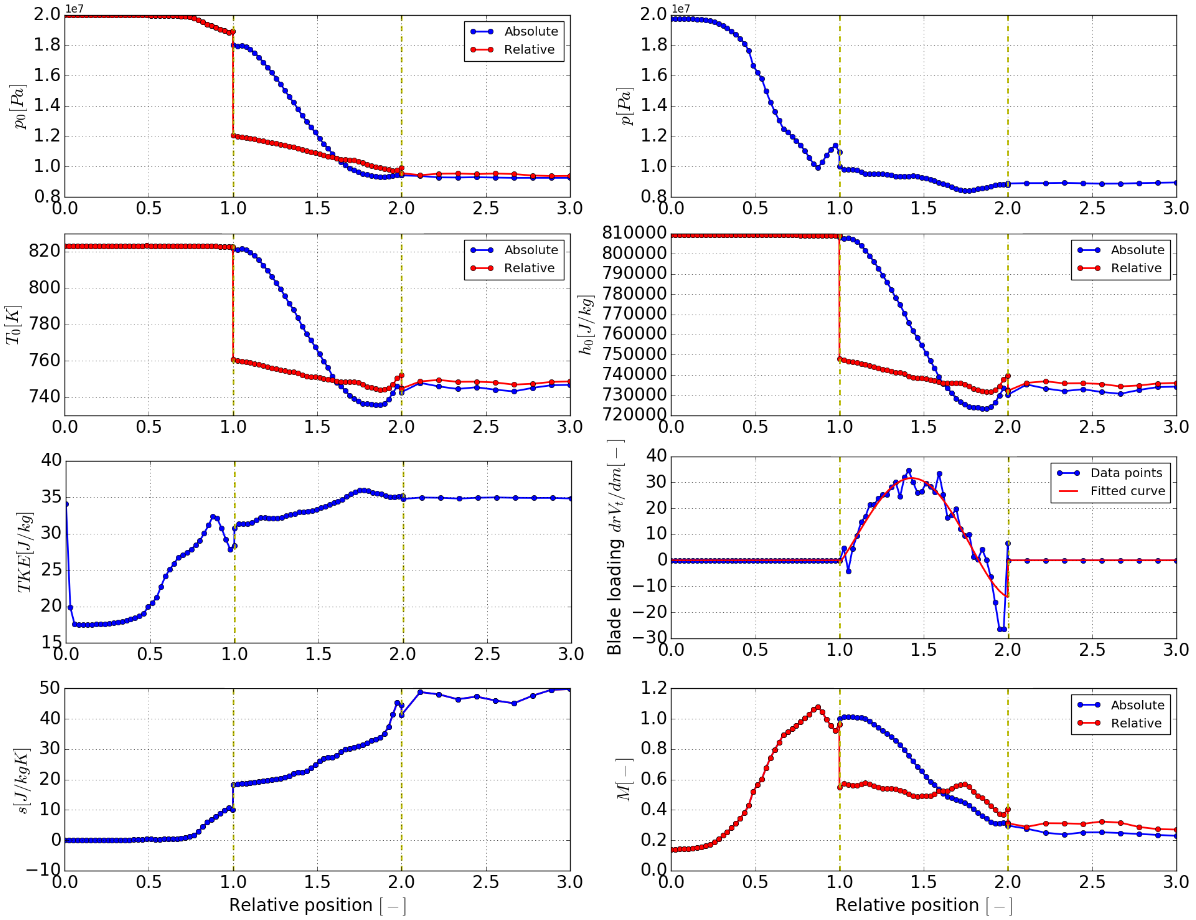

Figure 6.6: Generation 1 turbine variation of properties across the turbine.

be a new project by itself and is therefore outside of the scope of the current thesis project. The wake of the stator is identified as a region where the entropy generation is large, which can be seen by the steep increase in entropy for the last part of the stator. This shows the value that can be added when more sophisticated stator blade design tools are implemented in the meshing tool.

There is a small gap between the last slice of the stator and the first slice of the rotor. This explains the discrepancy between for example the stator outlet and rotor inlet static pressure. At the mixing plane between the stator and the rotor, an increase in entropy can be seen. This is due to mixing losses in the mixing plane and is not taken into account for the preliminary design as seen in Table 6.3. It can also be seen that the losses in the rotor show large discrepancies between the preliminary and CFD results. In the rotor channel a gradual change in total pressure, total temperature, total enthalpy, entropy, static pressure and Mach number can be seen. Part of the rotor blade close to the trailing edge has a negative blade load, indicating that this part of the rotor actually does work on the flow instead of the other way around. This also explains the steep increase in total absolute temperature and total absolute enthalpy in this region. When looking at the flow solution in more detail, one can see that the tip clearance near the rotor inlet causes a large velocity flow in this tip clearance region. As the rotor has a non-zero blade angle at the leading edge, this tip clearance flow near the rotor inlet has a radial component. This is visualised in Figure 6.8, which shows a large positive X-momentum in the tip clearance region, indicating the flow going radially outward. It can also be seen that a small separation region starts to form at the suction side of the blade, leading to reverse flow as can be seen in Figure 6.9, where a negative Z-momentum indicates reverse flow. This can be an effect of the low pressure gradient in the rotor. As a result of the Coriolis effect, the flow in this separated region is pushed towards the shroud, thereby creating a vortex further downstream as can be seen in Figure 6.10.

The degree of reaction of the turbine as predicted by SU2 is 0.10. To have conservation of rothalpy across

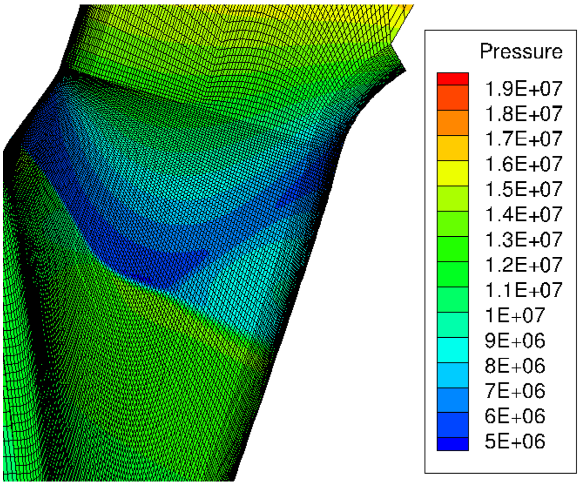

Figure 6.7: Generation 1 turbine pressure distribution in the supersonic part of the stator.

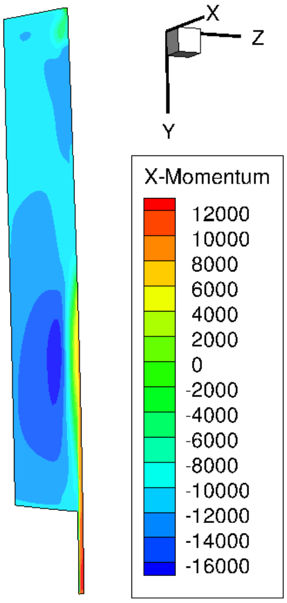

Figure 6.8: Generation 1 turbine X-momentum near the rotor inlet.

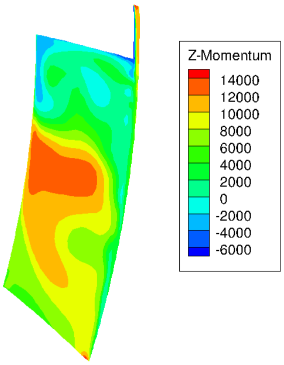

Figure 6.9: Generation 1 turbine Z-momentum in the rotor channel.

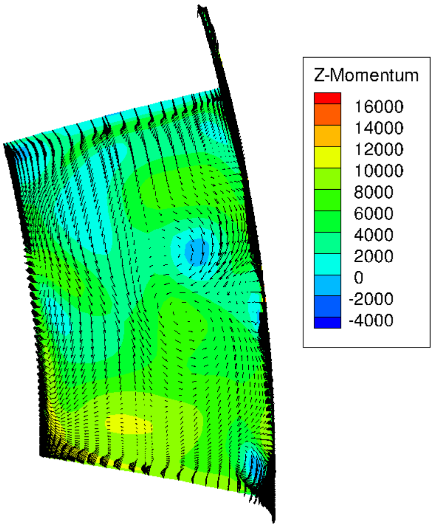

Figure 6.10: Generation 1 turbine vortex in the rotor channel.

the rotor stage, a deceleration of the flow can ensure a low degree of reaction. However, a decelerating flow is also susceptible to separation or reverse flow. This is in line with the effect explained by Knoernschild [32] as identified in the literature review in Chapter 2, who states that designing a pure impulse radial inflow turbine is expected to be not possible and that some pressure drop is required across the rotor channel. Nonetheless, a total-to-static efficiency of 65.1% can be achieved according to the SU2 simulation, which is high given the low specific speed and the line of maximum achievable efficiency as presented in Figure 4.16. This efficiency is lower than the efficiency estimated by zTurbo, which can be a result of neglecting the tip clearance and mixing losses during the 1D design and the negative blade loading. Therefore, the turbine geometry will be redesigned based on a 1D design in TOPGEN, which takes into account tip clearance losses and uses loss correlations for small scale radial inflow turbines. This redesign uses the same head and flow coefficient as the Generation 1 turbine design to see if this Generation 2 turbine shows better performance for a low reaction turbine. This will be discussed in Section 6.2.

6.2. GENERATION 2 TURBINE EVALUATION

To assess the effect of the mismatch in estimated efficiency between the 1D design using zTurbo and the 3D aerodynamic design, a redesign of the Generation 1 turbine is done using the University of Queensland's in-house 1D design tool TOPGEN [15]. This can give insight in the effect on the turbine geometric parameters and corresponding efficiency if the tip clearance loss is taken into account during the preliminary design. Based on several input parameters, including the head coefficient and flow coefficient, TOPGEN gives the rotor geometry and a breakdown of the losses. First, in Section 6.2.1 the preliminary design in TOPGEN will be explained. This is followed by the aerodynamic evaluation of the turbine in Section 6.2.2, which includes a comparison of the SU2 and Eilmer4 results. The main conclusions of Section 6.2 can be summarised as follows:

- For a similar turbine geometry, TOPGEN estimates a 15 percentage points lower efficiency compared to zTurbo. This is mainly due to an increase in estimated passage losses and tip clearance losses.

- The results of the steady-state SU2 simulation and the mean of the transient Eilmer4 simulation are in agreement when comparing the turbine efficiency and the variation of properties, like for example Mach number, across the turbine.

- The transient effects have a significant influence on the blade loading of the rotor, which affects the flow field and entropy generation in the turbine.

- The total-to-static efficiency is 69.5%, which is over 4 percent points higher than the Generation 1 turbine. High losses are found in the stator-rotor interspace, which can be a result of the over-expansion of the flow at the stator outlet. The mass flow rate, determined by the throat area of the choked stator, is $2.8 kg/s$, which is lower than the design value of $3 kg/s$. To reduce the over-expansion, a redesign of the Generation 2 turbine will be done, which uses the same rotor but has an increased stator throat area to match the design mass flow rate.

6.2.1. PRELIMINARY DESIGN

One of the advantages of TOPGEN compared to zTurbo is that the zero-swirl condition at the rotor outlet can be given as an input, so the rotor outlet blade angle is calculated automatically. Moreover, the tip clearance loss is estimated based on experimental data from NASA on small-scale turbomachinery design [13] [93].

The flow coefficient φ and head coefficient ψ of the Generation 1 turbine design are calculated using Equations 6.2 and 6.3 based on the zTurbo output parameters from the preliminary design [13]. The same flow and head coefficient are used as input values for the TOPGEN turbine design.

$$\varphi = \frac{V_{rotor,out}}{U_{rotor,in}} \tag{6.2}$$

$$\psi = \frac{V_{\theta,in}}{U_{rotor,in}} - \frac{R_{rotor,out,tip}}{R_{rotor,in}} \cdot \frac{V_{\theta,out}}{U_{rotor,in}} \tag{6.3}$$

By manually tweaking the loss coefficient calculation in TOPGEN to give the same estimated output power of $313 kW$ as seen in the zTurbo calculation, a geometry similar to the Generation 1 turbine is obtained. This design is labelled as TOPGEN1. By removing the modifications to the loss coefficient calculation, a rotor geometry is created which takes into account the extra losses when creating the rotor shape. As TOPGEN uses the user defined output power, the mass flow rate is increased to compensate for the loss in efficiency. This design is labelled as TOPGEN2. To be able to make a comparison with the Generation 1 turbine, the desired output power of the TOPGEN turbine is reduced to have a mass flow rate equal to the Generation 1 turbine design. This design is labelled as TOPGEN3. The performance characteristics of these turbine designs as estimated by TOPGEN, as well as the preliminary zTurbo design, are summarised in Table 6.4. Table 6.4 shows the total-to-static efficiency η_{ts}, degree of reaction r, output power P_{out}, mass flow rate $\dot{m}$, total loss Z_{total}, passage loss $Z_{passage}$, tip clearance loss Z_{tcl} and exit kinetic energy loss Z_{KE}.

The percentage values of the losses in Table 6.4 give the reduction in total-to-static efficiency corresponding to that loss. By summing up the losses of the TOPGEN1 design, a total-to-static efficiency of 70% is estimated by TOPGEN, i.e. the loss calculation of the TOPGEN1 design is modified to estimate a 15% higher

Table 6.4: TOPGEN turbine designs performance comparison.

Parameter	zTurbo	TOPGEN1	TOPGEN2	TOPGEN3
η_{ts} [%]	89	85	74	73
r [−]	-0.02	0.11	0.23	0.24
P_{out} $[kW]$	313	313	313	265
$\dot{m}$ $[kg/s]$	3.00	3.09	3.54	3.06
Z_{total} $[kW]$		43.5	31.0	32.8
$Z_{passage}$ $[kW]$	(8.6%)	24.0 (16.6%)	17.0 (14.3%)	17.8 (15.0%)
Z_{tcl} $[kW]$	(0%)	16.0 (11.0%)	11.0 (9.2%)	12.0 (10.0%)
Z_{KE} $[kW]$	(2.8%)	3.5 (2.4%)	3.1 (2.6%)	3.0 (2.5%)

efficiency in order to match the zTurbo output power. It can be seen that the tip clearance losses reduce the total-to-static efficiency by approximately 10% and are responsible for a significant part (approximately 36%) of the total losses. The estimated value of the degree of reaction for the TOPGEN1 design is close to the value measured in the SU2 simulation as discussed in Section 6.1. Also, higher passage losses are expected by TOPGEN compared to zTurbo. The passage losses in TOPGEN are based on the CETI loss model from Baines [91] and a combination of the skin friction and secondary flow loss model from Musgrave [94] and Rodgers [95].

6.2.2. AERODYNAMIC FULL TURBINE EVALUATION

A summary of the geometric parameters of the Generation 2 turbine is given in Table 6.5. The variation of these geometric parameters along the streamline can be seen in Figure B.16. When comparing these values to the geometric parameters of the Generation 1 turbine as given in Table 6.2, it can be noticed that the diameter of the rotor inlet has been decreased, which also results in a reduced stator diameter. The rotor outlet blade height is increased with over 10% compared to the Generation 1 turbine to allow for sufficient expansion taking into account the tip clearance losses, which are not accounted for in the Generation 1 turbine design. Moreover, as for the TOPGEN calculation 16 instead of 20 rotor blades are used, the blade thickness for the Generation 2 rotor is reduced by 20% in order to have the same outflow area as used in the TOPGEN calculation. The calculated stator outlet Mach number by using the method as explained in Chapter 5 is larger than the value suggested by the TOPGEN code. As a result, the expansion in the stator is expected to be larger, thereby reducing the degree of reaction compared to the degree of reaction seen in Table 6.4.

Table 6.5: Generation 2 turbine geometric parameters summary.

Stator		Rotor	
Parameter	Value	Parameter	Value
N_{stator} $[-]$	20	N_{rotor} $[-]$	20
$R_{stator,LE}$ $[mm]$	49.1	$R_{rotor,LE}$ $[mm]$	41.3
$R_{stator,TE}$ $[mm]$	43	$R_{rotor,TE,mean}$ $[mm]$	24.6
$R_{stator,throat}$ $[mm]$	46	$h_{rotor,in}$ $[mm]$	0.9
h_{stator} $[mm]$	1	$h_{rotor,out}$ $[mm]$	4.08
α_{stator} $[deg]$	68	$h_{rotor,tcl,in}$ $[mm]$	0.1
$M_{stator,out}$ $[-]$	1.12	$R_{rotor,tcl,out}$ $[mm]$	0.144
		z_{rotor} $[mm]$	13.4
		$\beta_{rotor,LE}$ $[deg]$	50.6
		$\beta_{rotor,TE}$ $[deg]$	59
		$t_{rotor,root}$ $[mm]$	1.6
		$t_{rotor,tip}$ $[mm]$	1.2
		ϕ_{rotor} $[deg]$	11

The same SU2 gas parameters and simulation parameters are used as for the Generation 1 turbine and are summarised in Tables B.1 and B.2. For the convergence history and residuals, the reader is referred to Appendix B. The convergence history of the inviscid simulation of the Generation 2 turbine can be seen in Figure B.17, which is started in first order and switched to second order after 900 iterations. By taking a closer look at the residuals by visualising them in the flow field, a better understanding can be obtained of the location of the residuals. In the stator domain, a peak in residuals of both the TKE and omega are found at the inlet boundary condition, which is again expected to be due to forcing a turbulent flow to enter a laminar or transition region. Apart from the turbulence residuals at the inlet boundary, no other region of peak residuals is identified in the stator domain, indicating that the level of quality of the mesh in this region is sufficient. The regions of interest for the residuals of the density and Z-momentum can be seen in Figures B.18 to B.19 respectively. Similar as for the Generation 1 turbine, it can be noted that the highest density residuals are found at the periodic boundary of the rotor outlet blocks, even after refining the mesh in that region. The highest momentum residuals are found in the rotor channel in the middle of the fluid domain. Because of computational limitations, refining the mesh in these regions even more is not feasible. Therefore it is decided to use these results to evaluate the turbine performance.

The Eilmer4 gas parameters and simulation parameters are used are summarised in Tables B.3 and B.4. The transient Eilmer4 simulation turns out to be unstable during start-up when using an initial flow field described by a constant pressure and temperature field in the turbine. This is likely to be due to high local velocities going in random directions during the first iterations of the simulation, as the main flow field has not developed yet. To overcome this issue, the capability of the Eilmer4 simulation setup file has been extended to give the user the possibility to start the simulation with a flow field with a fixed velocity. The direction of this velocity component is determined for every cell according to the local streamline direction, as also used for the post-processing tool as explained in Chapter 5. An absolute velocity of $50m/s$ is used to initialise the flow field. By using this method, the start of the simulation is more stable as the flow travels in approximately the right direction from the beginning.

The initial results of the Eilmer4 simulation showed unrealistic flow behaviour around the sliding interface between the stator and the rotor, which propagated through the rotor channel. At the sliding interface a jump in total absolute pressure, total absolute temperature, static temperature and Mach number to higher values was observed. Reviewing the sliding mesh calculation of Eilmer4 showed it contained two bugs:

- At the sliding interface, the stator properties in the absolute reference frame were compared to the rotor properties in the relative reference frame, whereas this comparison should be done in the same reference frame. This is fixed by transforming the rotor properties to the absolute reference frame for the stator calculation and by transforming the stator properties to the relative reference frame for the rotor calculation.
- An error was made in the calculation of the rothalpy I at the rotor inlet. Where previously Equation 6.4 was used to calculate the rothalpy, this has now been changed to the correct relation shown in Equation 6.5. In Equations 6.4 and 6.5, V is the absolute velocity component, V_{grid} is the grid velocity and W is the relative velocity.

$$I = h_{relative} = C_v \cdot T + \frac{p}{\rho} + \frac{(V_x - V_{grid,x})^2 + (V_y - V_{grid,y})^2 + (V_z - V_{grid,z})^2}{2} \tag{6.4}$$

$$I = h_{relative} = C_v \cdot T + \frac{p}{\rho} + \frac{|\overrightarrow{W}|^2 - |\overrightarrow{V_{grid}}|^2}{2} \tag{6.5}$$

The main results are summarised in Table 6.6. The variation of the properties across the turbine is visualised in Figure 6.11, where solid lines denoted by SS show the steady-state SU2 results and the dashed lines denoted by T show the mean of the transient Eilmer4 results.

Table 6.6: Generation 2 turbine main results.

Parameter	Value SU2	Value Eilmer4 (mean)	Value TOPGEN	Value Generation 1 turbine
η_{ts} [%]	69.5	69.7	73	65.1
η_{ts} reduction stator [%]	5.2	5.2	Unknown	6.6
η_{ts} reduction stator-rotor interspace [%]	6.8	5.2	Unknown	5.5
η_{ts} reduction rotor [%]	15.9	17.1	Unknown	20.8
Degree of reaction [−]	0.05	0.07	0.24	0.10

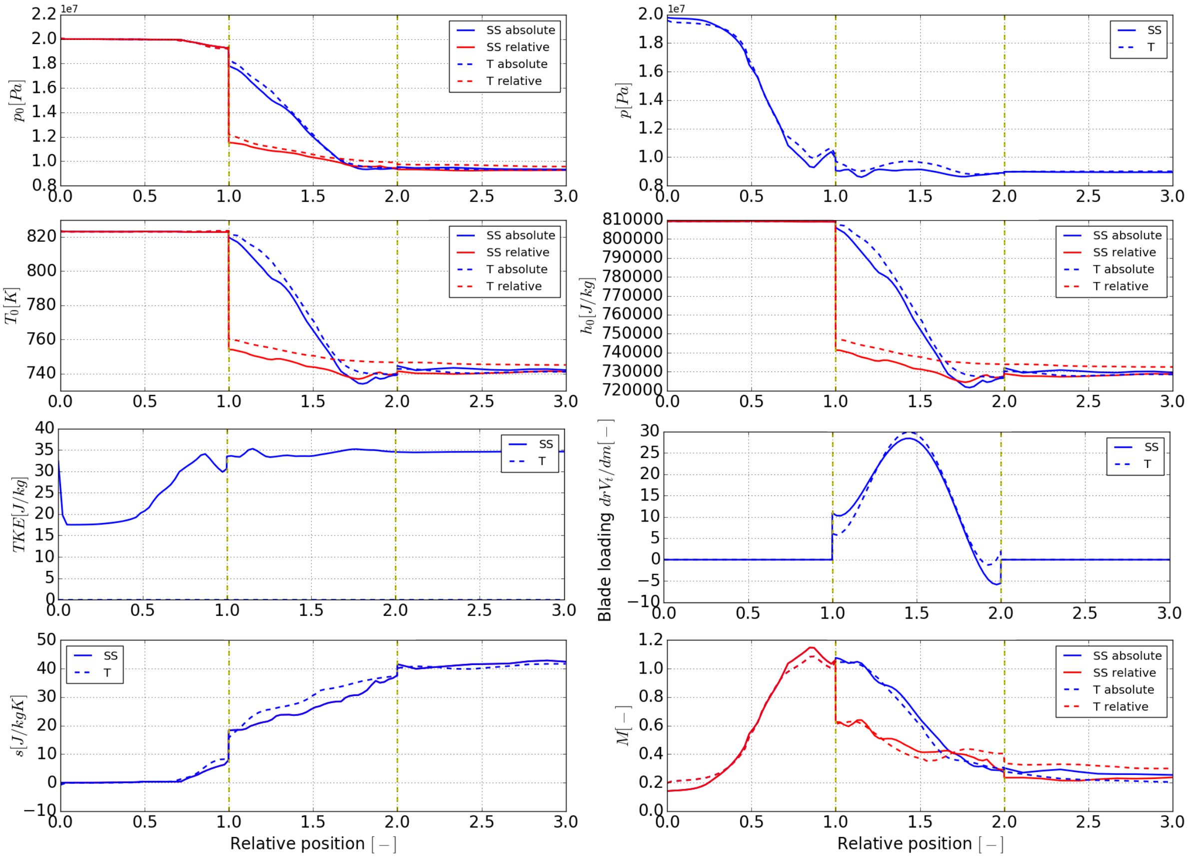

Figure 6.11: Generation 2 turbine comparison steady-state and transient variation of properties across the turbine.

When comparing the variation of properties across the turbine for the steady-state Generation 2 and the Generation 1 turbine, it can be noticed that the expansion in rotor channel is more continuous when looking at the pressure and Mach number distribution. The overall entropy generation in the rotor channel is reduced by approximately 25%. Also the entropy generation in the stator has decreased compared to the Generation 1 turbine as derived from Table 6.6. Still, high supersonic velocities are found in the stator as can be seen in Figure 6.12. Due to the orientation of the slices, which is similar to the slices seen in Figure B.15, the abrupt variation of properties near the shock wave is spread over multiple slices. Overall, a total-to-static efficiency of 69.5% is expected to be achieved according to the SU2 results. This is an improvement of over 4% compared to the Generation 1 turbine. The small pressure drop across the rotor results in a low degree of reaction of only 0.05.

The flow field of the Eilmer4 simulation is extracted at 18 time steps where the turbine rotates approximately 1° compared to the previous time step. These 18 time steps represent a rotor blade passing a single stator passage. The mass flow rate is evaluated at the inlet and outlet of the turbine at each of these time steps. The outlet mass flow rate oscillates around the inlet mass flow rate as can be seen in Figure 6.13. The transient variations of properties across the turbine for the Generation 2 turbine are summarised in Figure 6.14, showing the mean, the maximum value and the minimum value found at each relative position for the considered time steps. The discrepancy across the sliding interface is again due to the gap in between the last slice of the stator and the first slice of the rotor as explained before.

One of the noticeable phenomena in Figure 6.14 is the increase in total pressure and total temperature at the end of the stator for the $High$ curve. This behaviour is expected to be a result of the negative blade loading near the inlet of the rotor for some of the time steps and corresponds to a large increase in entropy. This indicates that those parts of the turbine are actually doing work on the fluid. Due to the rotor inlet blade angle, the work done on the fluid will have a result on the total pressure and total temperature at the end of the stator. Figure 6.15 shows the stator domain and the first part of the rotor domain. It can be seen that

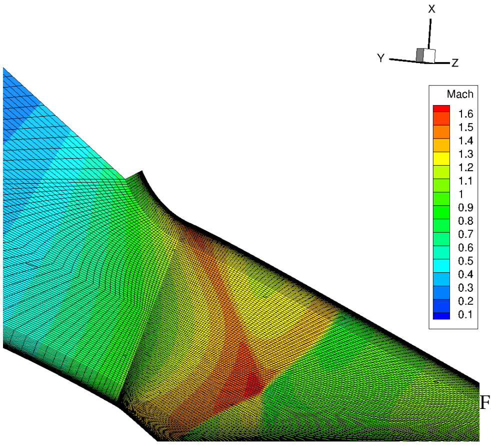

Figure 6.12: Generation 2 turbine SU2 Mach number distribution in the stator.

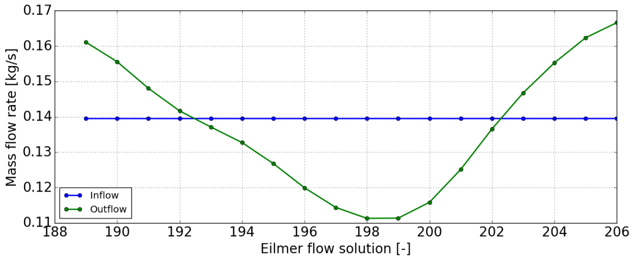

Figure 6.13: Generation 2 turbine Eilmer transient mass flow variation.

there is a high velocity tip clearance flow which, due to the non-zero rotor blade inlet angle, results in a strong radial component of the flow in the tip clearance region as can be seen by the high positive value of $vel.x$. This results in mixing losses and brings the flow from downstream regions more upstream, thereby increasing the entropy of the upstream region. This high velocity tip clearance flow results in a vortex as can be seen in Figure 6.16, which shows the relative Mach number at several slices across the rotor channel. Finally it can be seen that a large part of the total entropy increase happens in the stator and in the gap in between the stator and the rotor, particularly when the first part of the rotor blade is negatively loaded.

When comparing the mean of the transient results with the steady-state SU2 results as shown in Figure 6.11, several observations can be made:

- A good agreement is found between the change in total pressure and static pressure in the stator and rotor channel. The static pressure in the rotor channel shows more fluctuations in the transient simulation than in the steady-state simulation. This is related to the fluctuations in the relative Mach number in the rotor channel caused by the vortex as explained before.

- There is a reasonable agreement for the total absolute and relative temperature. As a result of the mixing plane in the steady-state simulation, a larger drop in total temperature is seen at this location compared to the transient simulation. The trend of the variation in total temperature in the rotor channel is comparable between the analyses.

- A good agreement can be seen for the Mach number distribution, although a slightly higher Mach number is seen for the steady-state simulation at the stator-rotor interface. This also explains the difference in static pressure at this location.

- As also shown in Table 6.6, the entropy rise in the stator is comparable due to the good agreement in total pressure and total temperature in this region. The entropy generation at the stator-rotor interface is larger in the steady-state simulation due to mixing losses in the mixing plane. Overall the entropy generation in the gap in between the stator and the rotor show to be significant for both the steady-state and the transient simulation.

- The total enthalpy at both the inlet and outlet of the turbine only shows a 0.1% difference between the transient and steady-state simulation. As a result, the difference in estimated turbine efficiency can be assumed to be independent of whether the simulation is of the steady-state or transient type.

During both the steady-state and transient simulation of the Generation 2 turbine, the mass flow rate is lower than the design mass flow rate of $3kg/s$. This can be a reason of the over-expansion in the stator leading to high Mach numbers in this region. As the mass flow rate is limited by the dimensions of the chocked stator throat, the turbine is re-evaluated with an increased stator throat width. This geometry will be referred to as the Generation 3 turbine.

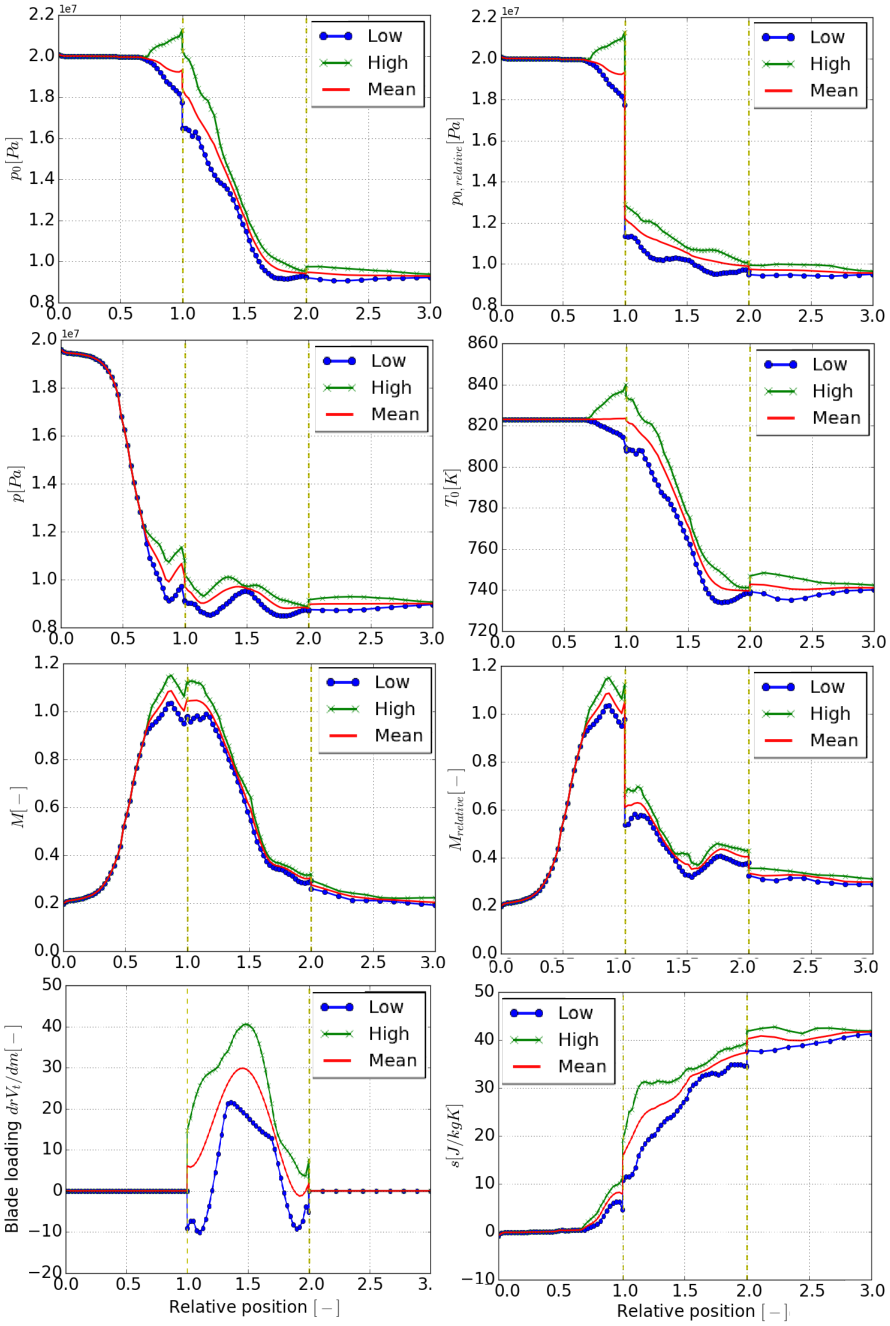

Figure 6.14: Generation 2 turbine Eilmer variation of properties across the turbine for the transient simulation.

6.3. GENERATION 3 TURBINE EVALUATION

The Generation 3 turbine uses the same rotor as the Generation 2 turbine. The stator throat is increased to have the desired mass flow rate of $3kg/s$. The blade walls of the stator and the rotor as well as the hub and shroud geometry of the rotor are set as adiabatic walls. First, the aerodynamic simulation of the full turbine is shown in Section 6.3.1. This is followed by the mechanical stress evaluation in Section 6.3.2. Next, in Section 6.3.3 the aerodynamic results are compared with a reference turbine from literature. The off-design performance is evaluated in Section 6.3.4. Finally, a summary of the Generation 3 turbine concept is given in Section 6.3.5. The main conclusions of Section 6.3 can be summarised as follows:

- As a result of the reduced over-expansion, the losses in the stator channel and in the stator-rotor interspace are reduced compared to the Generation 2 turbine. This results in an efficiency of 73.7%, which

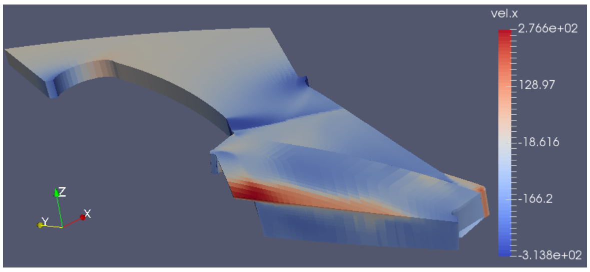

Figure 6.15: Generation 2 turbine Eilmer X-velocity solution flow field.

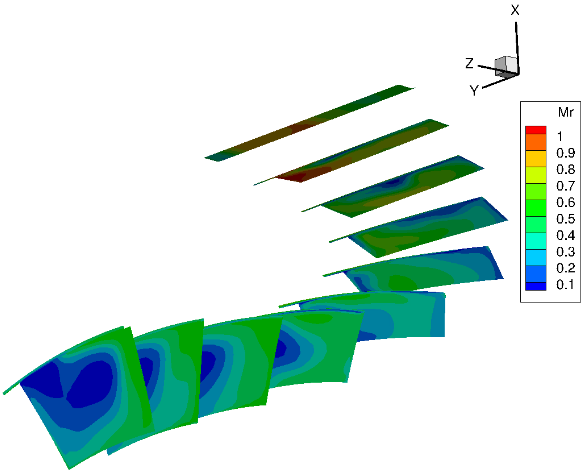

Figure 6.16: Generation 2 turbine Eilmer relative Mach number solution flow field from the rotor inlet at the top to the rotor outlet at the bottom.

is close to the design value from TOPGEN of 73%.

- As a result of the degree of reaction of 0.09, the axial load is $5.0 kN$. This can be reduced by increasing the degree of reaction or by increasing the rotational speed.
- The stresses in the rotor wheel are below the yield limit of the material, also in case of a 20% overspeed. The difference in maximum Von Mises stress when neglecting the pressure loading on the turbine is less than 1%, indicating that the centrifugal loads dominate the stress. Due to the small difference in strain between no-loading and full-loading, the turbine is unlikely to fail as a result of high cycle fatigue.
- A comparison of the results with a turbine from literature shows that the largest difference in losses are in the rotor of the Generation 3 turbine concept. This is expected to be a result of additional tip clearance losses due to the relatively larger tip gap, a larger hydraulic diameter and higher velocities in the rotor channel.
- The expansion in the stator decreases with increasing rotational speed, leading to a higher degree of reaction, which affects the axial load. When increasing or decreasing the rotational speed with 20% to simulate off-design performance, efficiencies above 70% can still be achieved.

6.3.1. AERODYNAMIC FULL TURBINE EVALUATION

The boundary layer mesh of the Generation 3 turbine results in a $y+$ value in the order of 1 to 5 in the turbine. The main results are summarised in Table 6.7. The same SU2 gas parameters and simulation parameters are used as for the Generation 2 turbine and are summarised in Tables B.1 and B.2. The variations of properties across the turbine for the Generation 3 turbine can be seen in Figure 6.17. The convergence history can be found in Figure B.20.

When comparing the variation of properties across the Generation 3 turbine and the Generation 2 turbine, it can be noticed that the over-acceleration in the stator is much reduced as the peak Mach number is lower. This also becomes evident when looking at the Mach number distribution in the stator as seen in Figure 6.18. The positive blade loading at both the start and end of the rotor helps reducing the entropy generation in these regions. As a result, the total pressure losses and entropy generation in the stator are reduced as seen in Table 6.7. Due to viscous effects, additional losses are found in the rotor channel. The pressure at the inlet of the rotor is increased to approximately $10 MPa$, which results in a degree of reaction of 0.09 with a total-to-static efficiency of 74%. Similar as for the Generation 2 turbine, the difference between the degree of reaction of the CFD analysis and TOPGEN is due to the larger design stator outlet Mach number.

The jet-speed ratio ν, defined as the ratio of the blade speed at the rotor inlet and the flow speed at the stator outlet, is for the Generation 3 turbine pushed towards lower values for two reasons. The first reason is

Table 6.7: Generation 3 turbine main results.

Parameter	Value CFD Generation 3	Value CFD Generation 2	Value TOPGEN
η_{ts} [%]	73.7	69.5	73
η_{ts} reduction stator [%]	4.6	5.2	Unknown
η_{ts} reduction stator-rotor interspace [%]	1.9	6.8	Unknown
η_{ts} reduction rotor [%]	18.7	15.9	Unknown
Degree of reaction [−]	0.09	0.05	0.24

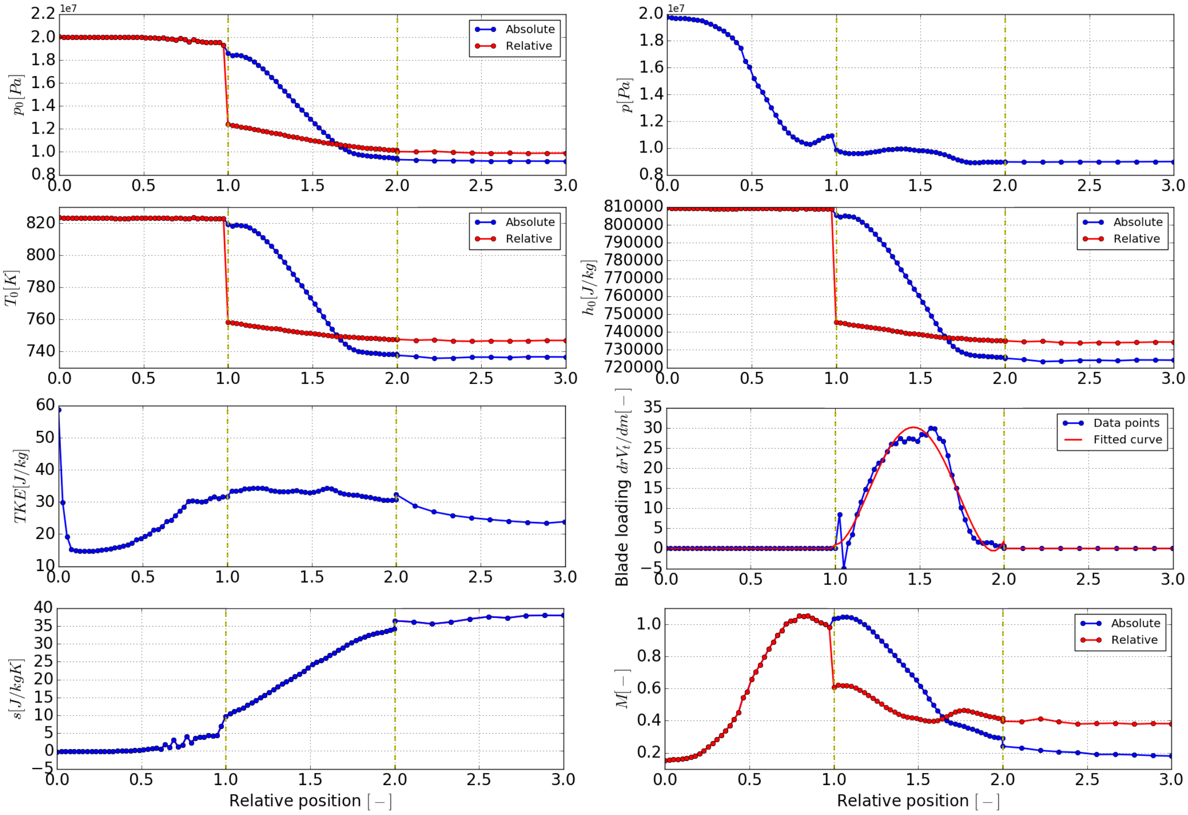

Figure 6.17: Generation 3 turbine variation of properties across the turbine.

the limited rotational speed of $50krpm$, which restricts the design to lower specific speeds than desired as identified in Chapter 4. The second reason is the low degree of reaction, which requires high flow velocities at the stator outlet in order to have a large pressure drop across the stator. The Generation 3 turbine has a jet-speed ratio of 0.53, which is calculated using the absolute flow velocity at the stator outlet from the SU2 analysis. Using the definition of the specific speed in SI units from Rohlik [9], the specific speed of the turbine is equal to $0.175\frac{rad\cdot m^{3/2}\cdot kg^{3/4}}{s^{3/2}\cdot J^{3/4}}$. For calculating this specific speed, for the volumetric flow rate the average density between the rotor inlet and outlet from the SU2 simulation is used. The isentropic specific work is calculated using the expansion ratio of the turbine [72]. The jet-speed ratio of 0.53 is below the suggested value by Rohlik [9] given the specific speed. This paradigm shift to a lower jet-speed ratio is also a result of the non-zero rotor inlet blade angle, which requires a lower rotational speed to have the flow aligned with the blade at the rotor inlet. The effect of varying the jet-speed ratio will be evaluated in Section 6.3.4.

6.3.2. MECHANICAL STRESS EVALUATION

The material of the blade is Alloy 718 and the strength properties of the material are obtained from Aerospace Specification Metals.[1] Alloy 718 is a common material for turbine design and has good strength properties up

---

[1] http://asm.matweb.com/search/SpecificMaterial.asp?bassnum=NINC34

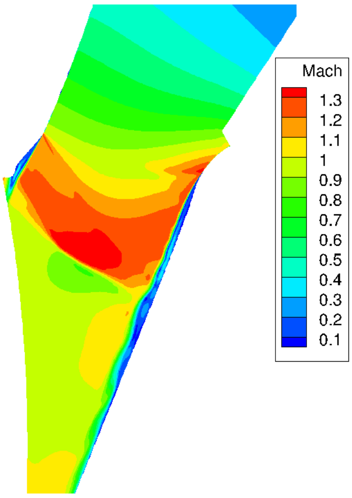

Figure 6.18: Generation 3 turbine Mach number distribution in the stator.

to 700°C. The strength properties at elevated temperatures are used from the aforementioned database and are summarised in Table 6.8.

Table 6.8: Mechanical design material properties.

Parameter	Material limit
Ultimate tensile strength $[MPa]$	1100
Yield strength $[MPa]$	980

The shape of the hub and blades of the turbine are based on the aerodynamic mesh of the Generation 2 and Generation 3 turbines as discussed in Sections 6.2 and 6.3.1. For clarity, Figure 6.19 is shown again. The geometrical dimensions of the back face and shaft as shown in Figure 6.19 are defined in consultation with the shaft, seal and bearing team. These dimensions will be referred to as the nominal dimensions and are summarised in Table 6.9. It should be noted that the outer radius of the shaft has been increased compared to the value used during the preliminary design. This is a result of design decisions made at a later stage in the design process for other components in the cycle. Consequently, this will have an effect on the axial load of the turbine. The length of the shaft and the outer radius of the shaft are largely influenced by the amount of space required for installing the seal, bearing and cooling system. The inner radius of the shaft is set such that an M16 shaft can fit through the centre of the turbine, used to provide a clamping force to the system as will be discussed later. $R_{connection}$ is the radius of the fillet connecting the shaft and the turbine. Referring to Figure 6.19, edge 1 will be subjected to an atmospheric pressure, edges 2, 3 and 4 to the rotor inlet pressure and edges 5 and 6 to the rotor outlet pressure. Moreover, a constraint is placed on edge 1 during the mechanical simulation, allowing movement of this edge only in the radial direction.

Table 6.9: Mechanical design nominal dimensions.

Parameter	Value
L_{shaft} $[mm]$	50
$R_{inner,shaft}$ $[mm]$	9
$R_{outer,shaft}$ $[mm]$	16.5
$t_{backface}$ $[mm]$	5
$R_{connection}$ $[mm]$	8

The nominal case rotates at $50krpm$ and uses the pressure data from the SU2 simulation of the Generation 3 turbine as explained in Section 6.3.1. The resulting Von Mises stress is visualised in Figure 6.20 and shows a peak Von Mises stress of approximately $221MPa$, which is below the material limits. Looking at the back of the rotor shows that the stresses are increasing towards the centre of the rotor, because the material at a larger radius will induce a stress in the lower radius regions. Consequently, the peak Von Mises stress can

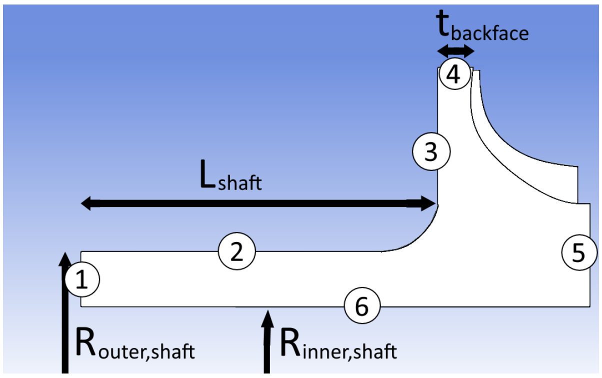

Figure 6.19: Side view of the mechanical model including edge labels.

be found at the inner radius of the shaft near the connection of the shaft and the rotor. The lowest stresses are found at the outer radius of the shaft at a distance from the connection of the shaft and the rotor, which is subjected to lower stresses than the material near the leading edge of the rotor blade because of the reduced surface speed as a result of the smaller radius.

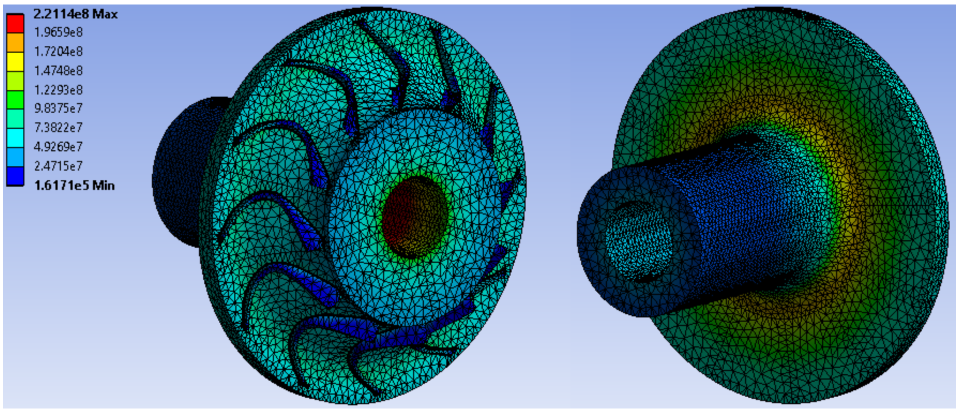

Figure 6.20: Von Mises stress in the nominal mechanical simulation.

Also the effect of changing the geometrical parameters and operating conditions on the stresses experienced by the turbine is evaluated. These results are summarised in Table 6.10. As identified in the literature review in Chapter 2, the turbine should be designed for a rotational speed that is 20% larger than the design operating speed. An increase in rotational speed will result in a four times larger increase in peak Von Mises stress. Increasing the outer radius of the shaft has most effect when the outer radius of the shaft is small. As the peak Von Mises stress is found near the inner radius of the shaft at the connection of the shaft and the rotor, decreasing the length of the shaft L_{shaft} showed to have no effect on the peak Von Mises stress. Increasing the thickness of the back face of the rotor $t_{backface}$ shows a linear increase in peak Von Mises stress as the amount of material subjected to centrifugal forces is increased. Decreasing the radius of the connection between the rotor and the shaft $R_{connection}$ increases the maximum stress. A larger radius will help distributing and transferring the centrifugal forces to the shaft. From the 3D model it can be seen that for the reduced radius at the connection the peak Von Mises stress at the back of the rotor near the connection is approaching the overall peak Von Mises stress as shown in Figure 6.22. From this it can be concluded that this radius should not be reduced to less than $4mm$, as this will result in high stress concentrations at the back of the rotor. Finally, it was observed that when removing the pressure forces from the simulation, thereby only taking into account the centrifugal loads in the system, the difference in maximum Von Mises stress is only 1%. Due to the low reaction of the turbine the centrifugal loads are dominating the stresses. From this it can be concluded that for a low reaction radial inflow sCO_2 turbine, only taking into account the centrifugal forces for the mechanical design will give a good approximation of the actual stresses seen during operation. As the aerodynamic results of the SU2 simulation and Eilmer4 simulation are in good agreement as seen in Section

6.2, the transient effects of a low reaction turbine are not considered to have an impact on the mechanical design as the stress due to the pressure loading is below 1% of the total stress.

Table 6.10: Effect of varying conditions on mechanical design.

Test case (difference with nominal case)	Maximum Von Mises stress [MPa] (difference with nominal case)
Nominal (-)	221 (-)
$\omega = 55krpm$ (+10%)	268 (+21%)
$\omega = 60krpm$ (+20%)	319 (+44%)
$R_{outer,shaft} = 20mm$(+21%)	207 (-6%)
$R_{outer,shaft} = 25mm$ (+52%)	202 (-9%)
$L_{shaft} = 40mm$ (-20%)	221 (0%)
$L_{shaft} = 30mm$ (-40%)	221 (0%)
$t_{backface} = 6.25mm$ (+25%)	237 (+7%)
$t_{backface} = 7.5mm$ (+50%)	250 (+13%)
$R_{connection} = 6mm$ (-25%)	227 (+3%)
$R_{connection} = 4mm$ (-50%)	235 (+6%)

A study is done on the effect of the clamping force on the stresses in the rotor. This clamping force is applied to the face at the rotor outlet, indicated by edge 5 in Figure 6.19, and is used to keep the rotor in place during operation and during extreme events. To determine the clamping force, a worst-case scenario analysis is done. A 12MPa flow at the inlet is assumed, which is higher than the design inlet pressure. To be conservative, the pressure at the outlet of the turbine in case of a turbine failure is prescribed as 0MPa, which is of course physically not existent. This pressure difference creates a force which has to be counteracted by the clamping force to keep the turbine in place. Moreover, a safety factor of 5 will be applied to the clamping force. For the first case, the inlet pressure is assumed to act on the entire back face of the turbine, thereby neglecting the area of the shaft which is in reality subjected to an atmospheric back pressure. This results, after taking into account the safety factor, in a clamping force of 316kN. The second case is similar to the first case, but taking into account the area of the shaft which is subjected to an atmospheric back pressure. This reduces the required clamping force to 265kN. Also the effect of removing the safety factor to the clamping force is evaluated, giving a clamping force of 53kN. Finally, to get a better spread of the data also a clamping force halfway in between 53kN and 265kN (159kN) is taken to evaluate the stresses. The results of this simulation are summarised in Figure 6.21. In Figure 6.21, $Peak$ refers to the peak Von Mises stress seen in the system and $Peakhub$ refers to the peak Von Mises stress seen at the inner surface of the shaft, which was identified to be the location of the peak Von Mises stress when no clamping force is applied. Also the yield stress of Table 6.8 is shown in Figure 6.21.

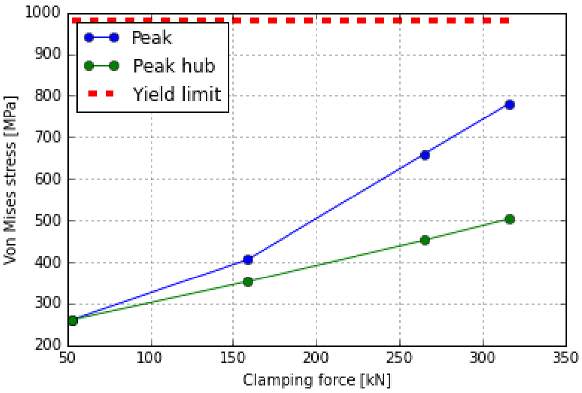

Figure 6.21: Clamping force versus Von Mises stress.

From Figure 6.21 it can be concluded that the peak stress increases with increasing clamping force. When using a clamping force of 53kN, the peak Von Mises stress is located at the inner surface of the shaft as also seen in the previously mentioned analyses. When increasing the clamping force to 159kN the peak Von Mises stress is found at the rotor-shaft connection, but is still close to the maximum Von Mises stress found at the inner surface of the shaft. When increasing the clamping force to 265kN and 316kN the shaft-rotor connection clearly becomes the most critical location in the system regarding the maximum experienced stress during operation, similar as seen in Figure 6.22. The stress concentration at the rotor-shaft connection when a clamping force of 265kN is applied can be seen in Figure 6.23. This stress concentration can be reduced by increasing $R_{connection}$ or by increasing the angle between the shaft and the rotor. Overall, the stress at all clamping loads is still well below the yield limit of the material. It can therefore be concluded that the clamping force of $265kN$ can be applied to the system without any further implications.

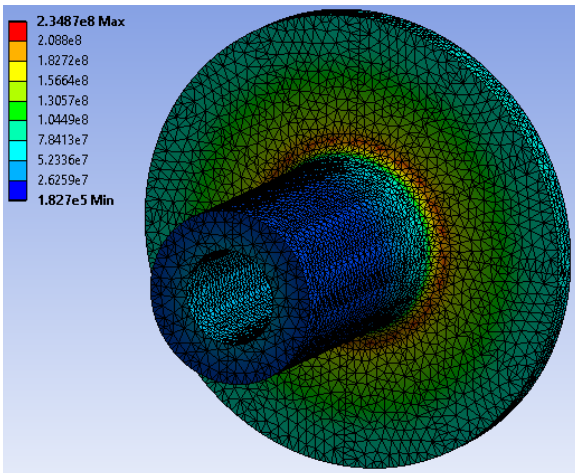

Figure 6.22: Von Mises stress in the mechanical simulation with $R_{connection} = 4mm$.

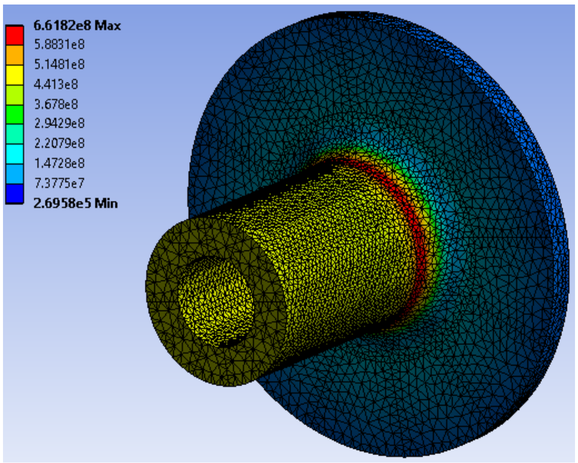

Figure 6.23: Von Mises stress in the mechanical simulation with a clamping load of $265kN$.

The axial load according to the mechanical evaluation which is transferred to the thrust bearings is equal to $5.0kN$. Looking back at Figure 6.19, this load is obtained by summing the pressure loads acting on edge 1, 3, 5 and the hub surface of the rotor passage. Also the pressure load on the inner shaft through the centre is considered, which has to be supported by the thrust bearing as well. The difference between the estimated load in the preliminary design of $2.9kN$ and the axial load from the mechanical design is mainly a result of the change in shaft design compared to the shaft used during the preliminary design. As the shaft is located at the high pressure side of the turbine, increasing the degree of reaction of the turbine can reduce the magnitude of the axial load. When taking the turbine dimensions, rotor inlet pressure and rotor outlet pressure from the aerodynamic design and assuming the axial load to vary linearly in the turbine channel, the axial load estimation from the 1D design would predict an axial load of $5.5kN$. Based on this, it can be concluded that for a low reaction sCO_2 turbine the axial load can be well estimated using the rotor dimensions and rotor inlet and outlet pressure, thereby eliminating the need of doing a detailed mechanical design for obtaining the axial load.

With a rotor blade passing 1 million stator blades per minute during operating, the flow field variation during the transient simulation as seen in Figure 6.13 will subject the rotor to High Cycle Fatigue (HCF). Therefore, it is important to evaluate the HCF life of the rotor. This is done by calculating the elastic strain difference between the nominal case and the case with no loading. This is an extremely conservative approach, as this would assume the blade loading due to the pressure of the fluid to constantly oscillate between no-loading and full-loading. The difference in strain between no-loading and full-loading is less than 0.01% as can be seen in Figure 6.24. Research of Korth [96] shows that the life of Alloy 718 at $538°C$, which is close to the turbine inlet temperature, approaches infinite when the strain range is less than 0.3%. From the observations of the mechanical design, it can be concluded that the HCF strength of the rotor is well within the limits as a result of the low blade loading and the rotor is therefore unlikely to fail as a result of HCF.

6.3.3. Comparison of performance to comparable design from literature

Wheeler and Ong [25] describe the breakdown of the losses in a radial inflow turbine. No detailed analyses have been done for the Generation 3 turbine allowing to quantify the loss contributions originating from the different sources as described by Wheeler and Ong. Therefore, only a comparison will be done on the overall losses in the stator, in the rotor and at the exit of the turbine. A comparison between the breakdown of the entropy generation in the Generation 3 turbine design with the losses of the Rotor 1 design as described by Wheeler and Ong can be seen in Table 6.11, which also shows the breakdown of the losses of the NASA stage [97] used as a comparison in the research of Wheeler and Ong. This is also visualised in Figure 6.25. The Rotor 1 design is a transonic ORC turbine with a stator exit Mach number of approximately 1.4, whereas the NASA stage is a conventional gas turbine of the radial inflow architecture. For the Generation 3 turbine, the

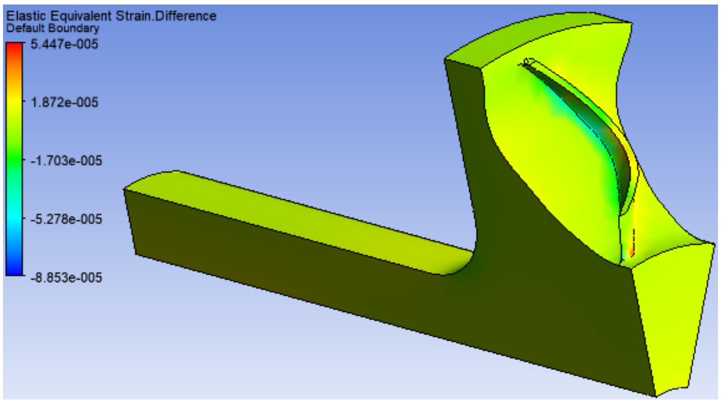

Figure 6.24: Elastic equivalent strain difference between the analysis with pressure loads and the analysis without pressure loads.

reduction in total-to-static efficiency due to the exit Kinetic Energy (KE) is taken as the difference between the total-to-total efficiency and total-to-static efficiency [72]. The losses in the stator and in the rotor are taken as the relative contribution to the total entropy generation in the turbine as seen in Figure 6.17.

Table 6.11: Losses breakdown comparison.

	Generation 3 turbine -$\Delta\eta_{ts}$	Rotor 1 -$\Delta\eta_{ts}$ [25]	NASA stage -$\Delta\eta_{ts}$ [25]
Stator	6.5%	7.5%	6.1%
Rotor	18.7%	5.8%	10.3%
Exit	1.1%	3.9%	5.4%

It can be seen that the reduction in total-to-static efficiency due to losses in the stator is lower for the Generation 3 turbine compared to Rotor 1. The first possible reason for this is that the hub and shroud wall of the stator are assumed to be free-slip walls during the SU2 simulation, which reduces the viscous effects. Wheeler and Ong [25] attribute the higher stator losses of the Rotor 1 design compared to the NASA stage to the higher stator outlet Mach number, leading to larger contributions of the boundary layer and shocks to the losses. The stator outlet Mach number of the Generation 3 turbine is only slightly supersonic as can be seen in Figure 6.17. This is in between the stator outlet Mach number of the Rotor 1 design of 1.4 and the NASA stage of 0.8. Following the same reasoning as in the research of Wheeler and Ong, this explains the stator losses to be lower than in the Rotor 1 design and higher than in the NASA stage.

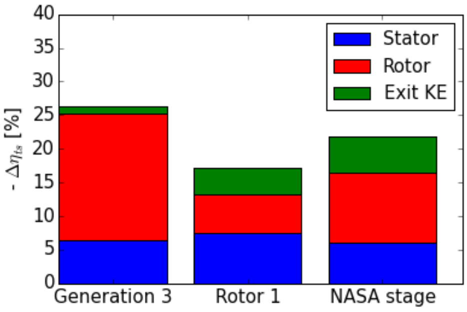

Figure 6.25: Losses breakdown comparison with the Rotor 1 and NASA stage from Wheeler and Ong [25].

On the contrary, by looking at Figure 6.25 it can be noticed that the losses in the rotor are much larger in the final design compared to the Rotor 1 design. As identified before, the tip clearance losses can be a significant contributor to the total losses. Since the Rotor 1 design is shrouded, there are no tip leakage flows and therefore no tip leakage losses. Consequently, the losses in the rotor will be larger for the Generation 3 turbine compared to the Rotor 1 design. As the turbine dimensions of the Generation 3 turbine are smaller compared to the NASA stage, secondary effects are increased as already identified in the literature review in Chapter 2. Similar as in the Rotor 1 design, flow separation is seen on the suction side of the rotor blade, caused by the turning of the flow. This flow separation results in a vortex further downstream. The separation contributes to the entropy generation and thereby the losses in the rotor. The entropy generation in this separated region and in the vortex can be seen in Figure 6.26, where the flow fields closer to the rotor inlet show the separation region and the flow field closer to the rotor outlet shows the vortex as regions with a high entropy. The vortex is aggravated by the tip clearance flow in the Generation 3 turbine, which is absent for the Rotor 1 design. Also noted by Wheeler and Ong [25] is the low momentum fluid at the suction surface having a radial component as a result of the fluid path bending from the radial to the axial direction. This is also observed in the Generation 3 turbine, as can be seen by the high entropy near the shroud of the last flow field of Figure 6.26, which is close to the outlet of the turbine, with the shroud at the right side of the cross section.

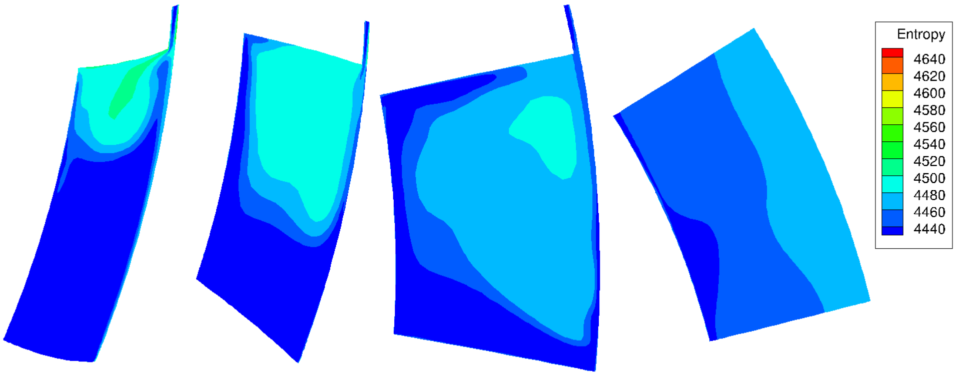

Figure 6.26: Generation 3 turbine entropy variation from the rotor inlet (left) to the outlet (right).

Two possible reasons for the larger losses in the rotor channel compared to the NASA stage are the reduced blade heights and the higher meridional velocity. The small blade height, apart from aggravating tip clearance effects, results in a small hydraulic diameter. Taking the example of a square, when increasing the length of the sides by a factor 2, the ratio between the circumferential length and the area of the square decreases by a factor 2. This means the viscous effects will have a larger influence on the Generation 3 turbine with the smaller hydraulic diameter compared to the NASA stage. Moreover, the tip clearance of the NASA stage is with 3.7% and 1.2% at the rotor inlet and outlet respectively [97] lower than the Generation 3 turbine. The relative Mach at the inlet of the NASA rotor is 0.26, which is significantly lower than the relative Mach number of 0.6 as seen at in the Generation 3 turbine. The higher meridional velocity will also negatively affect the viscous losses in the rotor channel.

The absolute flow velocity at the turbine exit of the Generation 3 turbine is approximately $75 m/s$. Because of this low exit velocity compared to the Rotor 1 design, the contribution of the exit KE to the losses is reduced.

Based on these observations, it can be concluded that the rotor is identified as the region where future improvement of the Generation 3 turbine can be made. One of the options would be to use a shrouded rotor design, which diminishes the tip clearance effect of the small blades.

6.3.4. OFF-DESIGN PERFORMANCE

To investigate the effect of the jet-speed ratio on the turbine efficiency, the rotational speed of the turbine is varied from $30 krpm$ to $60 krpm$. The results are summarised in Table 6.12, where the nominal operating speed of $50 krpm$ is shown in bold. Table 6.12 shows the rotational speed ω, total-to-static efficiency η_{ts}, total-to-total efficiency η_{tt}, jet-speed ratio ν, absolute flow angle at the rotor outlet $\alpha_{rotor,out}$, relative flow angle at the rotor outlet $\beta_{rotor,out}$, relative Mach number at the rotor outlet $M_{relative,rotor,out}$, the pressure at the interface in between the stator and rotor $p_{interface}$ and the axial load on the rotor F_{axial}.

In Table 6.12 the difference between the total-to-total efficiency and the total-to-static efficiency is the loss in kinetic energy at the turbine outlet. Since the axial velocity at the rotor outlet is independent of the rotational speed, the kinetic energy loss is solely a function of the absolute flow angle at the rotor outlet. The kinetic energy loss is minimal when the absolute flow angle at the rotor outlet angle approaches 0, i.e. the swirl is small, which is the case at the nominal design speed. Based on these trends, operating at a slightly higher rotational speed than the nominal speed of $50 krpm$ could reduce the swirl further to improve the total-to-static efficiency.

The relative flow angle at the rotor outlet, the relative Mach number at the rotor outlet and the pressure at the stator-rotor interface are directly related to each other. It should be noted that the mixing plane at the

Table 6.12: Rotational speed variation for the Generation 3 turbine design.

ω [rpm]	η_{ts} [%]	η_{tt} [%]	ν [$-$]	$\alpha_{rotor,out}$ [deg]	$\beta_{rotor,out}$ [deg]	$M_{relative,rotor,out}$ [$-$]	$p_{interface}$ [MPa]	F_{axial} [kN]
30000	60.0	63.5	0.29	60.6	72.7	0.444	9.5	11.2
35000	66.1	69.2	0.34	56.5	72.5	0.449	9.7	11.2
40000	70.6	72.8	0.40	47.3	71.5	0.429	9.9	9.7
45000	71.4	72.7	0.47	28.9	69.7	0.391	10.4	7.9
50000	**73.7**	**74.8**	**0.53**	**8.8**	**68.6**	**0.374**	**10.8**	**5.0**
55000	73.5	74.6	0.61	-19.1	67.2	0.364	11.3	3.8
60000	72.9	74.5	0.70	-36.8	66.3	0.330	11.8	2.2

stator-rotor interface is located close to the trailing edge of the stator. This pressure is not the same as the pressure at the rotor inlet, as the flow will further expand from the stator outlet to the rotor inlet. As a result of the increased Coriolis and viscous forces for larger rotational speeds, the pressure drop across the rotor is increased to counteract these forces, leading to a higher pressure at the interface. Given the variation in flow area in the rotor passage as shown in Figure B.16, the corresponding lower Mach number at the interface results in a reduced relative Mach number at the rotor outlet. Because of the fixed axial Mach number at the rotor outlet as explained before, a larger relative Mach number at the rotor outlet results in an increased relative flow angle at this location.

The variation in entropy, blade loading, pressure and Mach number along the turbine when rotating at $30krpm$ and $60krpm$ can be seen in Figures 6.27 and 6.28 respectively. First of all, it can be noted that the peak Mach number in the stator channel reduces for increased rotational speeds as already concluded from Table 6.12. As a result of the reduced Mach number, the entropy generation in the stator channel is reduced. On the contrary, a more pronounced increase in entropy close to the rotor inlet can be observed for the $60krpm$ rotational speed. This is an effect of the change in blade loading caused by a change in the relative flow angle at the rotor inlet. It can be seen that for the $60krpm$ case, the first part of the rotor has a negative blade loading, whereas this part of the blade is positively loaded for the $30krpm$ case. As a result of the negative blade loading, the total temperature increases in this region, leading to a large increase in entropy. By looking at the pressure and relative Mach number distribution in the rotor, it can be seen that the expansion process is more gradual at the higher rotational speed. Consequently, the entropy generation in the rotor channel is much reduced, leading to an improved overall efficiency.

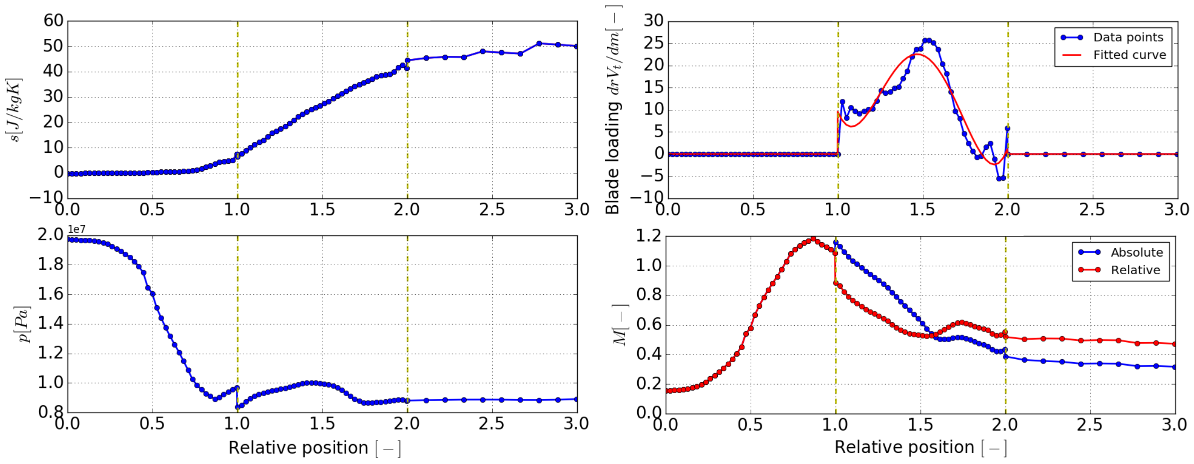

Figure 6.27: Generation 3 turbine $\omega = 30krpm$ variation of properties across the turbine.

The total-to-static efficiency of the off-design rotational speeds as seen in Table 6.12 can be increased by adjusting the blade angle at the rotor trailing edge. It can be noted that the jet-speed ratio giving the highest efficiency is below the suggested value by Rohlik [9], although the reduction in total-to-total efficiency is small when increasing the jet-speed ratio to 0.7. Overall, it can be seen that the turbine has an efficiency above 70% when operating in between 80% and 120% of the nominal rotational speed of $50krpm$. As mentioned before,

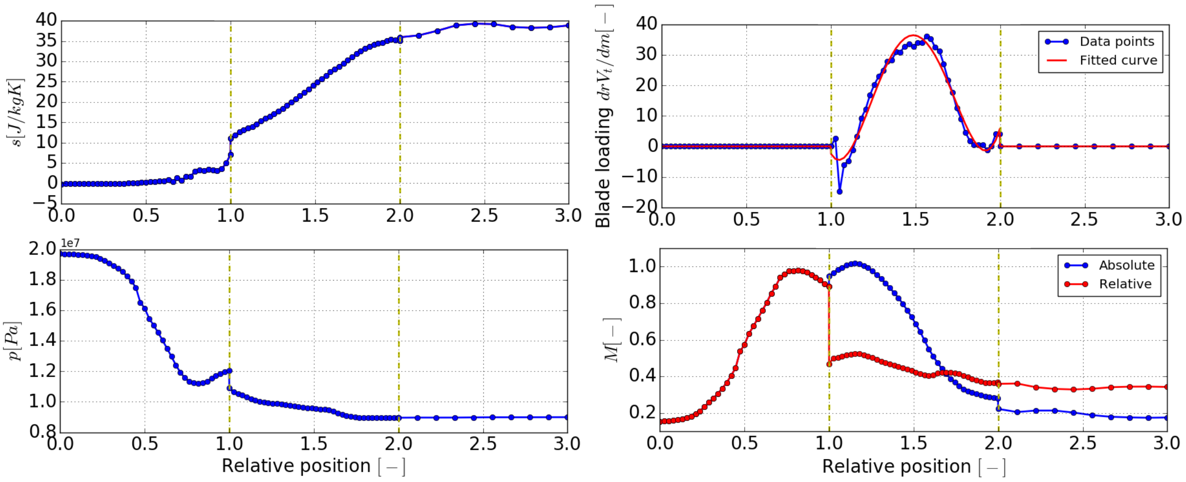

Figure 6.28: Generation 3 turbine $\omega = 60krpm$ variation of properties across the turbine.

at the nominal rotational speed the axial load is acting in the direction of the thrust bearing. Increasing the rotational speed to $60krpm$ increases the degree of reaction and consequently reduces the axial load. The variation in pressure at the stator-rotor interface for different rotational speeds, which is also important during start-up, should be taken into account for the bearing design.

6.3.5. TURBINE CONCEPT SUMMARY

For clarity, the main geometric parameters of the Generation 3 turbine are summarised in Table 6.13, which matches the values seen for the Generation 2 turbine in Section 6.2. The operating conditions and performance of the Generation 3 turbine are summarised in Table 6.14. The radial inflow turbine concept operates at the maximum allowable operating speed of $50krpm$ as defined in Section 4.1. The small turbine dimensions as a result of the low volumetric flow rate in combination with the limited rotational speed require a non-zero blade angle at the rotor leading edge. The desire of increasing the diameter at the rotor inlet in order to increase the rotor tip speed, decreases the blade height at the rotor inlet to the minimum value of $0.9mm$ as set in Section 4.1. The low degree of reaction of 0.09 results in an axial load of only $5.0kN$ into the thrust bearing. As this load is acting in the direction of the thrust bearing, a 1D estimation shows increasing the degree of reaction to 0.26 could reduce the magnitude of this load even more. The effect of the pressure loads on the maximum Von Mises stress is less than 1%. Similar efficiencies can be maintained when operating at off-design conditions with a rotational speed increase or decrease of 20%. Overall, a total-to-static efficiency of 74% can be achieved for the Generation 3 turbine.

Table 6.13: Generation 3 turbine geometric parameters summary.

Stator		Rotor	
Parameter	Value	Parameter	Value
N_{stator} $[-]$	20	N_{rotor} $[-]$	20
$R_{stator,LE}$ $[mm]$	49.1	$R_{rotor,LE}$ $[mm]$	41.3
$R_{stator,TE}$ $[mm]$	43	$R_{rotor,TE,mean}$ $[mm]$	24.6
$R_{stator,throat}$ $[mm]$	46	$h_{rotor,in}$ $[mm]$	0.9
h_{stator} $[mm]$	1	$h_{rotor,out}$ $[mm]$	4.08
α_{stator} $[deg]$	68	$h_{rotor,tcl,in}$ $[mm]$	0.1
$M_{stator,out}$ $[-]$	1.12	$R_{rotor,tcl,out}$ $[mm]$	0.144
		z_{rotor} $[mm]$	13.4
		$\beta_{rotor,LE}$ $[deg]$	50.6
		$\beta_{rotor,TE}$ $[deg]$	59
		$t_{rotor,root}$ $[mm]$	1.6
		$t_{rotor,tip}$ $[mm]$	1.2
		ϕ_{rotor} $[deg]$	11

Table 6.14: Generation 3 turbine operating conditions and performance summary.

Parameter	Value
Mass flow rate [kg/s]	3.0
Rotational speed [rpm]	50000
Inlet total pressure [Mpa]	20
Inlet total temperature [K]	823
Outlet pressure [MPa]	9
Total-to-static efficiency [%]	73.7
Total-to-total efficiency [%]	74.8
Degree of reaction	0.09
Degree of admission	1.0
Jet-speed ratio	0.53
Axial load [kN]	5.0
Maximum Von Mises stress without clamping load [MPa]	221
Maximum Von Mises stress with clamping load [MPa]	662

7

CONCLUSIONS AND RECOMMENDATIONS

In this Chapter the main conclusions and recommendations of this research are presented. This starts with Section 7.1 where a summary of the main conclusions of the research is given, including a review of the research questions. Next, in Section 7.2 the recommendations for future work will be discussed.

7.1. CONCLUSIONS

The primary objective of this research was to create a workflow for designing turbines using the Eilmer4 software and use this workflow to design a small-scale sCO_2 turbine for CSP applications. As this project is the first application of Eilmer4 for turbomachinery design, there was a need for establishing a workflow and creating tools aiding the user to execute this workflow. The tools that have been developed can automate going from one step to the next in the turbine design process and can be used in any future research following the same method as this research. Whereas previous turbine designs at the University of Queensland used various software tools, the developed methodology of this research helps standardising the turbine design process. The methodology covers going from a 1D design to a 3D transient and steady-state aerodynamic design and a mechanical stress evaluation. From this research, it can be concluded that the tools have been successfully implemented and can be used for future turbine design. Also, Eilmer4 can from now on be used for turbine design.

During the 1D design of the sCO_2 turbine it became evident that the efficiency of the radial outflow turbine is inferior to both the axial turbine and the radial inflow turbine. The low aspect ratio of the blades of the axial turbine as a result of the low mass flow rate requirement is not considered to be a realistic option and the corresponding additional losses that are expected make this option unpractical. When using an axial turbine in combination with partial admission, this aspect ratio can be increased, but the additional complications in turbine design and losses due to blockage of the flow make the radial inflow turbine the preferred turbine architecture for this application. Keeping the axial load down, which is identified as one of the challenges in sCO_2 turbine design according to previous research, a low degree of reaction turbine is required in order for the shaft to be placed at the low pressure side of the turbine. It was found that a turbine efficiency of 89% can be achieved, although this estimation of zTurbo neglects tip clearance losses, which are found to be significant for small-scale turbomachinery.

This became evident during the CFD simulation, where the Generation 1 turbine has an efficiency of only 65%. A 1D simulation using the TOPGEN code showed that, for the same head coefficient and flow coefficient, a tip clearance loss of approximately 10% is expected, which is based on a NASA correlation for small-scale radial inflow turbines. Consequently, the turbine geometric parameters change for the TOPGEN design when taking into account this reduced efficiency compared to the zTurbo design. The overestimation of the turbine efficiency when using zTurbo will result in unaccounted losses during the CFD simulation. The TOPGEN design has an estimated efficiency of 72.5% with a degree of reaction of 0.24, which requires the shaft to be placed at the high pressure side of the turbine in order to compensate for the increased pressure drop across the rotor to keep the axial force low.

The steady-state SU2 simulation and the transient Eilmer4 simulation show differences across the turbine path, but the overall properties at the inlet and outlet are in good agreement, including the estimated turbine efficiency of the Generation 2 turbine. Based on this, it can be concluded that a steady-state simulation can give a good approximation of the turbine performance, although comparing multiple turbine designs would be required to test the validity of this conclusion for the design of small-scale low reaction sCO_2 turbomachinery in general. From the results of the steady-state SU2 simulation of the Generation 3 turbine, it can be concluded that a total-to-static efficiency of 74% can be achieved with a degree of reaction of only 0.09 as a result of the transonic flow at the stator outlet. A negative blade loading showed to be a source of entropy generation. Whereas changes in rotational speed have a small impact on the turbine efficiency, this is shown to have a large influence on the pressure at the rotor inlet and therefore blade load and axial load. As no sudden peaks in entropy generation are seen across the rotor channel, it can be concluded that the high curvature of a low reaction radial inflow turbine does not seem to have a detrimental effect on the turbine performance as was suggested in dated literature. Based on this it can be concluded that the low degree of reaction radial inflow turbine is identified as an area of the design space which can be used for managing the thrust load.

From the results of the mechanical stress evaluation, it could be noted that the Generation 3 turbine has sufficient strength to operate at design conditions and during overspeed. It can be concluded that the centrifugal forces dominate the stresses in a low reaction radial inflow sCO_2 turbine, as the influence on stresses due to pressure loading is less than 1%. As a result of the good agreement between steady-state and transient simulation in combination with the low stresses from the blade loading, it can be concluded that the transient effects will not have an influence on the mechanical design of the turbine. Moreover, it is found that the rotational speed has a large influence on the stresses in the turbine. Also, reducing the radius of the connection between the rotor and the shaft below a minimum value can result in a rapid increase in maximum stress. Finally it was seen that the axial load of $5.0 kN$ can be estimated reasonably well by using a simple 1D estimation based on the turbine dimensions and results from the aerodynamic design. This would eliminate the need of doing a detailed mechanical stress evaluation for obtaining the axial loads of the turbine.

The results of this research can be related back to the research questions as introduced in Chapter 1:

- **What are the implications of the requirements set by ASTRI to the turbine design?** The requirements set by ASTRI to the turbine design limit the specific speed of the turbine concept. This is a direct result of the small power output and the limited rotational speed. Consequently, CFD simulations suggest the achievable efficiency reduces compared to reference turbines. Moreover, the requirement of having a low axial force limits the degree of reaction of the turbine. This pushes the design away from a reaction turbine, which is according to literature reducing the efficiency of the turbine. Whereas setting these limits is not desired from an aerodynamic point of view, limiting the rotational speed and degree of reaction is desirable for the bearing and mechanical design. Moreover, a reduction in axial load as a result of the limited degree of reaction simplifies the seal and thrust bearing as concluded from literature. The challenges in mechanical design as a result of the high fluid loads were identified in literature, but due to the low degree of reaction, the fluid loads do not have a large impact on the mechanical design. As a result of the requirements set by ASTRI, the centrifugal forces and blade loading are limited. Moreover, passage losses and tip clearance losses in the rotor channel are found to be the main contributor to the overall turbine losses in a low reaction radial inflow turbine.

- **What turbine architecture is more suitable for meeting the requirements set by ASTRI?** The sCO_2 turbines found in literature are axial and radial inflow architectures and the potential of using a radial outflow turbine for other highly dense fluids is identified in literature. The large design space exploration during the preliminary design allowed for assessing the performance of the axial turbine, radial inflow turbine and radial outflow turbine. It can be concluded that extremely low aspect ratio blades are found for the axial turbine architecture due to the low mass flow rate requirement. The blade aspect ratio can be increased by reducing the degree of admission, but this is not desirable as this complicates the turbine design and will create additional losses due to blockage of the flow. The estimated efficiency of the radial outflow turbine is inferior to the efficiencies seen for the radial inflow turbine. The radial inflow turbine is showing good estimated efficiencies with acceptable axial loads for full admission turbines. Therefore the radial inflow turbine is considered to be the most suitable turbine architecture for meeting the requirements set by ASTRI and for other small-power sCO_2 applications.

- **What methods can be used to design the different turbine architectures of interest?** The preliminary design tools used are zTurbo and TOPGEN. By using an automated tool, a large design space can be explored using zTurbo. Extending the capability of estimating the axial force to this approach is a necessity in order to give insight into meeting the requirements set by ASTRI. The limitation of zTurbo is that some of the loss models as implemented in zTurbo fail to give an output for certain input parameters. Moreover, neglecting the tip clearance losses when using the Glassman loss model in zTurbo is shown to have a significant effect on the estimated turbine efficiency. For designing a radial inflow turbine, TOPGEN is found to be a suitable tool to estimate the turbine performance when compared to the CFD results. By using the design methodology and the developed tools, a method is established to go from a preliminary design to a transient aerodynamic evaluation using Eilmer4, a steady-state aerodynamic evaluation using SU2 and a mechanical stress evaluation using ANSYS. The difference between estimated turbine efficiencies of the steady-state and the mean of the transient aerodynamic evaluation is small. However, the transient variation of the flow field is found to have an effect on the entropy generation at different rotor positions. Therefore, it can be concluded that evaluating and understanding the transient effects is important to be able to increase the turbine efficiency to higher levels.

- **What is the stator and rotor geometry to achieve the highest performance?** Although no thorough optimisation has been done, it can be concluded that the low axial load requirement pushes the design to a low reaction turbine, thereby requiring transonic stator outlet conditions. Also a deceleration of the flow in the relative reference frame is required in the rotor to compensate for the decrease in rotational speed in order to keep the degree of reaction low. For the exact geometrical parameters and fluid states, the reader is referred to Section 6.3.5.

What is the performance of a supercritical CO_2 turbine meeting the requirements set by the Australian Solar Thermal Research Initiative (ASTRI)? The Generation 3 turbine as designed in this thesis work shows to have a total-to-static efficiency of 74% and results in an axial load of $5.0kN$. According to this research, removing the low rotational speed and axial load requirement could increase the turbine performance at the expense of complicating mechanical, bearing and seal design. The main conclusion is that it is possible to design an sCO_2 turbine with reasonable performance while meeting the low rotational speed and axial load requirements.

7.2. RECOMMENDATIONS

The current study focuses on the design of the turbine, while taking into account the possible implications on the shaft and bearing design. For future research it, is recommended to combine the method and results of this research to a study on shaft and bearing performance to be able to analyse the whole power block including all subsystems. This will give more insight into some of the challenges in sCO_2 turbine design as identified in Chapter 2, like rotordynamics, which is strongly coupled to the turbine design.

Moreover, it is recommended to review the loss models for the radial inflow turbine in zTurbo. Including tip clearance effects and making these loss models more robust is considered to be a necessity for using zTurbo in future small radial inflow turbine designs.

Due to the implementation of the sliding interface in Eilmer4, the turbine design of this research is restricted to an equal number of stator and rotor blades. It is unlikely that optimal turbine efficiency is achieved by using the exact same number of stator and rotor blades. Moreover, from a vibrational and mechanical point of view it is desirable to have an unequal number of stator and rotor blades, as this prevents all rotor blades to pass the wake of the stator at the same time. Therefore, it is recommended to extend the capability of the sliding interface in Eilmer4 to be able to model a different number of stator and rotor blades.

With the current meshing tool, obtaining a smooth variation in cell area is difficult to obtain in certain parts of the mesh due to for example the short supersonic section of the stator. Moreover, the skewness of the cells in certain parts of the mesh is higher than recommended in literature. This is a result of the short supersonic section in the stator compared to the overall stator length, the non-zero rotor inlet blade angle and the meshing around the leading and trailing edge of the rotor. It is therefore recommended to perform a study on improving the aerodynamic meshing tool to enhance the mesh quality in the aforementioned regions.

The computational time of the transient Eilmer4 simulation for well-resolved boundary layers is found to be unacceptably high in the order of weeks to even months due to the small time step required to solve the flow in the smallest cells in the fluid domain. This time step is proportional to the volume of the smallest cell in the mesh. Therefore, it is not only recommended, but also considered to be a necessity for making Eilmer4 suitable to perform a viscous turbine evaluation, to implement wall functions in Eilmer4. By using wall functions, a larger $y+$ value can be used, thereby allowing for a less refined boundary layer and consequently an increased cell size in the boundary layer mesh.

As a large part of the current study is focusing on creating the methodology and tools, future research can focus in more detail on the variation of turbine geometrical parameters and the effect on the turbine performance, as this has only been done to a limited extend. Moreover, it is recommended to do a detailed study on the shape of the stator blade in the supersonic part of the stator as this has been identified as a region where the fluid over-accelerates, thereby leading to extra losses. As the passage and tip clearance losses in the rotor dominate the total turbine losses, it is recommended to have this as the main area of attention in future research to recover performance. A shrouded turbine would be one of the interesting options to evaluate in more detail.

Finally it is also recommended to analyse the turbine during start-up and shut-down in depth before building the turbine to ensure acceptable behaviour during testing of the turbine.

A

PRELIMINARY DESIGN RESULTS

A.1. AXIAL TURBINE

$\dot{m} = 2.5 kg/s$

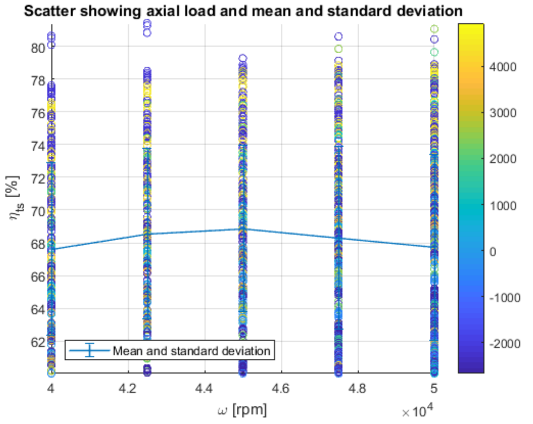
Scatter showing axial load and mean and standard deviation

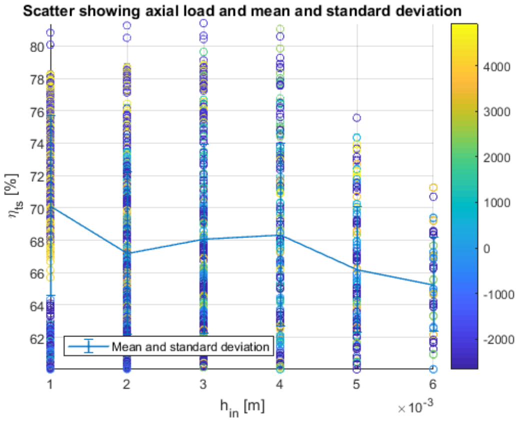
Scatter showing axial load and mean and standard deviation

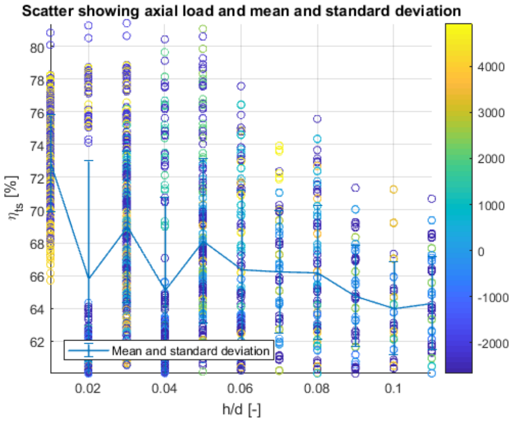
Scatter showing axial load and mean and standard deviation

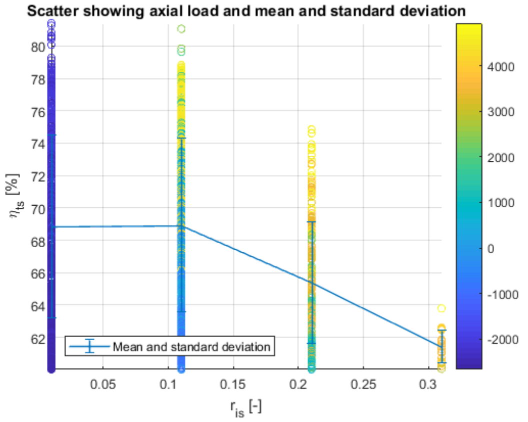
Scatter showing axial load and mean and standard deviation

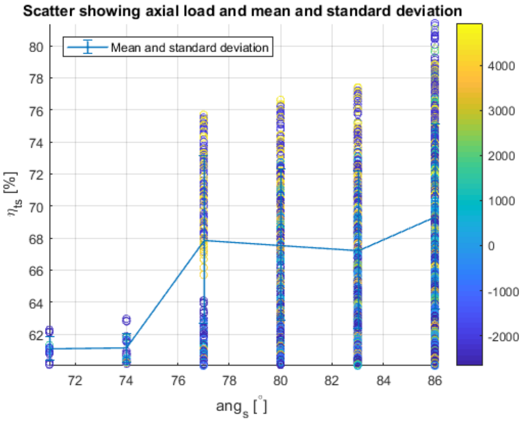
Scatter showing axial load and mean and standard deviation
Mean and standard deviation
80
78
76
74
72
70
68
66
64
62
η_{ts} [%]
72
74
76
78
80
82
84
86
ang$_s$ [°]
4000
3000
2000
1000
0
-1000
-2000

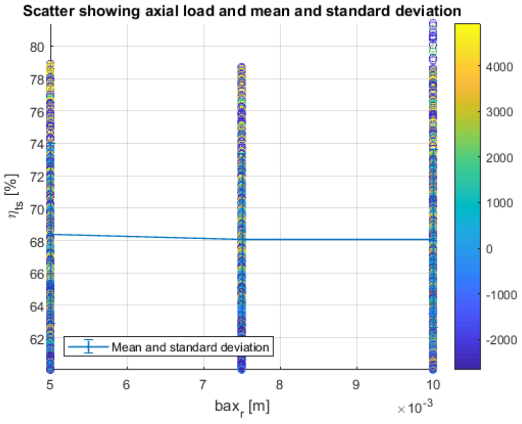
Scatter showing axial load and mean and standard deviation
Mean and standard deviation
80
78
76
74
72
70
68
66
64
62
η_{ts} [%]
5
6
7
8
9
10
$\times 10^{-3}$
bax$_r$ [m]
4000
3000
2000
1000
0
-1000
-2000

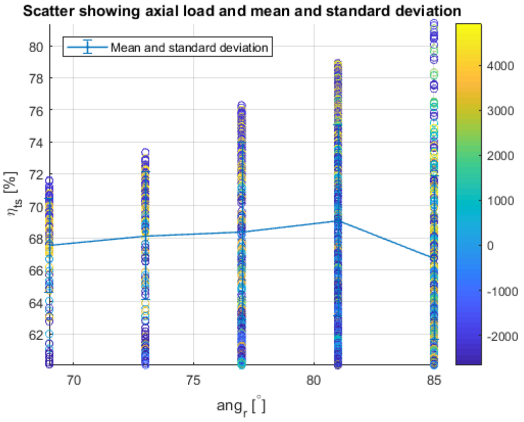
Scatter showing axial load and mean and standard deviation
Mean and standard deviation
80
78
76
74
72
70
68
66
64
62
η_{ts} [%]
70
75
80
85
ang$_r$ [°]
4000
3000
2000
1000
0
-1000
-2000

$\dot{m} = 3kg/s$

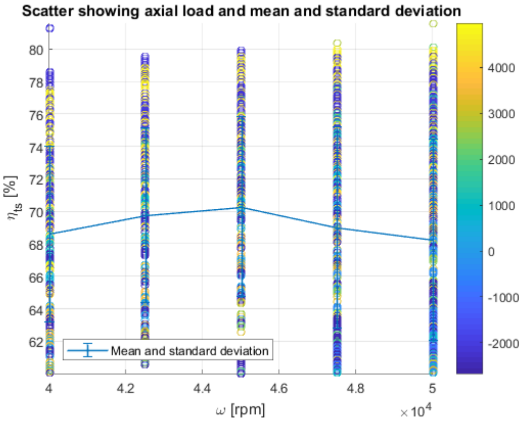
Scatter showing axial load and mean and standard deviation
Mean and standard deviation
80
78
76
74
72
70
68
66
64
62
η_{ts} [%]
4
4.2
4.4
4.6
4.8
5
$\times 10^{4}$
ω [rpm]
4000
3000
2000
1000
0
-1000
-2000

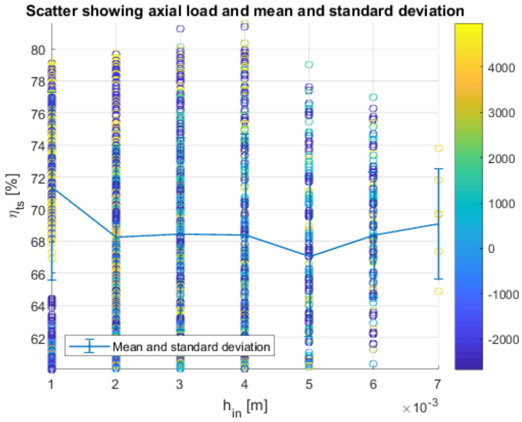
Scatter showing axial load and mean and standard deviation
Mean and standard deviation
80
78
76
74
72
70
68
66
64
62
η_{ts} [%]
1
2
3
4
5
6
7
$\times 10^{-3}$
h$_{in}$ [m]
4000
3000
2000
1000
0
-1000
-2000

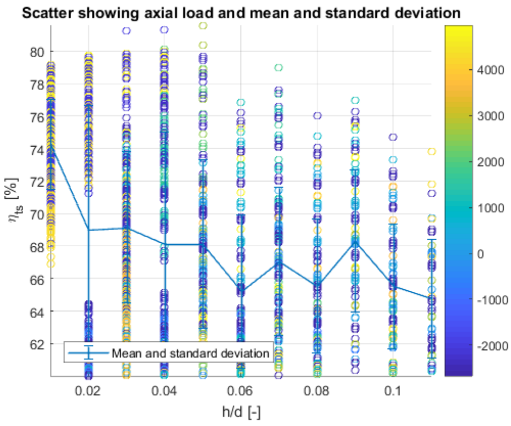
Scatter showing axial load and mean and standard deviation
η_{ts} [%]
80
78
76
74
72
70
68
66
64
62
0.02
0.04
0.06
0.08
0.1
h/d [-]
Mean and standard deviation
4000
3000
2000
1000
0
-1000
-2000

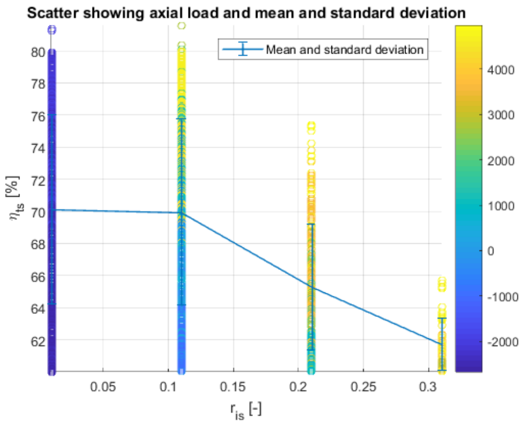
Scatter showing axial load and mean and standard deviation
η_{ts} [%]
80
78
76
74
72
70
68
66
64
62
0.05
0.1
0.15
0.2
0.25
0.3
r_{is} [-]
Mean and standard deviation
4000
3000
2000
1000
0
-1000
-2000

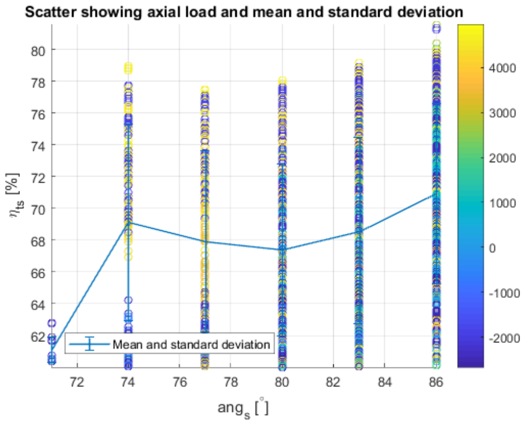
Scatter showing axial load and mean and standard deviation
η_{ts} [%]
80
78
76
74
72
70
68
66
64
62
72
74
76
78
80
82
84
86
ang_s [°]
Mean and standard deviation
4000
3000
2000
1000
0
-1000
-2000

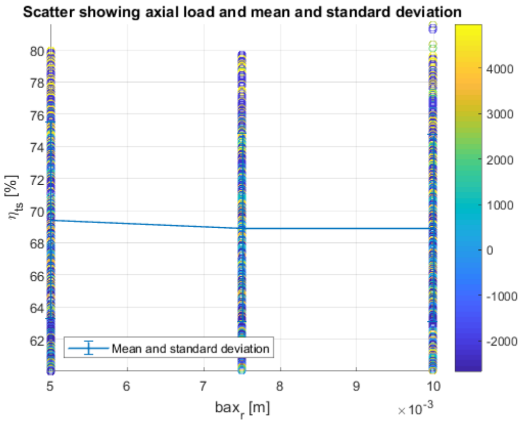
Scatter showing axial load and mean and standard deviation
η_{ts} [%]
80
78
76
74
72
70
68
66
64
62
5
6
7
8
9
10
bax_r [m]
$\times 10^{-3}$
Mean and standard deviation
4000
3000
2000
1000
0
-1000
-2000

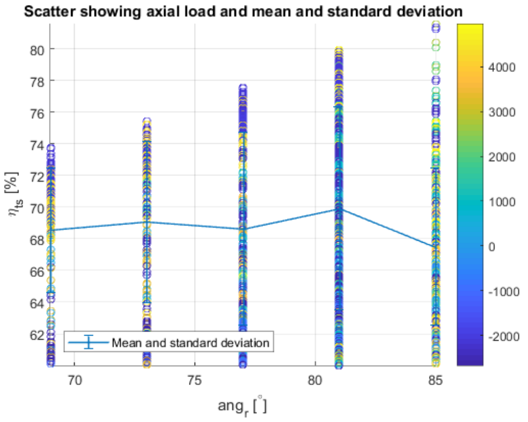
Scatter showing axial load and mean and standard deviation
η_{ts} [%]
80
78
76
74
72
70
68
66
64
62
70
75
80
85
ang_r [°]
Mean and standard deviation
4000
3000
2000
1000
0
-1000
-2000

$\dot{m} = 3.5kg/s$

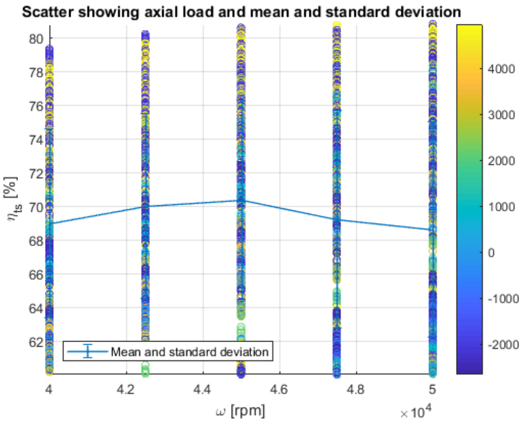
Scatter showing axial load and mean and standard deviation
η_{ts} [%]
80
78
76
74
72
70
68
66
64
62
4
4.2
4.4
4.6
4.8
5
$\times 10^4$
ω [rpm]
Mean and standard deviation
4000
3000
2000
1000
0
-1000
-2000

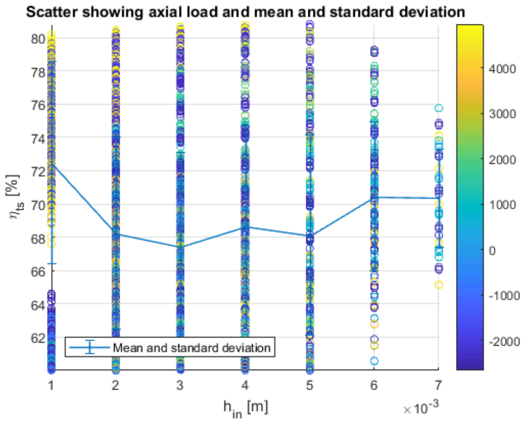
Scatter showing axial load and mean and standard deviation
η_{ts} [%]
80
78
76
74
72
70
68
66
64
62
1
2
3
4
5
6
7
$\times 10^{-3}$
h_{in} [m]
Mean and standard deviation
4000
3000
2000
1000
0
-1000
-2000

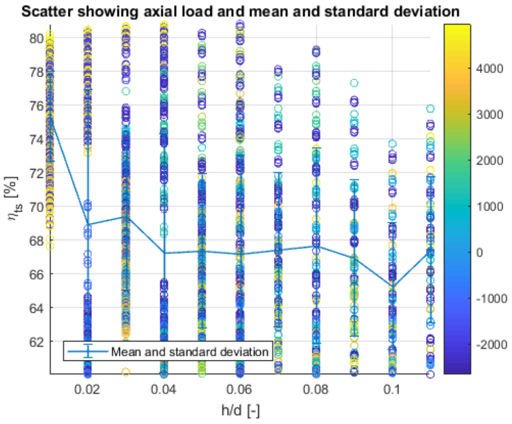
Scatter showing axial load and mean and standard deviation
η_{ts} [%]
80
78
76
74
72
70
68
66
64
62
0.02
0.04
0.06
0.08
0.1
h/d [-]
Mean and standard deviation
4000
3000
2000
1000
0
-1000
-2000

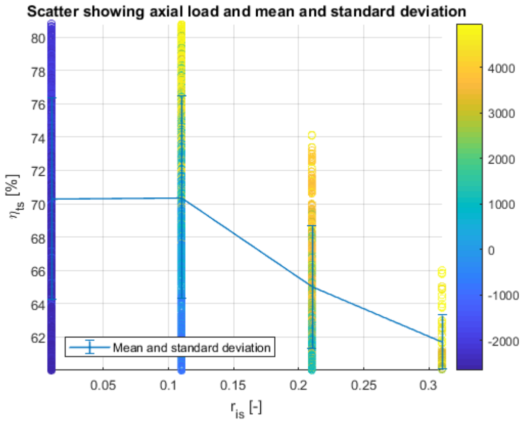
Scatter showing axial load and mean and standard deviation
η_{ts} [%]
80
78
76
74
72
70
68
66
64
62
0.05
0.1
0.15
0.2
0.25
0.3
r_{is} [-]
Mean and standard deviation
4000
3000
2000
1000
0
-1000
-2000

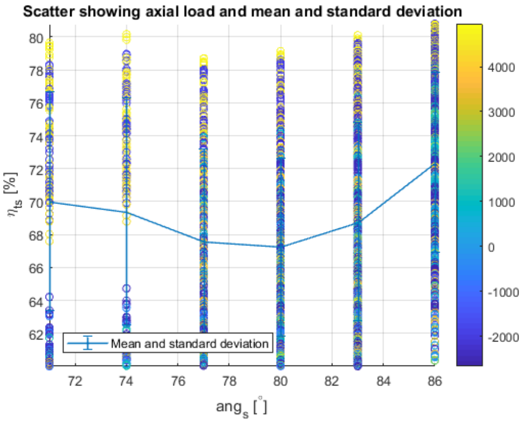
Scatter showing axial load and mean and standard deviation
η_{ts} [%]
80
78
76
74
72
70
68
66
64
62
72
74
76
78
80
82
84
86
ang_s [°]
Mean and standard deviation
4000
3000
2000
1000
0
-1000
-2000

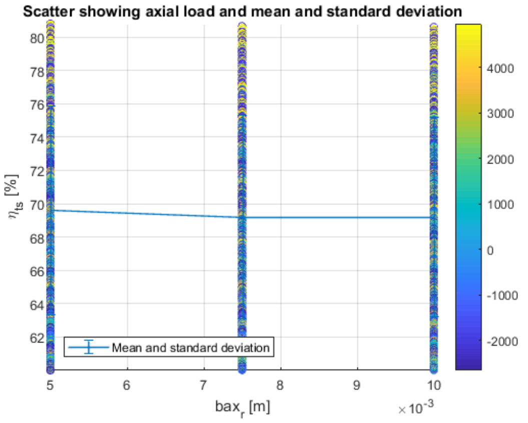
Scatter showing axial load and mean and standard deviation
η_{ts} [%]
80
78
76
74
72
70
68
66
64
62
5
6
7
8
9
10
$\times 10^{-3}$
bax_r [m]
Mean and standard deviation
4000
3000
2000
1000
0
-1000
-2000

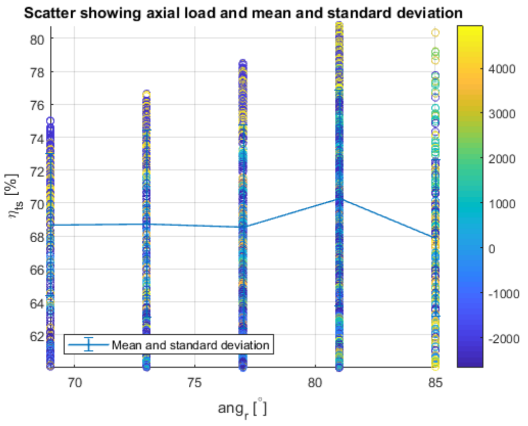

Table A.1: Comparison of the axial turbine results of the Traupel loss model and Soderberg loss model.

$\dot{m}$ $[kg/s]$	ω $[rpm]$	h_{in} $[m]$	h/d [-]	r_{is} [-]	ang_s [°]	bax_r $[m]$	ang_r [°]	gr_{adm} [-]	Traupel η_{ts} [%]	Soderberg η_{ts} [%]	Error [%]
3	50000	0.004	0.05	0.11	86	0.01	85	1	81.6	88.5	8.5
3	40000	0.004	0.04	0.01	86	0.01	85	1	81.3	89.3	9.8
3	40000	0.003	0.03	0.01	86	0.01	85	1	81.3	89.3	9.9
3	47500	0.004	0.05	0.11	86	0.01	85	1	80.4	87.2	8.5
3	50000	0.003	0.04	0.11	86	0.01	85	1	80.1	86.9	8.4
3	47500	0.004	0.04	0.11	86	0.005	81	1	80.0	91.4	14.3
3	50000	0.004	0.04	0.11	86	0.005	81	1	80.0	91.3	14.2
3	45000	0.004	0.04	0.01	86	0.005	81	1	79.9	91.2	14.2
3	47500	0.003	0.03	0.11	86	0.005	81	1	79.9	91.4	14.4
3	50000	0.003	0.03	0.11	86	0.005	81	1	79.9	91.3	14.3
3	45000	0.003	0.03	0.01	86	0.005	81	1	79.8	91.2	14.3
3	47500	0.004	0.04	0.01	86	0.005	81	1	79.7	91.1	14.3
3	47500	0.004	0.04	0.11	86	0.0075	81	1	79.7	90.9	14.0
3	50000	0.004	0.04	0.11	86	0.0075	81	1	79.7	90.8	13.9
3	47500	0.002	0.02	0.11	86	0.005	81	1	79.7	91.4	14.7
3	45000	0.004	0.04	0.01	86	0.0075	81	1	79.7	90.8	13.9
3	50000	0.004	0.05	0.01	86	0.005	81	1	79.7	90.1	13.0
3	50000	0.002	0.02	0.11	86	0.005	81	1	79.7	91.3	14.6
3	47500	0.003	0.03	0.11	86	0.0075	81	1	79.7	90.9	14.1
3	47500	0.003	0.03	0.01	86	0.005	81	1	79.7	91.1	14.4

A.2. RADIAL INFLOW TURBINE

$\dot{m} = 1 kg/s$

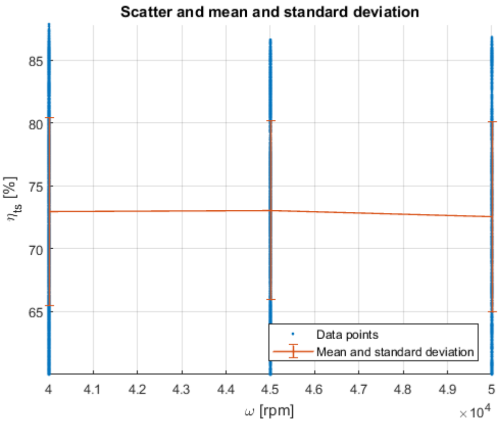
Scatter and mean and standard deviation
η_{ts} [%]
85
80
75
70
65
4
4.1
4.2
4.3
4.4
4.5
4.6
4.7
4.8
4.9
5
ω [rpm]
× 10^4
Data points
Mean and standard deviation

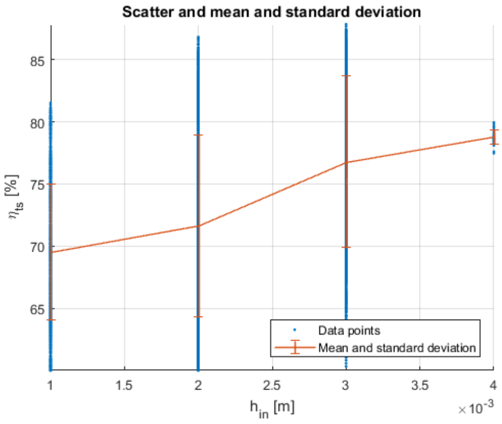
Scatter and mean and standard deviation
η_{ts} [%]
85
80
75
70
65
1
1.5
2
2.5
3
3.5
4
h_{in} [m]
× 10^-3
Data points
Mean and standard deviation

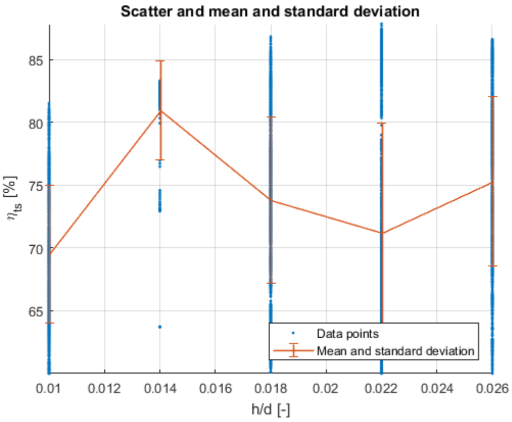
Scatter and mean and standard deviation
η_{ts} [%]
85
80
75
70
65
0.01
0.012
0.014
0.016
0.018
0.02
0.022
0.024
0.026
h/d [-]
Data points
Mean and standard deviation

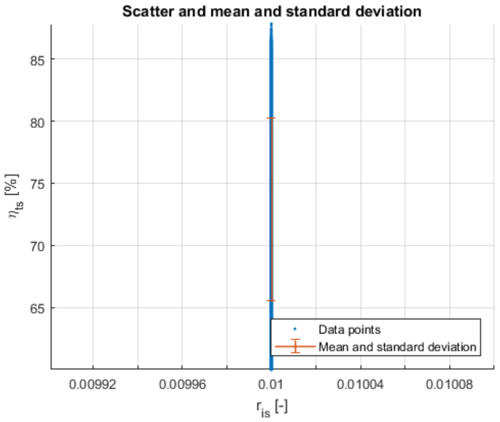
Scatter and mean and standard deviation
η_{ts} [%]
85
80
75
70
65
0.00992
0.00996
0.01
0.01004
0.01008
r_{is} [-]
Data points
Mean and standard deviation

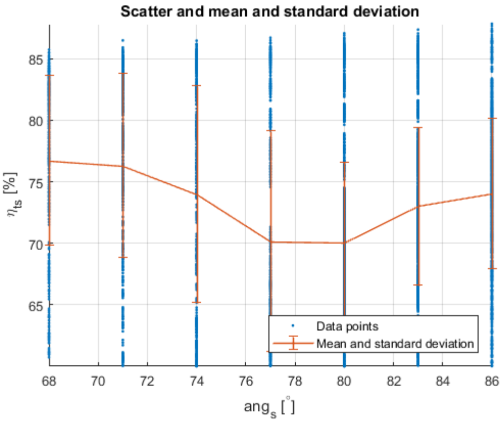
Scatter and mean and standard deviation
η_{ts} [%]
85
80
75
70
65
68
70
72
74
76
78
80
82
84
86
ang_s [°]
Data points
Mean and standard deviation

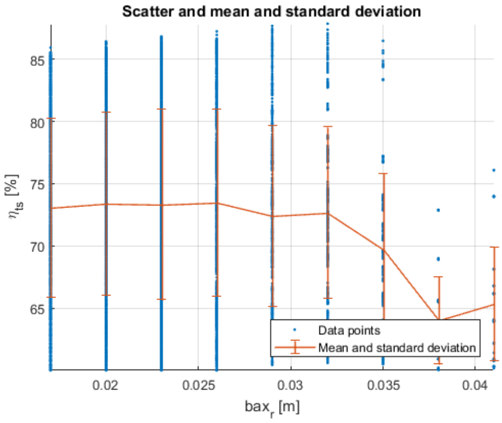
Scatter and mean and standard deviation
η_{ts} [%]
85
80
75
70
65
0.02
0.025
0.03
0.035
0.04
bax_r [m]
Data points
Mean and standard deviation

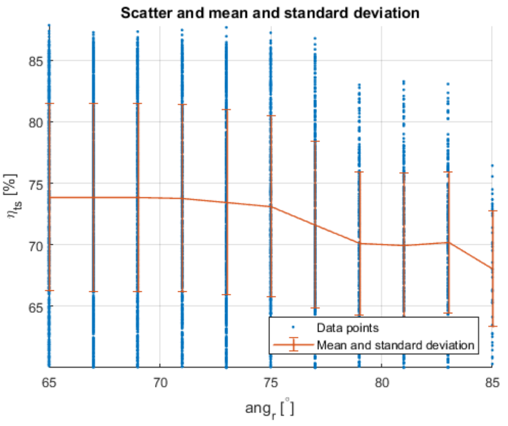
Scatter and mean and standard deviation
η_{ts} [%]
85
80
75
70
65
65
70
75
80
85
ang$_r$ [°]
Data points
Mean and standard deviation

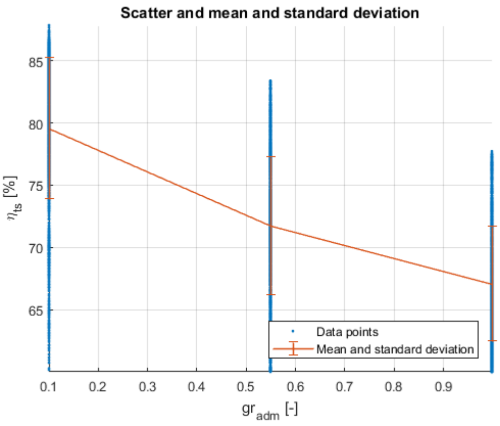
Scatter and mean and standard deviation
η_{ts} [%]
85
80
75
70
65
0.1
0.2
0.3
0.4
0.5
0.6
0.7
0.8
0.9
gr$_{adm}$ [-]
Data points
Mean and standard deviation

$\dot{m} = 2kg/s$

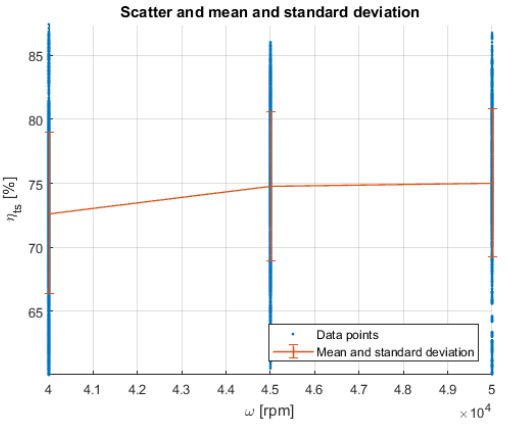
Scatter and mean and standard deviation
η_{ts} [%]
85
80
75
70
65
4
4.1
4.2
4.3
4.4
4.5
4.6
4.7
4.8
4.9
5
ω [rpm]
$\times 10^4$
Data points
Mean and standard deviation

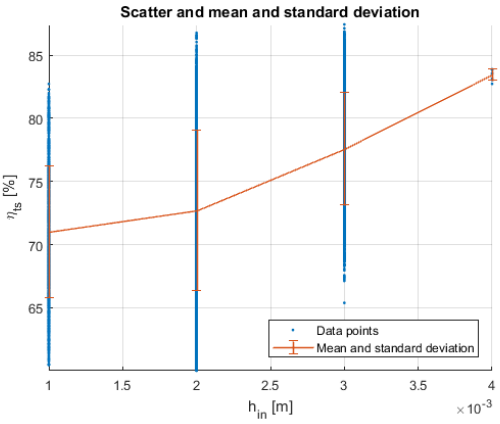
Scatter and mean and standard deviation
η_{ts} [%]
85
80
75
70
65
1
1.5
2
2.5
3
3.5
4
h$_{in}$ [m]
$\times 10^{-3}$
Data points
Mean and standard deviation

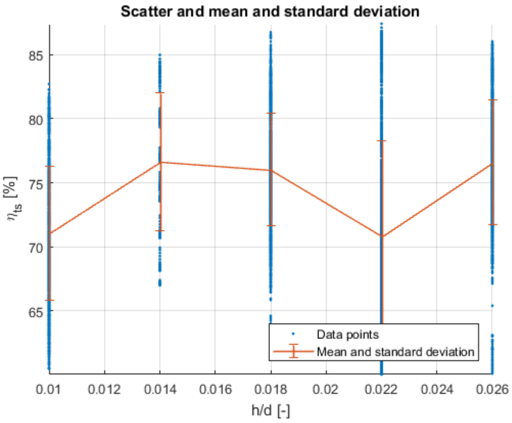
Scatter and mean and standard deviation
η_{ts} [%]
85
80
75
70
65
0.01
0.012
0.014
0.016
0.018
0.02
0.022
0.024
0.026
h/d [-]
Data points
Mean and standard deviation

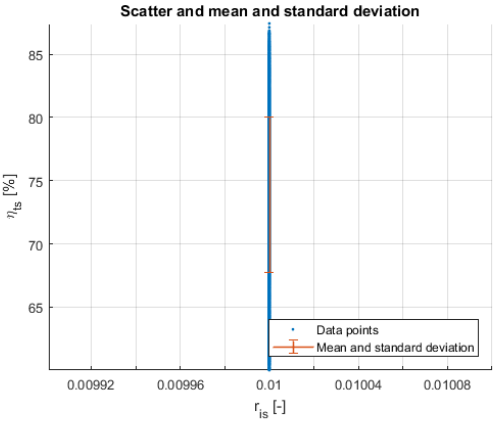
Scatter and mean and standard deviation
η_{ts} [%]
85
80
75
70
65
0.00992
0.00996
0.01
0.01004
0.01008
r$_{is}$ [-]
Data points
Mean and standard deviation

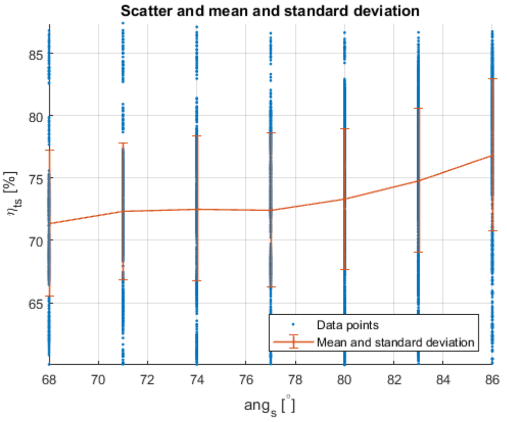
Scatter and mean and standard deviation
η_{ts} [%]
85
80
75
70
65
68
70
72
74
76
78
80
82
84
86
ang_s [°]
Data points
Mean and standard deviation

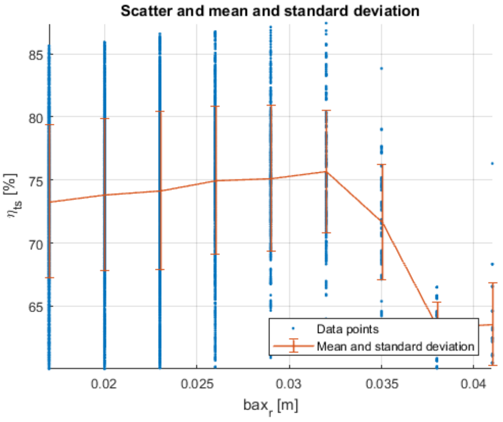
Scatter and mean and standard deviation
η_{ts} [%]
85
80
75
70
65
0.02
0.025
0.03
0.035
0.04
bax_r [m]
Data points
Mean and standard deviation

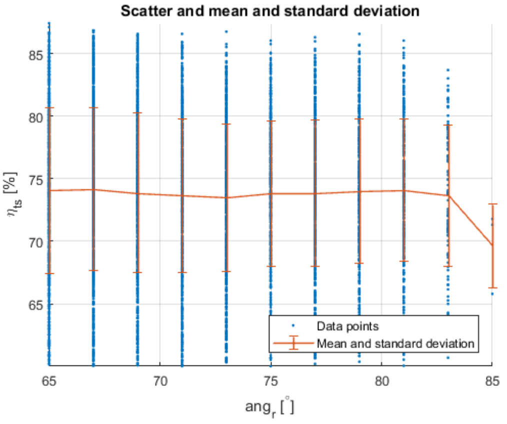
Scatter and mean and standard deviation
η_{ts} [%]
85
80
75
70
65
65
70
75
80
85
ang_r [°]
Data points
Mean and standard deviation

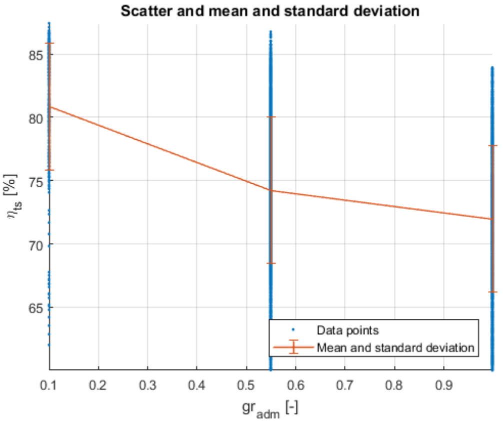
Scatter and mean and standard deviation
η_{ts} [%]
85
80
75
70
65
0.1
0.2
0.3
0.4
0.5
0.6
0.7
0.8
0.9
gr_{adm} [-]
Data points
Mean and standard deviation

$\dot{m} = 3kg/s$

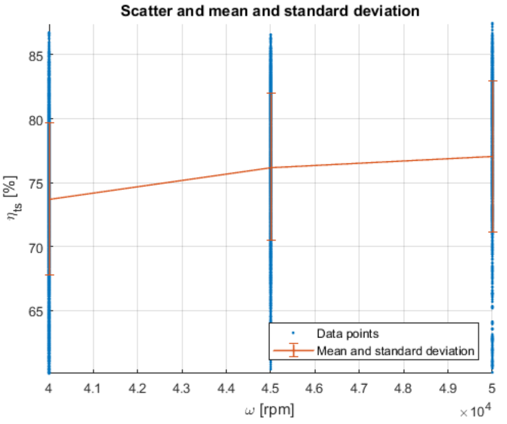
Scatter and mean and standard deviation
η_{ts} [%]
85
80
75
70
65
4
4.1
4.2
4.3
4.4
4.5
4.6
4.7
4.8
4.9
5
$\times 10^4$
ω [rpm]
Data points
Mean and standard deviation

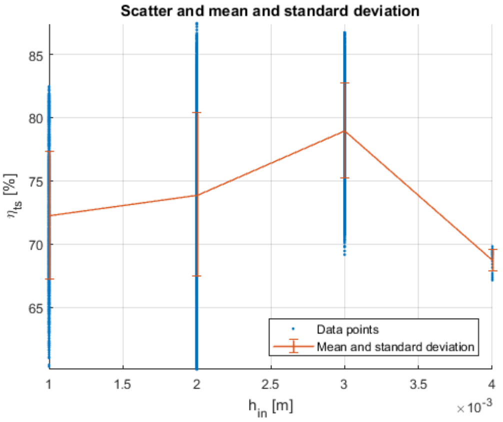
Scatter and mean and standard deviation
η_{ts} [%]
85
80
75
70
65
1
1.5
2
2.5
3
3.5
4
$\times 10^{-3}$
h_{in} [m]
Data points
Mean and standard deviation

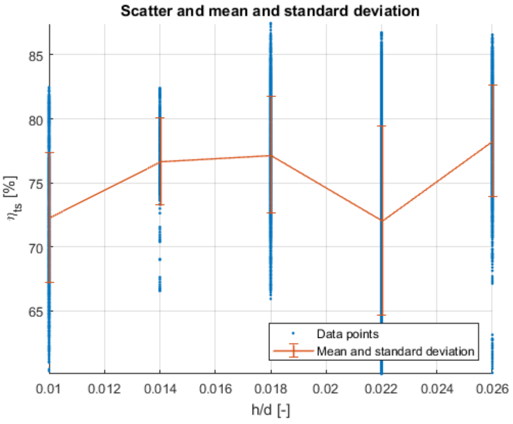
Scatter and mean and standard deviation
85
80
75
70
65
η_{ts} [%]
0.01
0.012
0.014
0.016
0.018
0.02
0.022
0.024
0.026
h/d [-]
Data points
Mean and standard deviation

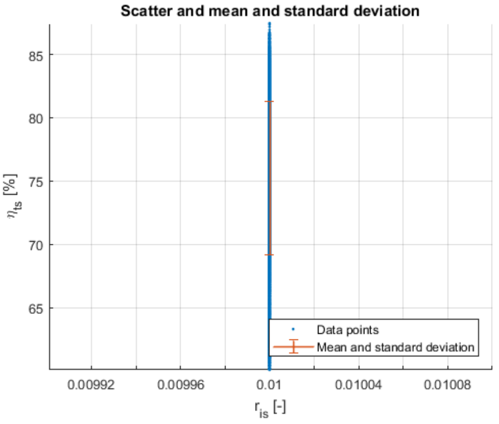
Scatter and mean and standard deviation
85
80
75
70
65
η_{ts} [%]
0.00992
0.00996
0.01
0.01004
0.01008
r_{is} [-]
Data points
Mean and standard deviation

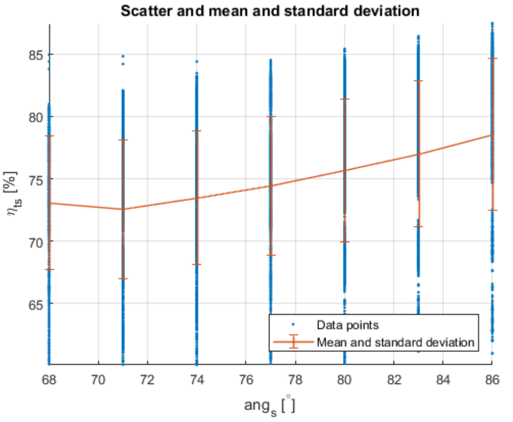
Scatter and mean and standard deviation
85
80
75
70
65
η_{ts} [%]
68
70
72
74
76
78
80
82
84
86
ang_s [°]
Data points
Mean and standard deviation

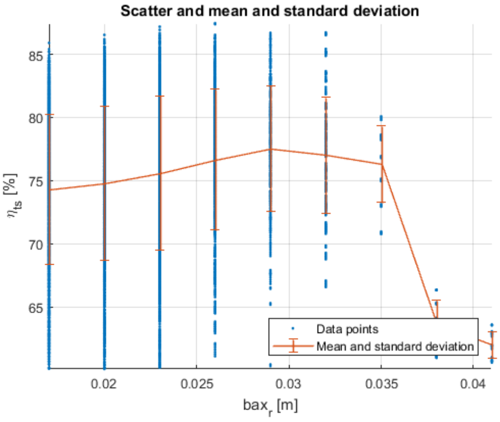
Scatter and mean and standard deviation
85
80
75
70
65
η_{ts} [%]
0.02
0.025
0.03
0.035
0.04
bax_r [m]
Data points
Mean and standard deviation

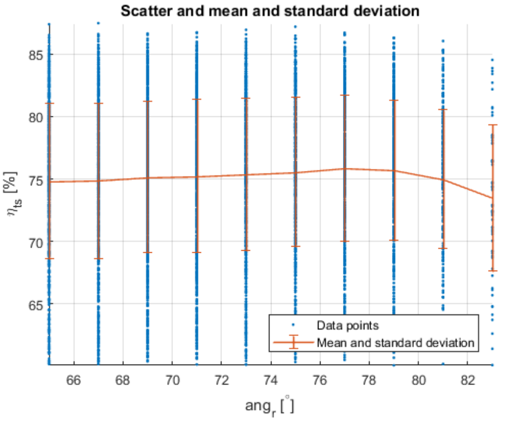
Scatter and mean and standard deviation
85
80
75
70
65
η_{ts} [%]
66
68
70
72
74
76
78
80
82
ang_r [°]
Data points
Mean and standard deviation

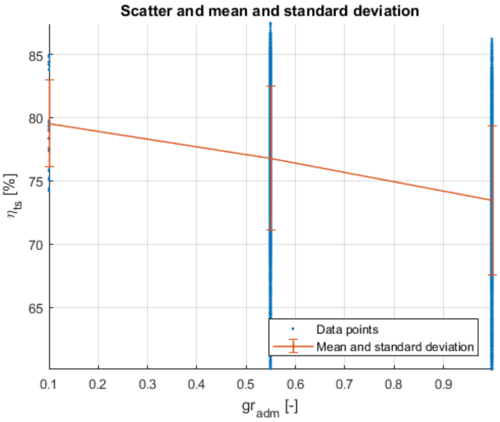
Scatter and mean and standard deviation
85
80
75
70
65
η_{ts} [%]
0.1
0.2
0.3
0.4
0.5
0.6
0.7
0.8
0.9
gr_{adm} [-]
Data points
Mean and standard deviation

Table A.2: Comparison of the radial inflow turbine results of the Traupel loss model and Glassman loss model.

$\dot{m}$ [kg/s]	ω [rpm]	h_{in} [m]	h/d [-]	r_{is} [-]	ang_s [°]	bax_r [m]	ang_r [°]	gr_{adm} [-]	Traupel η_{ts} [%]	Glassman η_{ts} [%]	Error [%]
3	45000	0.003	0.026	0.01	77	0.017	81	0.998	76.9	85.4	10.97
3	50000	0.001	0.01	0.01	77	0.02	79	0.998	76.9	83.0	7.92
3	45000	0.002	0.018	0.01	77	0.02	79	0.998	76.8	83.9	9.31
3	45000	0.003	0.026	0.01	77	0.017	79	0.998	76.7	85.7	11.71
3	50000	0.001	0.01	0.01	77	0.02	77	0.998	76.7	83.4	8.64
3	50000	0.001	0.01	0.01	77	0.017	81	0.998	76.7	83.2	8.48
3	45000	0.002	0.018	0.01	77	0.02	77	0.998	76.6	84.2	9.94
3	50000	0.001	0.01	0.01	77	0.02	75	0.998	76.6	83.6	9.14
3	50000	0.001	0.01	0.01	77	0.017	79	0.998	76.6	83.8	9.43
3	45000	0.003	0.026	0.01	77	0.017	77	0.998	76.5	85.9	12.24
3	45000	0.002	0.018	0.01	77	0.017	81	0.998	76.5	83.9	9.71
3	50000	0.001	0.01	0.01	77	0.023	71	0.998	76.5	83.0	8.60
3	45000	0.002	0.018	0.01	77	0.023	71	0.998	76.4	84.1	10.05
3	50000	0.001	0.01	0.01	77	0.017	77	0.998	76.4	84.1	10.03
3	45000	0.002	0.018	0.01	77	0.02	75	0.998	76.4	84.3	10.41
3	50000	0.001	0.01	0.01	77	0.02	73	0.998	76.4	83.6	9.52
3	50000	0.001	0.01	0.01	77	0.023	69	0.998	76.3	83.0	8.82
3	45000	0.002	0.018	0.01	77	0.017	79	0.998	76.3	84.3	10.55
3	45000	0.003	0.026	0.01	77	0.017	75	0.998	76.2	85.9	12.69
3	45000	0.002	0.018	0.01	77	0.023	69	0.998	76.2	84.0	10.26
3	50000	0.001	0.01	0.01	77	0.017	75	0.998	76.2	84.2	10.47
3	50000	0.001	0.01	0.01	77	0.02	71	0.998	76.2	83.6	9.80
3	50000	0.001	0.01	0.01	77	0.023	67	0.998	76.1	83.0	8.95
3	45000	0.002	0.018	0.01	77	0.02	73	0.998	76.1	84.3	10.79
3	45000	0.002	0.018	0.01	77	0.017	77	0.998	76.1	84.5	11.12
3	45000	0.002	0.018	0.01	77	0.023	67	0.998	76.0	83.9	10.35
3	50000	0.001	0.01	0.01	77	0.023	65	0.998	76.0	82.8	9.03
3	50000	0.001	0.01	0.01	77	0.02	69	0.998	75.9	83.5	10.00
3	50000	0.001	0.01	0.01	77	0.017	73	0.998	75.9	84.1	10.81
3	45000	0.003	0.026	0.01	77	0.017	73	0.998	75.9	85.8	13.07
3	45000	0.003	0.026	0.01	77	0.02	67	0.998	75.9	85.5	12.64
3	45000	0.002	0.018	0.01	77	0.02	71	0.998	75.9	84.3	11.09
3	45000	0.002	0.018	0.01	77	0.023	65	0.998	75.8	83.7	10.39
3	45000	0.002	0.018	0.01	77	0.017	75	0.998	75.8	84.6	11.57
3	50000	0.001	0.01	0.01	77	0.02	67	0.998	75.8	83.4	10.10
3	50000	0.001	0.01	0.01	77	0.017	71	0.998	75.7	84.0	11.08
3	45000	0.002	0.018	0.01	77	0.02	69	0.998	75.6	84.1	11.30
3	50000	0.001	0.01	0.01	77	0.02	65	0.998	75.6	83.2	10.14
3	45000	0.003	0.026	0.01	77	0.017	71	0.998	75.5	85.7	13.45
3	45000	0.002	0.018	0.01	77	0.017	73	0.998	75.5	84.5	11.95
3	50000	0.001	0.01	0.01	77	0.017	69	0.998	75.4	83.9	11.26
3	45000	0.002	0.018	0.01	77	0.02	67	0.998	75.4	83.9	11.38
3	45000	0.003	0.026	0.01	77	0.017	69	0.998	75.2	85.5	13.71
3	45000	0.002	0.018	0.01	77	0.017	71	0.998	75.1	84.4	12.26
3	45000	0.002	0.018	0.01	77	0.02	65	0.998	75.1	83.7	11.39
3	50000	0.001	0.01	0.01	77	0.017	67	0.998	75.1	83.7	11.34
3	50000	0.001	0.01	0.01	74	0.02	79	0.998	75.1	82.6	9.93
3	50000	0.001	0.01	0.01	74	0.017	81	0.998	75.1	83.0	10.44
3	50000	0.001	0.01	0.01	74	0.02	77	0.998	75.0	82.9	10.59
3	50000	0.001	0.01	0.01	74	0.017	79	0.998	75.0	83.4	11.27

A.3. REFINEMENT

TRAUPEL LOSS MODEL

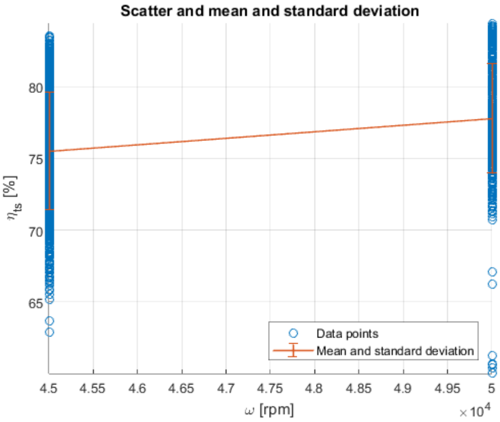

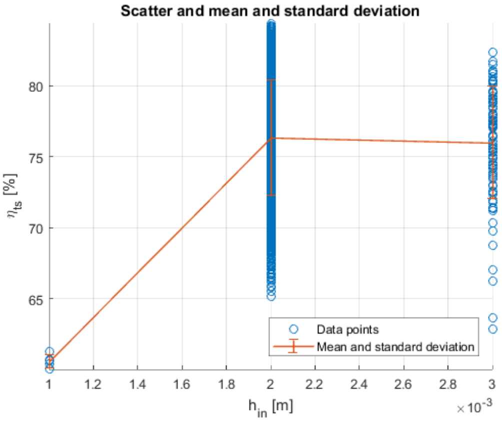

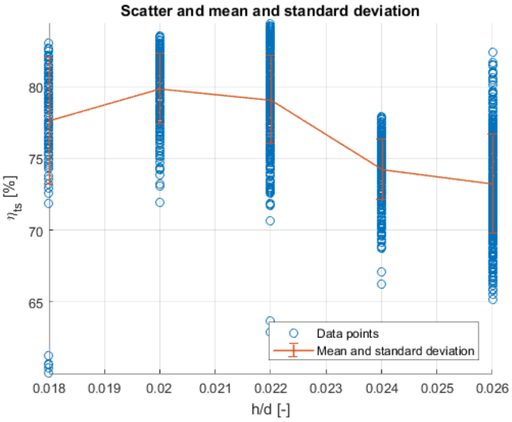

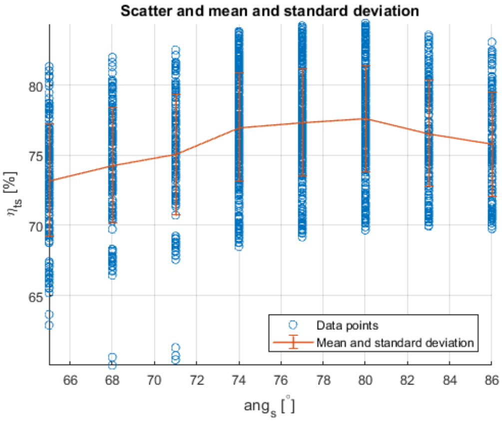

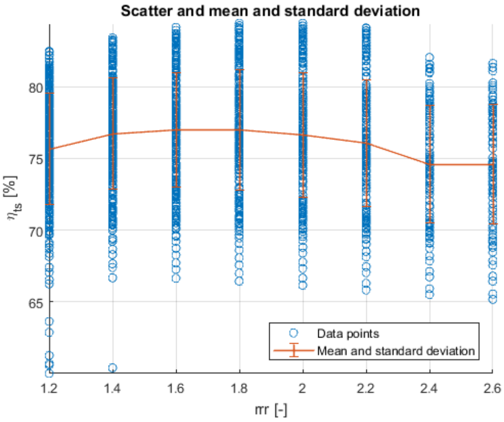

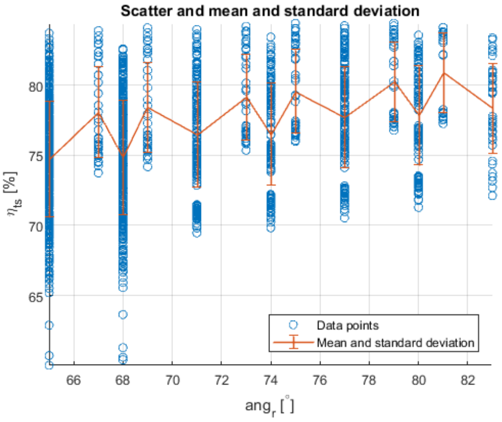

GLASSMAN LOSS MODEL

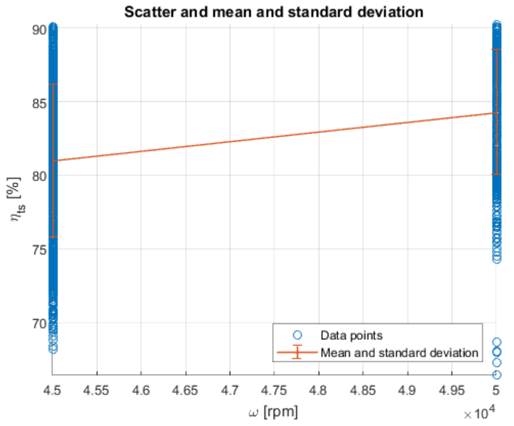

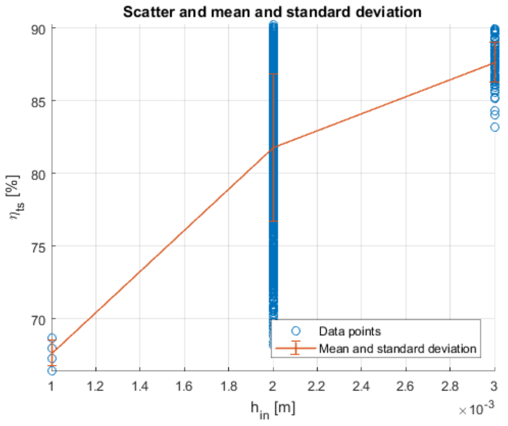

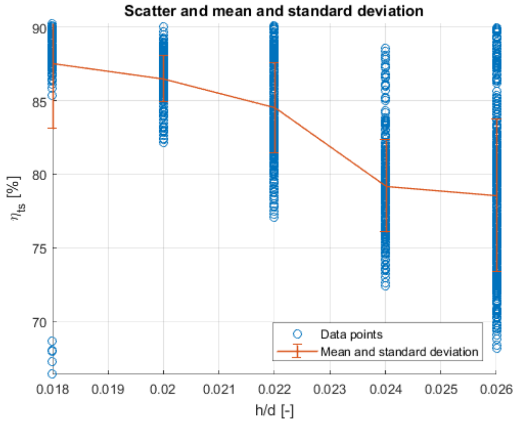

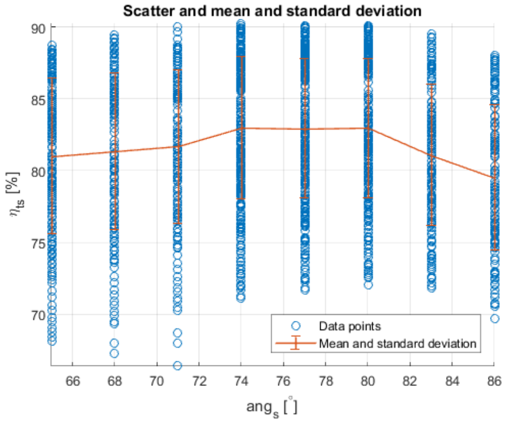

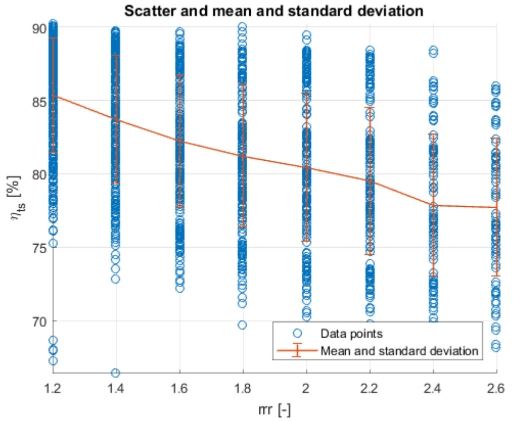

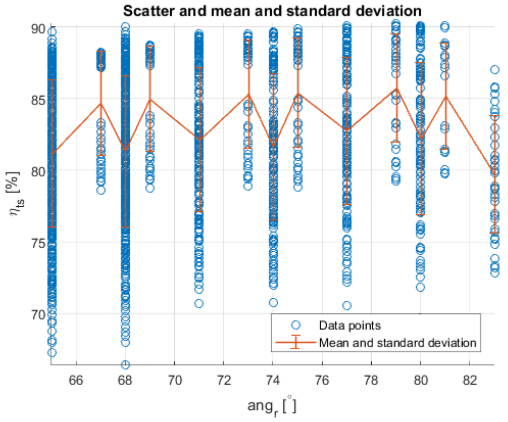

B

AERODYNAMIC DESIGN PARAMETERS AND RESULTS

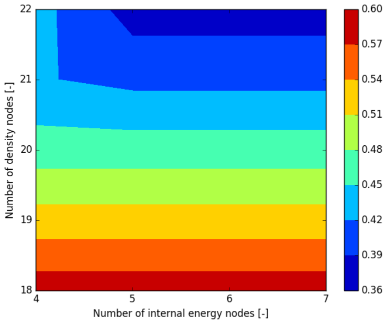

Figure B.1: Maximum error [%] in interpolated pressure.

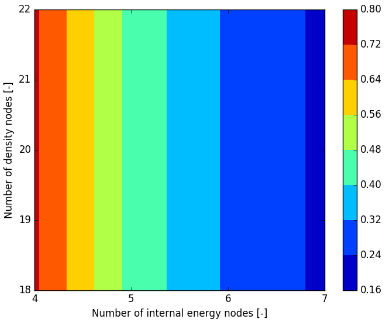

Figure B.2: Maximum error [%] in interpolated dynamic viscosity.

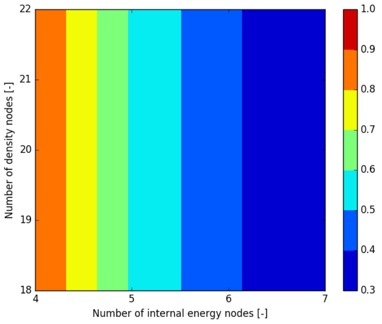

Figure B.3: Maximum error [%] in interpolated ratio of specific heats.

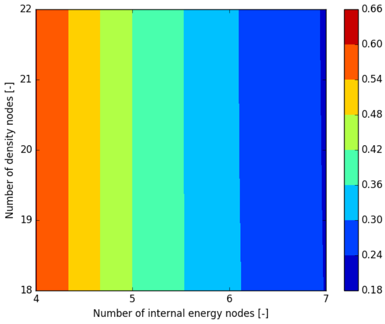

Figure B.4: Maximum error [%] in interpolated heat capacity at constant pressure.

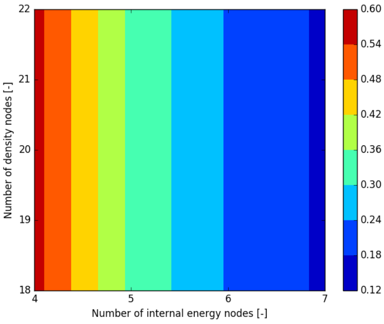

Figure B.5: Maximum error [%] in interpolated heat capacity at constant volume.

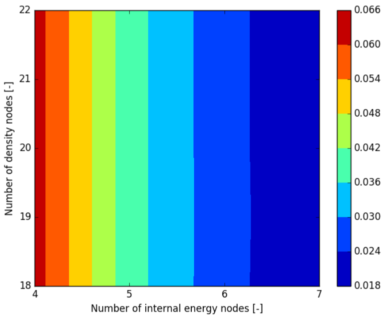

Figure B.6: Maximum error [%] in interpolated enthalpy.

Table B.1: SU2 gas parameters overview.

Parameter	Value
Fluid model	Ideal gas
γ $[-]$	1.238
R $[J/kgK]$	189
Viscosity model	Sutherland
μ_{ref} $[Ns/m^2]$	1.48E-5
$\mu_{t,ref}$ $[K]$	293.15
Sutherland constant $[-]$	240
Conductivity model	Constant Prandtl

Table B.2: SU2 simulation parameters overview.

Parameter	Value
Physical governing equations	RANS
Turbulence model	SST
Mathematical problem	Direct
Free-stream turbulence intensity	0.1
Free-stream turbulent to laminar viscosity ratio	100
Mixing plane interface kind	Linear interpolation
Turbulent mixing plane	Yes
Average process kind	Mixedout
Performance average process kind	Mixedout
Average Mach limit	0.05
Numerical method for spatial gradients	Weighted least squares
Linear solver	FGMRES
Linear solver preconditioner	LU_SGS
Convective numerical method	ROE
Spatial numerical order integration	Second order limiter
Slope limiter	Van Albada
Artificial dissipation coefficients	(0.15, 0.5, 0.02)
Time discretization	Euler implicit
Relaxation coefficient	1.4
Entropy coefficient	0.5
Convective numerical method turbulence	Scaler upwind
Spatial numerical order turbulence	Second order limiter
Slope limiter turbulence	Venkatakrishnan
Time discretization turbulence	Euler implicit
CFL reduction number turbulence	0.001
Relaxation factor turbulence	1.5

Table B.3: Eilmer4 gas parameters overview.

Parameter	Value
Fluid model	Ideal gas
γ $[-]$	1.238
R $[J/kgK]$	189
Viscosity model	Sutherland
μ_{ref} $[Ns/m^2]$	1.48E-5
$\mu_{t,ref}$ $[K]$	293.15
Sutherland constant $[-]$	240
Conductivity model	Sutherland

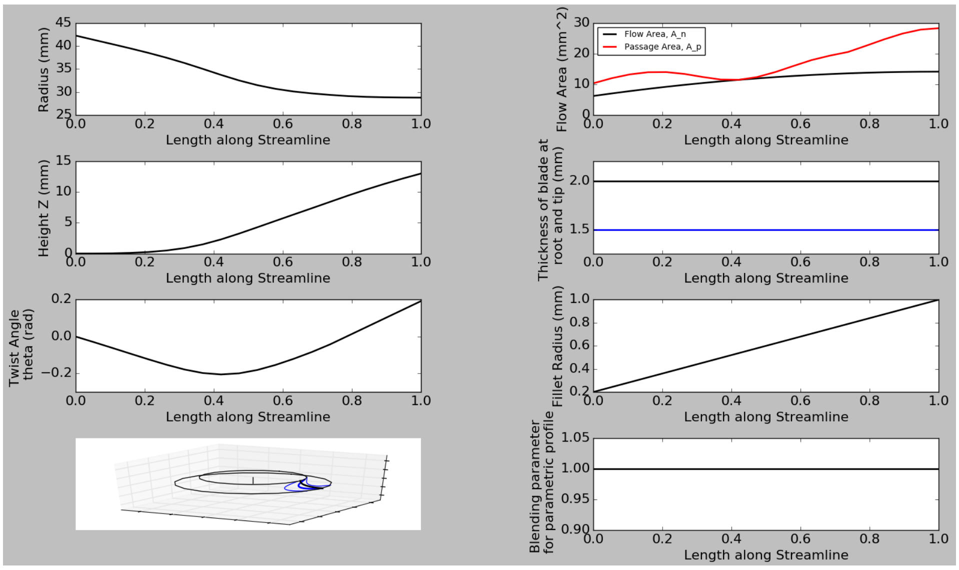

Figure B.7: Generation 1 turbine rotor parameters variation along streamline.

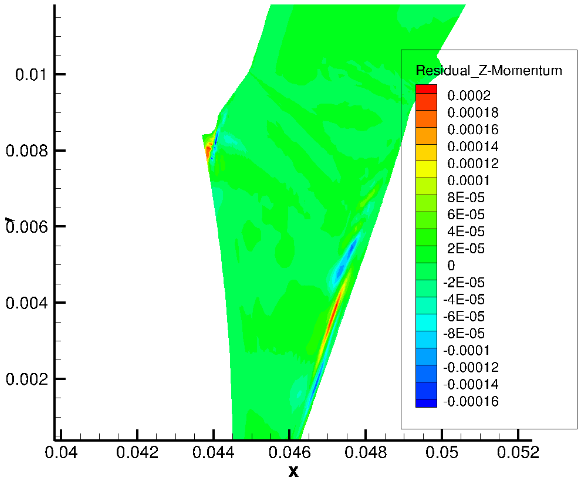

Figure B.8: Generation 1 turbine Z-momentum residuals for the less fine supersonic stator mesh.

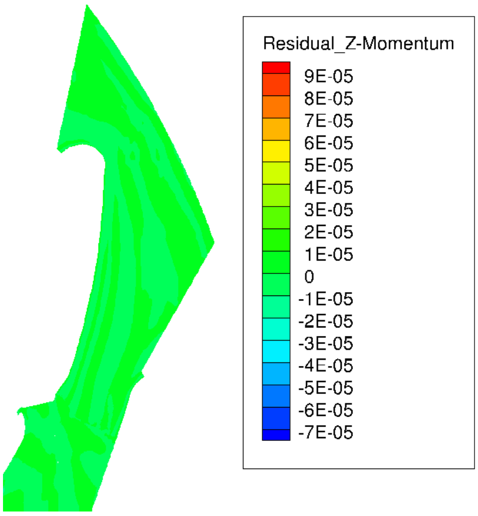

Figure B.9: Generation 1 turbine Z-momentum residuals for the finer supersonic stator mesh.

Table B.4: Eilmer4 simulation parameters overview.

Parameter	Value
Physical governing equations	RANS
Gas dynamics update scheme	Predictor-corrector
Free-stream turbulence intensity	0.05
Free-stream turbulent to laminar viscosity ratio	100
Spatial numerical order integration	Second order
Numerical method for spatial gradients	Least squares
Slope limiter	Venkatakrishnan
Flux calculator	Adaptive
Thermodynamic interpolator	Rhou

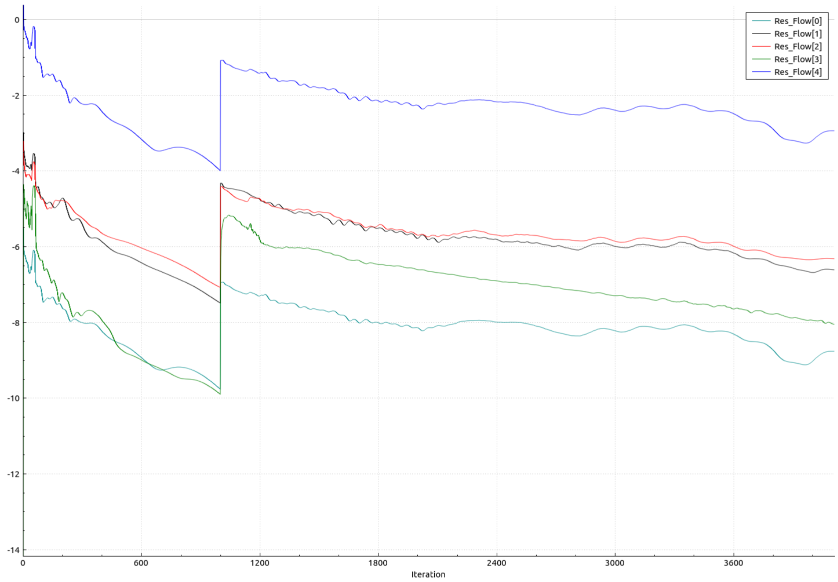

Figure B.10: Generation 1 turbine SU2 convergence history.

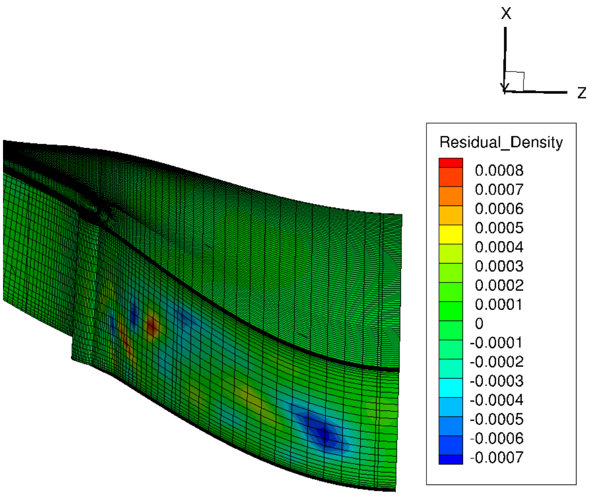

Figure B.11: Generation 1 turbine density residuals.

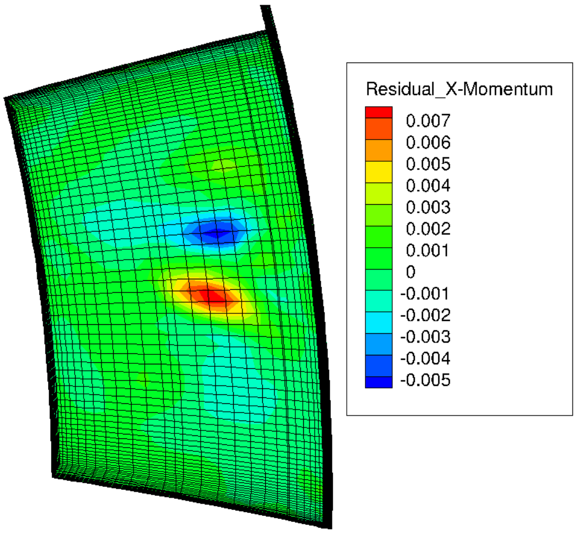

Figure B.12: Generation 1 turbine X-momentum residuals.

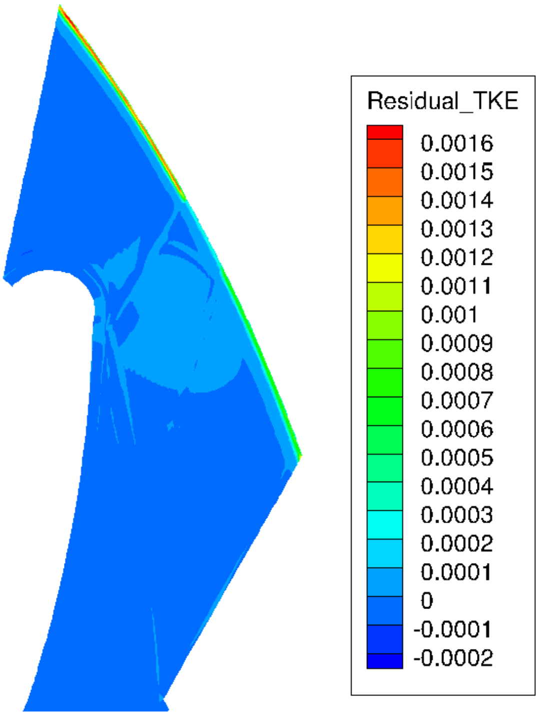

Figure B.13: Generation 1 turbine TKE residuals.

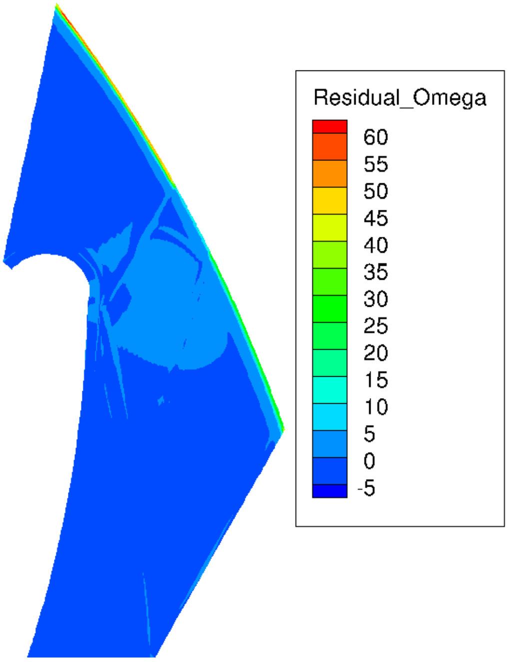

Figure B.14: Generation 1 turbine omega residuals.

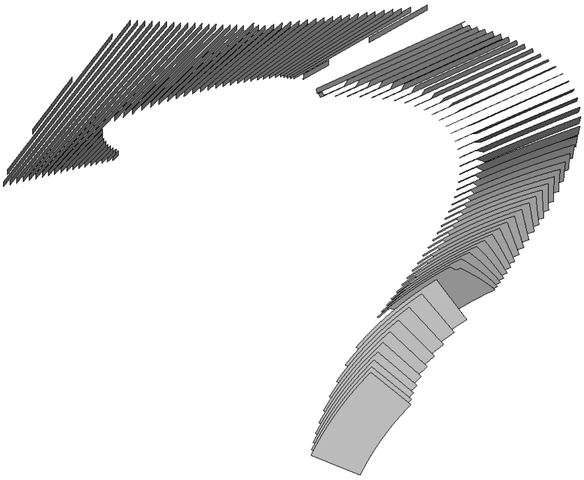

Figure B.15: Generation 1 turbine slices for post-processing the simulation.

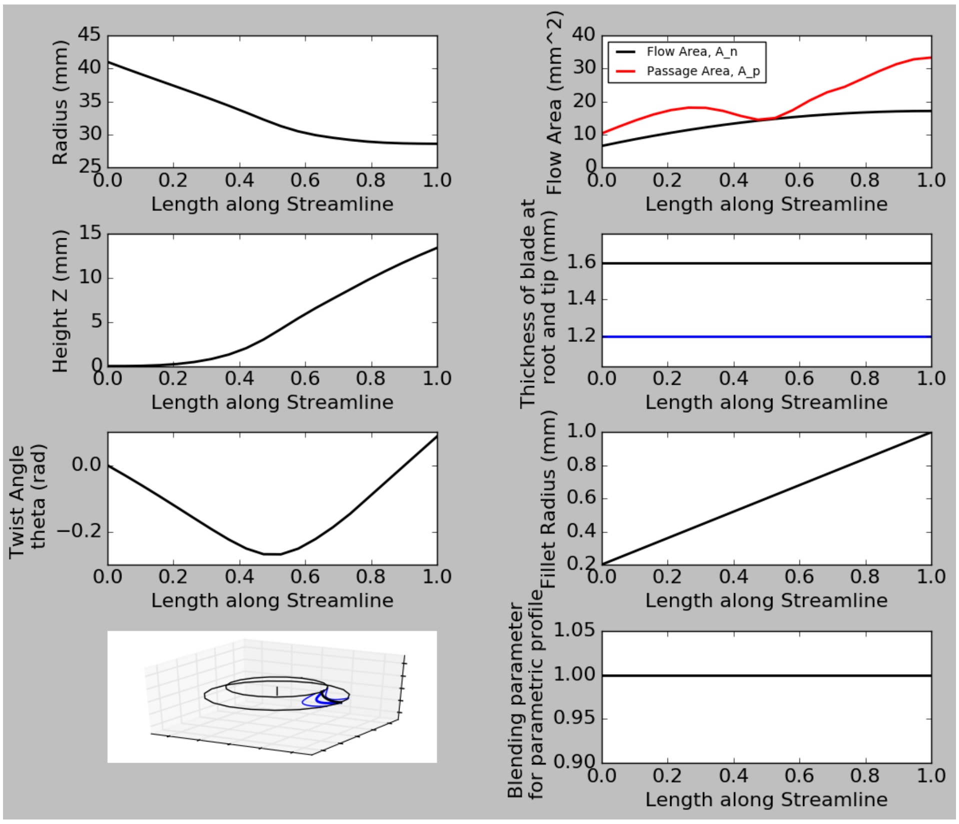

Figure B.16: Generation 2 turbine rotor parameters variation along streamline.

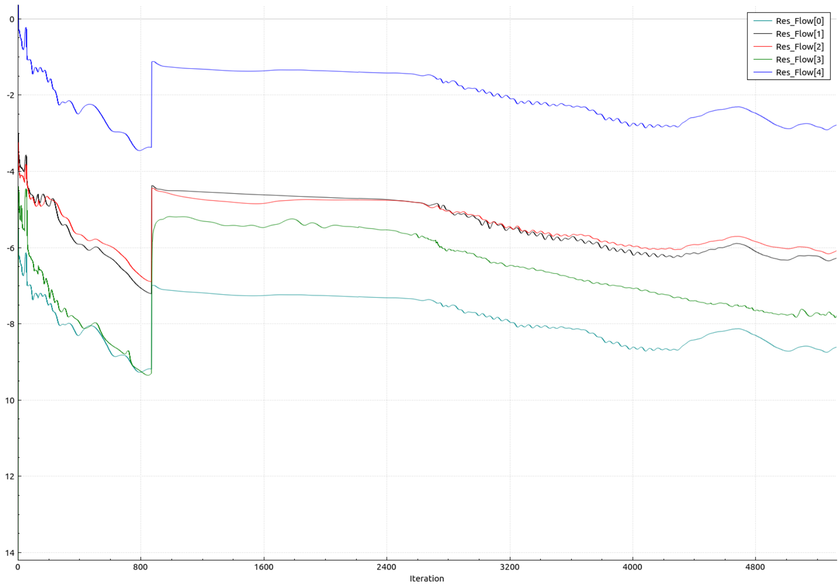

Figure B.17: Generation 2 turbine SU2 convergence history.

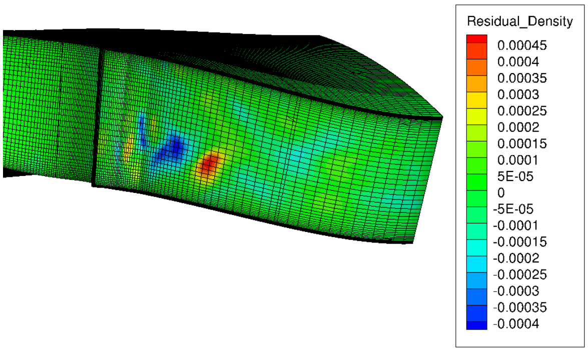

Figure B.18: Generation 2 turbine SU2 density residuals.

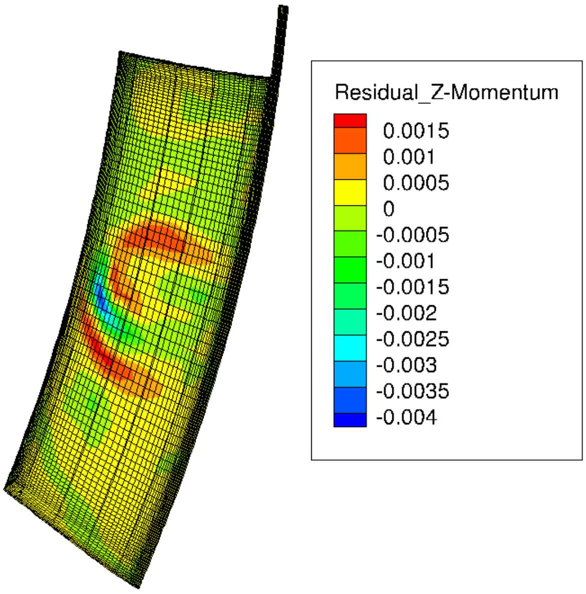

Figure B.19: Generation 2 turbine SU2 Z-momentum residuals.

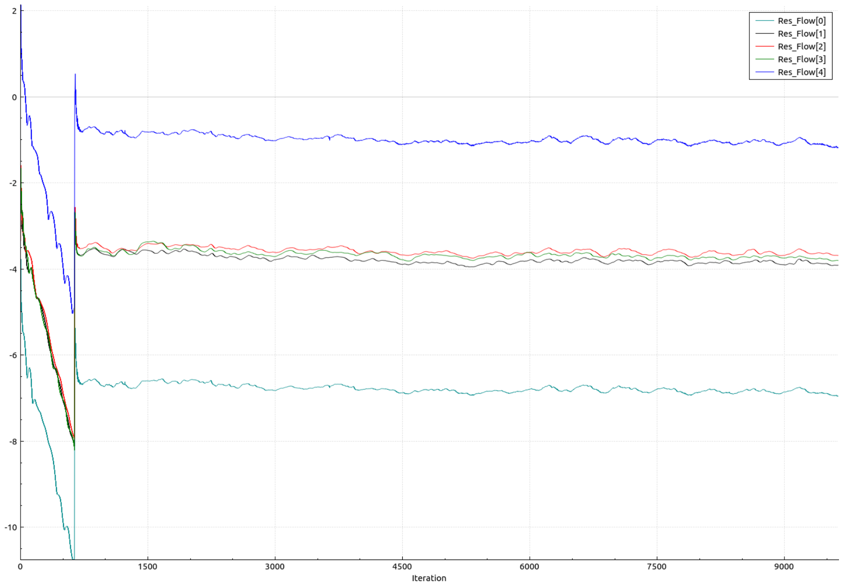

Figure B.20: Generation 3 turbine SU2 convergence history.

BIBLIOGRAPHY

[1] G. Angelino, *Perspectives for the liquid phase compression gas turbine,* Journal of Engineering for Power **89**, 229 (1967).

[2] E. Feher, *The supercritical thermodynamic power cycle,* Energy Convention **8**, 85 (1968).

[3] V. Dostal, *A supercritical carbon dioxide cycle for next generation nuclear reactors*, Tech. Rep. (Massachusetts Institute of Technology, 2004).

[4] H. Yamaguchi, X. Zhang, K. Fujima, M. Enomoto, and N. Sawada, *Solar energy powered rankine cycle using supercritical* co_2*,* Applied Thermal Engineering **26**, 2345 (2006).

[5] I. Jahn and J. Keep, *On and off-design performance of supercritical carbon dioxide power cycles,* Proceedings of Shanghai 2017 Global Power and Propulsion Forum (2017).

[6] H. Russell, A. Rowlands, C. Ventura, and I. Jahn, *Design and testing process for a 7 kw radial inflow refrigerant turbine at the university of queensland,* Proceedings of ASME Turbo Expo 2016: Turbomachinery Technical Conference and Exposition Seoul (2016).

[7] P. Walsh and P. Fletcher, *Gas Turbine Performance* (Blackwell Publishing, 2004).

[8] O. Balje, *A study on design criteria and matching of turbomachines: Part a—similarity relations and design criteria of turbines,* Journal of Engineering for Power **84**, 83 (1962).

[9] H. Rohlik, *Analytical determination of radial inflow turbine design geometry for maximum efficiency,* NASA TN D-4348 (1968).

[10] Y. Muto, M. Aritomi, T. Ishizuka, and N. Watanabe, *Comparison of supercritical* co_2 *gas turbine cycle and brayton* co_2 *gas turbine cycle for solar thermal power plants,* The 4th International Symposium - Supercritical CO_2 Power Cycles Pittsburgh (2014).

[11] C. Kalra, D. Hofer, E. Sevincer, J. Moore, and K. Brun, *Development of high efficiency hot gas turboexpander for optimized csp supercritical* co_2 *power block operation,* The 4th International Symposium - Supercritical CO_2 Power Cycles Pittsburgh (2014).

[12] C. Turchi, *10MW Supercritical* CO_2 *Turbine Test*, Tech. Rep. (National Renewable Energy Laboratory (NREL), Golden, CO (United States), 2014).

[13] J. Qi, T. Reddell, K. Qin, K. Hooman, and I. Jahn, *Supercritical* co_2 *radial turbine design performance as a function of turbine size parameters,* Proceedings of ASME Turbo Expo 2016: Turbomachinery Technical Conference and Exposition Seoul (2016).

[14] S. Spazzoli, *Supercritical* CO_2 *power cycle for solar applications: Thermodynamic analysis and 1D turbomachinery design*, Tech. Rep. (Delft University of Technology, 2016).

[15] C. Ventura, P. Jacobs, A. Rowlands, P. Petrie-Repar, and E. Sauret, *Preliminary design and performance estimation of radial inflow turbines: An automated approach,* Journal of Fluids Engineering **134**, 031102 (2012).

[16] D. Chapman and D. Arias, *An assessment of the supercritical carbon dioxide cycle for use in a solar parabolic trough power plant,* Presentation, Abengoa Solar (2009).

[17] P. Jacobs and R. Gollan, *The user's guide to the Eilmer4 flow simulation program*, Tech. Rep. (2017).

[18] Z. Ma and C. Turchi, *Advanced supercritical carbon dioxide power cycle configurations for use in concentrating solar power systems,* Supercrticial CO_2 Power Cycle Symposium Colorado (2011).

[19] S. Wright, *Mighty might,* Mechanical Engineering Magazine , 40 (2012).

[20] M. Shanechi, M. Odabaee, and K. Hooman, *Optimisation of a high pressure ratio radial-inflow turbine: Coupled cfd-fe analysis,* in *ASME Turbo Expo 2015: Turbine Technical Conference and Exposition* (American Society of Mechanical Engineers, 2015) pp. V02CT45A003–V02CT45A003.

[21] S. Nakano, K. Tsubouchi, H. Shiraiwa, K. Hayashi, and H. Yamada, *A 150 kw radial inflow steam turbine system for the bottoming cycle of reciprocating engines,* ASME Paper No. GT2010-23231 (2010).

[22] E. Sauret and A. Rowlands, *Candidate radial-inflow turbines and high-density working fluids for geothermal power systems,* Energy **36**, 4460 (2011).

[23] G. Persico and M. Pini, *Fluid dynamic design of organic rankine cycle turbines,* Organic Rankine Cycle (ORC) Power Systems: Technologies and Applications , 253 (2016).

[24] F. Rubechini, M. Marconcini, A. Arnone, A. D. Greco, and R. Biagi, *Special challenges in the computational fluid dynamics modeling of transonic turbo-expanders,* Journal of Engineering for Gas Turbines and Power **135**, 102701 (2013).

[25] A. Wheeler and J. Ong, *A study of the three-dimensional unsteady real-gas flows within a transonic orc turbine,* ASME Paper No. GT2014-25475 (2014).

[26] J. Sienicki, A. Moisseytsev, R. Fuller, S. Wright, and P. Pickard, *Scale dependencies of supercritical carbon dioxide brayton cycle technologies and the optimal size for a next-step supercritical* co_2 *cycle demonstration,* in SCO_2 *power cycle symposium* (2011).

[27] A. Glassman, *Turbine design and application* (National Aeronautics and Space Administration, 1994).

[28] O. Balje and R. Binsley, *Axial turbine performance evaluation. part a - loss-geometry relationships,* ASME Journal of Engineering for Power **90**, 341 (1968).

[29] S. Yahya and M. Doyle, *Aerodynamic losses in partial admission turbines,* International Journal of Mechanical Sciences **11**, 417 (1969).

[30] J. Fridh, B. Bunkute, R. Fakhrai, and T. Fransson, *An experimental study on partial admission in a two-stage axial air test turbine with numerical comparisons,* Proceedings of ASME Turbo Expo Vienna **5**, 1285 (2004).

[31] D. Ainley, *Performance of axial-flow turbines,* Proceedings of the Institution of Mechanical Engineers **159**, 230 (1948).

[32] E. Knoernschild, *The radial turbine for low specific speeds and low velocity factors,* Journal of Engineering for Power **83**, 1 (1961).

[33] M. Pini, G. Persico, E. Casati, and V. Dossena, *Preliminary design of a centrifugal turbine for organic rankine cycle applications,* ASME Journal of Engineering for Gas Turbines and Power **135**, 042312 (2013).

[34] E. Lemmon, M. Huber, and M. McLinden, *NIST Standard Reference Database 23: Reference Fluid Thermodynamic and Transport Properties-REFPROP, Version 9.1, National Institute of Standards and Technology,* `https://www.nist.gov/srd/refprop` (2013).

[35] P. Colonna and T. van der Stelt, *Fluidprop: a program for the estimation of thermo physical properties of fluids,* `http://www.fluidprop.com` (2004).

[36] C. Soderberg, *Unpublished notes,* Gas Turbine Laboratory, Massachusetts Institute of Technology (1949).

[37] H. Craig and H. Cox, *Performance estimation of axial flow turbines,* Proceedings of the Institution of Mechanical Engineers **185**, 407 (1971).

[38] W. Traupel, *Thermische Turbomashinen* (Springer-Verlag Berlin Heidelberg, 1977).

[39] P. Meitner and A. Glassman, *Off-design performance loss model for radial turbine with pivoting, variable-area stators*, Tech. Rep. (NASA, 1980).

[40] M. Abidat, M. Hachemi, M. Hakidou, and N. Baines, *Prediction of the steady and non-steady flow performance of a highly loaded mixed flow turbine,* Proceedings of the Institution of Mechanical Engineers **212**, 173 (1998).

[41] I. Jahn, *Radial inflow turbine meshing revision 2*, Tech. Rep. (The University of Queensland, 2016).

[42] N. Baines, *Flow development in radial turbine rotors,* in *International Gas Turbine and Aeroengine Congress and Exhibition, ASME Paper* (1996).

[43] M. Zangeneh-Kazemi, W. Dawes, and W. Hawthorne, *Three dimensional flow in radial-inflow turbines,* ASME paper , 1 (1988).

[44] G. Angelino, *Carbon dioxide condensation cycles for power production,* Journal of Engineering for Power **90**, 287 (1968).

[45] D. Fleming, T. Holschuh, T. Conboy, G. Rochau, and R. Fuller, *Scaling considerations for a multi-megawatt class supercritical co*$_2$ *brayton cycle and path forward for commercialization,* ASME Paper No. GT2012-68484 (2012).

[46] M. Kulhanek and V. Dostal, *Thermodynamic analysis and comparison of supercritical carbon dioxide cycles,* Supercriticial CO$_2$ Power Cycle Symposium Colorado (2011).

[47] R. Fuller, J. Preuss, and J. Noall, *Turbomachinery for supercritical co*$_2$ *power cycles,* in *ASME Turbo Expo 2012: Turbine Technical Conference and Exposition* (American Society of Mechanical Engineers, 2012) pp. 961–966.

[48] H. Müller-Steinhagen and F. Trieb, *Concentrating solar power,* A review of the technology. Ingenia Inform QR Acad Eng **18**, 43 (2004).

[49] K. Brun, *Fundamentals and Applications of Supercritical Carbon Dioxide (sCO*$_2$*) Based Power Cycles* (Kent: Elsevier Science, 2017).

[50] Y. Ahn, S. Bae, M. Kim, S. Cho, S. Baik, J. Lee, and J. Cha, *Review of supercritical co*$_2$ *power cycle technology and current status of research and development,* Nuclear Engineering and Technology **47**, 647 (2015).

[51] R. Bidkar, A. Mann, R. Singh, E. Sevincer, S. Cich, M. Day, C. Kulhanek, A. Thatte, A. Peter, D. Hofer, and J. Moore, *Conceptual designs of 50 mw and 450 mw supercritical co*$_2$ *turbomachinery trains for power generation from coal. part 1: cycle and turbine,* The 5th International Symposium - Supercritical CO$_2$ Power Cycles San Antonio (2016).

[52] Y. Gong, N. Carstens, M. Driscoll, and I. Matthews, *Analysis of radial compressor options for supercritical co*$_2$ *power conversion cycles,* Massachusetts, USA: Center for Advanced Nuclear Energy Systems, MIT Department of Nuclear Science and Engineering (2006).

[53] J. Cha, T. Lee, J. Eoh, S. Seong, S. Kim, D. Kim, M. Kim, T. Kim, and K. Suh, *Development of a supercritical co*$_2$ *brayton energy conversion system coupled with a sodium cooled fast reactor,* Nuclear Engineering and Technology **41**, 1025 (2009).

[54] S. Wright, T. Conboy, and G. Rochau, *Break-even Power Transients for two Simple Recuperated sCO*$_2$ *Brayton Cycle Test Configurations.*, Tech. Rep. (Sandia National Laboratories (SNL-NM), Albuquerque, NM (United States), 2011).

[55] M. Persichilli, T. Held, S. Hostler, E. Zdankiewicz, and D. Klapp, *Transforming waste heat to power through development of a co*$_2$*-based-power cycle,* Electric Power Expo , 10 (2011).

[56] R. Vilim, *Development and validation of a radial inflow turbine model for simulation of the SNL sCO*$_2$ *split-flow loop.*, Tech. Rep. (Argonne National Laboratory (ANL), 2012).

[57] K. Kimball and E. Clementoni, *Supercritical carbon dioxide brayton power cycle development overview,* ASME Paper No. GT2012-68204 (2012).

[58] M. Utamura, H. Hasuike, K. Ogawa, T. Yamamoto, T. Fukushima, T. Watanabe, and T. Himeno, *Demonstration of supercritical co$_2$ closed regenerative brayton cycle in a bench scale experiment,* in *ASME Turbo Expo* (2012) pp. 155–164.

[59] J. Pasch, T. Conboy, D. Fleming, and G. Rochau, *Supercritical CO$_2$ recompression Brayton cycle: completed assembly description.*, Tech. Rep. (Sandia National Laboratories, 2012).

[60] T. Conboy, S. Wright, J. Pasch, D. Fleming, G. Rochau, and R. Fuller, *Performance characteristics of an operating supercritical co$_2$ brayton cycle,* Journal of Engineering for Gas Turbines and Power **134**, 111703 (2012).

[61] J. Sienicki, L. Krajtl, and A. Moisseytsev, *Utilization of the supercritical co$_2$ brayton cycle with sodium-cooled fast reactors,* (2014).

[62] T. Held, *Initial test results of a megawatt-class supercritical co$_2$ heat engine,* in *4th International Symposium on Supercritical CO$_2$ Power Cycles, Pittsburgh, PA, Sept* (2014) pp. 9–10.

[63] H. Zhang, H. Zhao, Q. Deng, and Z. Feng, *Aerothermodynamic design an numerical investigation of supercritical carbon dioxide turbine,* Turbine Technical Conference and Exposition Montréal (2015).

[64] E. Clementoni, T. Cox, and M. King, *Off-nominal component performance in a supercritical carbon dioxide brayton cycle,* Journal of Engineering for Gas Turbines and Power **138**, 011703 (2016).

[65] J. Cho, H. Shin, H. Ra, G. Lee, C. Roh, B. Lee, and Y. Baik, *Development of the supercritical carbon dioxide power cycle experimental loop in kier,* in *ASME Turbo Expo 2016: Turbomachinery Technical Conference and Exposition* (American Society of Mechanical Engineers, 2016) pp. V009T36A013–V009T36A013.

[66] J. Zhang, P. Gomes, M. Zangeneh, and B. Choo, *Design of a centrifugal compressor stage and a radial-inflow turbine stage for a supercritical co$_2$ recompression brayton cycle by using 3d inverse design method,* in *ASME Turbo Expo 2017: Turbomachinery Technical Conference and Exposition* (American Society of Mechanical Engineers, 2017) pp. V009T38A023–V009T38A023.

[67] R. Dambach, H. P. Hodson, and I. Huntsman, *An experimental study of tip clearance flow in a radial inflow turbine,* ASME 1998 International Gas Turbine and Aeroengine Congress and Exhibition **1** (1998).

[68] S. Wright, R. Radel, M. Vernon, G. Rochau, and P. Pickard, *Operation and analysis of a supercritical co$_2$ brayton cycle,* Sandia Report, No. SAND2010-0171 (2010).

[69] L. Meijboom, *Turbine design user manual*, Tech. Rep. (The University of Queensland, 2017).

[70] F. Palacios, T. Economon, A. Aranake, S. Copeland, A. Lonkar, T. Lukaczyk, D. Manosalvas, K. Naik, A. Padrón, B. Tracey, A. Variyar, and J. Alonso, *Stanford university unstructured (su2): Open-source analysis and design technology for turbulent flows,* AIAA paper **243**, 13 (2014).

[71] P. Jacobs, R. Gollan, A. Denman, B. O'Flaherty, D. Potter, P. Petrie-Repar, and I. Johnston, *Eilmer's theory book: basic models for gas dynamics and thermochemistry*, Tech. Rep. (The University of Queensland, 2012).

[72] S. Dixon and C. Hall, *Fluid mechanics and thermodynamics of turbomachinery* (Elsevier Butterworth-Heinemann, 2010).

[73] D. Japikse and N. Baines, *Introduction to turbomachinery* (Inc. and Oxford University Press, 1994).

[74] S. Vitale, M. Pini, A. Ghidoni, and P. Colonna, *Fluid dynamic design and analysis of a highly loaded centrifugal rotor for mini orc power systems,* 3rd International Seminar on ORC Power Systems Brussels (2015).

[75] M. Neale, *The tribology handbook* (Butterworth-Heinemann, 1995).

[76] K. Hirsch and R. Moghadam, *Validation of one-dimensional loss models for axial gas turbines*, Tech. Rep. (Lund Institute of Technology and Lund University, 2016).

[77] E. Casati, S. Vitale, M. Pini, G. Persico, and P. Colonna, *Centrifugal turbines for mini-organic rankine cycle power systems,* ASME Journal of Engineering for Gas Turbines and Power **136**, 122607 (2014).

[78] S. Dixon, *Fluid mechanics and thermodynamics of turbomachinery* (Elsevier Butterworth-Heinemann, 2005).

[79] D. Wilcox, *Turbulence modeling for cfd,* DCW Industries Inc (1994).

[80] R. Gollan, *Onedval: a tool to extract one-dimensionalised properties from CFD data,* Tech. Rep. (The University of Queensland, 2013).

[81] A. Yamamoto, *Production and development of secondary flows and losses in two types of straight turbine cascades: part 1 - a stator case,* Journal of Turbomachinery **109**, 186 (1987).

[82] M. Zangeneh, M. Schleer, F. Pløger, S. Hong, C. Roduner, B. Ribi, and R. Abhari, *Investigation of an inversely designed centrifugal compressor stage—part i: design and numerical verification,* Journal of Turbomachinery **126**, 73 (2004).

[83] G. Persico, *Evolutionary optimization of centrifugal nozzles for organic vapours,* Journal of Physics: Conference Series **821** (2017).

[84] A. Binder and R. Romey, *Secondary flow effects and mixing of the wake behind a turbine stator,* ASME 1982 International Gas Turbine Conference and Exhibit **1**, 1 (1982).

[85] A. Reichert and H. Simon, *Design and flow field calculation for transonic and supersonic radial inflow turbine guide vanes,* ASME 1995 International Gas Turbine and Aeroengine Congress and Exposition. American Society of Mechanical Engineers , V001T01A022 (1995).

[86] R. Span and W. Wagner, *A new equation of state for carbon dioxide covering the fluid region from the triple-point temperature to 1100 k at pressures up to 800 mpa,* Journal of physical and chemical reference data **25**, 1509 (1996).

[87] J. Sengers, R. Kayser, C. Peters, and H. White, *Equations of state for fluids and fluid mixtures*, Vol. 5 (Amsterdam: Elsevier, 2000).

[88] J. Qi, Private communication.

[89] J. Burgess, *Adaptive look-up table*, Tech. Rep. (The University of Queensland, 2016).

[90] G. Ding, Z. Wu, J. Liu, T. Inagaki, K. Wang, and M. Fukaya, *An implicit curve-fitting method for fast calculation of thermal properties of pure and mixed refrigerants,* International Journal of Refrigeration **28**, 921–932 (2005).

[91] H. Moustapha, M. Zelesky, N. Baines, and D. Japikse, *Axial and radial turbines*, Vol. 2 (Concepts NREC Wilder, 2003).

[92] W. Chain, P. Jacobs, J. Nap, D. Mee, R. Kirchhartz, and S. Stennett, *The* $k-\omega$ *turbulence model in Eilmer3: User guide and test cases*, Tech. Rep. (The University of Queensland, 2014).

[93] S. Futral and D. Holeski, *Experimental results of varying the blade-shroud clearance in a 6.02-inch radial-inflow turbine,* (1970).

[94] D. Musgrave, *The prediction of design and off-design efficiency for centrifugal compressor impellers,* in *Performance Prediction of Centrifugal Pumps and Compressors* (1979) pp. 185–189.

[95] C. Rodgers, *Mainline performance prediction for radial inflow turbine in small high pressure ratio turbine*, Tech. Rep. (Tech. rep., Von Karman Institute Lecture Series, 1987).

[96] G. Korth, *Effects of various parameters on the fatigue life of alloy 718*, Tech. Rep. (EG and G Idaho, Inc., Idaho Falls, ID (USA), 1991).

[97] K. McLallin and J. Haas, *Experimental performance and analysis of 15.04-centimeter-tip-diameter, radial-inflow turbine with work factor of 1.126 and thick blading.*, Tech. Rep. (NASA Cleveland Ohi Lewis Research Center, 1980).